Novel Low Loss Microwave & Millimeter-Wave Planar Transmission Lines

Yuyuan Lu

A Thesis
Submitted to the Faculty of Graduate Studies
in Partial Fulfillment of the Requirements
for the Degree of

Master of Science

Department of Electrical and Computer Engineering
University of Manitoba
Winnipeg, Manitoba, Canada

May 1999

0-612-41739-5

THE UNIVERSITY OF MANITOBA

FACULTY OF GRADUATE STUDIES

*****

COPYRIGHT PERMISSION PAGE

NOVEL LOW LOSS MICROWAVE & MILLIMETER-WAVE PLANAR TRANSMISSION LINES

BY

YUYUAN LU

A Thesis/Practicum submitted to the Faculty of Graduate Studies of The University of Manitoba in partial fulfillment of the requirements of the degree

of

MASTER OF SCIENCE

Abstract

This thesis focuses on the investigation of novel low loss microwave & millimeter-wave planar transmission lines using Finite-Difference Time-Domain (FDTD) method. The advantages of these planar transmission lines are their low resistive loss at microwave & millimeter-wave frequency bands and easy integration with microwave and millimeter-wave circuits and components.

The FDTD method solves Maxwell's time-dependent curl equations directly in the time domain by converting them into finite-difference equations. These are then solved in a time matching sequence by alternately calculating the electric and magnetic fields in an interlaced spatial grid. The advantage of this approach is the ability to investigate any arbitrary and inhomogeneous structure as well as obtains results efficiently.

Initially, a conventional substrate microstrip patch antenna fed by microstrip transmission line is studied using the FDTD. Discrete Fourier Transform (DFT) is used to transform voltage value from the time domain to frequency domain. The reflection coefficient S_{11} versus frequencies is obtained. The distribution spatial field components, at different time steps are computed and plotted out. The results agree well with the measured and published results. This demonstrates that the FDTD algorithm works correctly and well.

Next, the FDTD is extended to analyse micromachined microstrip transmission lines. Micromachined microstrip transmission lines with thick and thin upper substrates, as well as with the inverted micromachined microstrip transmission lines are studied.

Numerical results for the effective relative permittivity, the dielectric loss, the conductor loss and the characteristics impedance are presented with different groove sizes. It shows that the dielectric loss of a micromachined microstrip transmission line decreases greatly compared with that of its conventional counterpart. The spatial electric and magnetic field distributions in spectral domain are provided through the Discrete Fourier Transform (DFT).

Finally, for the first time trenched and micromachined coplanar waveguide transmission lines with and without ground planes are investigated using the FDTD. The grooves and trenches with different geometrical parameters at different positions inside the substrate are analysed. Numerical results for their effective relative permittivity, dielectric loss, conductor loss and characteristic impedance are provided. It is found that grooves below both the central transmission line and the gaps between the conductors can reduce the dielectric loss significantly, although the conductor loss changes little. In addition, for the first time, the spatial electric and magnetic field component distributions in the frequency domain are given. They show the mechanism of field propagation within these novel coplanar waveguide transmission lines.

Acknowledgements

I would like to express my greatest appreciation and the most sincere gratitude to my advisor, Professor L. Shafai for giving me a chance to work with him. His invaluable advice, helpful discussions and financial support were essential for the successful completion of this study and writing my thesis. Moreover, his profound knowledge and experience guided me constantly throughout the course of my studies and will impress me in all my life.

Special thanks to Dr. C. Shafai for his helpful discussion, Professor G. O. Martens for his suggestion about DFT & FFT, Dr. W. A. Charmma at DREO (Defence Research Establishment Ottawa) for his advice, and other colleagues in the Electromagnetic group at University of Manitoba for their friendly help and discussion.

I am also grateful to the Department of Electrical & Computer Engineering and Faculty of Graduate Studies at the University of Manitoba for providing the facility and making this research available.

Finally, I dedicated this thesis to my parents and grandmother to acknowledge their continuous understanding, long-term encouragement, great love and steadfast support. I also owe my older sister and younger brother who took over the most of my duties in the family across the Pacific Ocean.

Table of Contents

Abstract i

Acknowledgement iii

Table of Contents iv

List of Figures vi

Chapter 1. Introduction 1

1.1 Literature Survey 2

1.2 Purpose of This Thesis 13

Chapter 2. FDTD Theory 15

2.1 Maxwell's Equations 16

2.2 FDTD Theory and Formulas 17

2.3 Numerical Stability 23

2.4 Numerical Dispersion 24

2.5 Interface Between Media 24

2.6 Absorbing Boundary Conditions 26

2.7 Choice of Excitation 33

Chapter 3. Analysis of Conventional and Micromachined Microstrip Circuits . . 37

3.1 Analysis of Conventional Substrate Microstrip Patch Antenna 37

3.2 Analysis of Micromachined Planar Microstrip Transmission Lines 45

3.3 Inverted Micromachined Planar Microstrip Transmission Lines 61

Chapter 4. Analysis of Low Loss Coplanar Waveguide Transmission Lines 66

4.1 Analysis of Trenched Coplanar Waveguide Transmission Lines 66

4.1.1 Trenched Coplanar Waveguide Transmission Lines without Bottom Ground Planes 67

4.1.2 Trenched Coplanar Waveguide Transmission Lines with Bottom Ground Planes 73

4.2 Analysis of Micromachined Coplanar Waveguide Transmission Lines . . . 80

4.2.1 Micromachined Coplanar Waveguide Transmission Lines without Bottom Ground Planes 80

4.2.2 Micromachined Coplanar Waveguide Transmission Lines with Bottom Ground Planes. 88

Chapter 5. Conclusions and Future Work 95

Appendix A 99

Appendix B 102

Appendix C 108

Appendix D 109

References 111

List of Figures

Fig. 1.1.1 The Geometry of Microshield Line 4

Fig. 2.1.1 Relative Spatial Positions of Field Components at a "Yee" Unit Cell 18

Fig. 2.1.2 The "Leapfrog" Scheme to Calculate Electromagnetic Fields 22

Fig. 2.1.3 Boundary Points at x = 0 Used in the Mur ABC Difference Scheme 33

Fig. 3.1.1 Conventional Substrate Microstrip Line-fed Rectangular Patch Antenna . . 38

Fig. 3.1.2 Time Domain Gaussian Pulse Waveform used for Excitation of FDTD for Fig. 3.1.1 41

Fig. 3.1.3 Transient E_z Distribution just beneath the Microstrip Line at the Reference Plane 41

Fig. 3.1.4 Return Loss $|S_{11}|$ for the Microstrip Rectangular Patch Antenna 42

Fig. 3.1.5 The Time Domain Spatial Distribution of E_z beneath the Microstrip Line at the Reference Plane at Time Steps 200, 400 43

Fig. 3.1.6 The Time Domain Spatial Distribution of E_z beneath the Microstrip Line at the Reference Plane at Time Steps 600, 800 44

Fig. 3.2.1 Geometry Structure of Micromachined Microstrip Transmission Line 49

Fig. 3.2.2 Effective Relative Permittivity for Fig. 3.2.1 between Y = 130 dy & 150 dy 50

Fig. 3.2.3 Dielectric Loss for Fig. 3.2.1 between Y =130 dy & 150 dy 50

Fig. 3.2.4 Conductor Loss for Fig. 3.2.1 between Y =130 dy & 150 dy 51

Fig. 3.2.5 Characteristic Impedance for Fig. 3.2.1 at Y = 30 dy 51

Fig. 3.2.6 Characteristic Impedance for Fig. 3.2.1 Y = 50 dy 52

Fig. 3.2.7 Characteristic Impedance for Fig. 3.2.1 Y = 150 dy 52

Fig. 3.2.8 Electric & Magnetic Fields Distribution at 15 GHz at Y= 150 dy in X-Z Plane for Fig. 3.2.1 with $W_1 = 0$ 53

Fig. 3.2.9 Electric & Magnetic Fields Distribution at 30 GHz at Y= 150 dy in X-Z Plane for Fig. 3.2.1 with $W_1 = 0$ 54

Fig. 3.2.10 Electric & Magnetic Fields Distribution at 30 GHz at Y= 150 dy in X-Z Plane for Fig. 3.2.1 with $W_1 = 3\ W_2$ 55

Fig. 3.2.11 Effective Relative Permittivity for Fig. 3.2.1 between Y =130 dy & 150 dy with $h_1 = 0$ 58

Fig. 3.2.12 Dielectric Loss for Fig. 3.2.1 between Y =130 dy & 150 dy with $h_1 = 0$ . . . 58

Fig. 3.2.13 Conductor Loss for Fig. 3.2.1 between Y =130 dy & 150 dy with $h_1 = 0$ . . 59

Fig. 3.2.14 Characteristic Impedance for Fig. 3.2.1 with $h_1 = 0$ at Y = 30 dy 59

Fig. 3.2.15 Characteristic Impedance for Fig. 3.2.1 with $h_1 = 0$ at Y = 50 dy 60

Fig. 3.2.16 Characteristic Impedance for Fig. 3.2.1 with $h_1 = 0$ at Y = 150 dy 60

Fig. 3.3.1 Cross Section of Inverted Micromachined Microstrip Transmission Lines 62

Fig. 3.3.2 Effective Relative Permittivity for Fig. 3.3.1 between Y = 130dy & 150dy 63

Fig. 3.3.3 Dielectric Loss for Fig. 3.3.1 between Y =130 dy & 150 dy 63

Fig. 3.3.4 Conductor Loss for Fig. 3.3.1 between Y =130 dy & 150 dy 64

Fig. 3.3.5 Characteristic Impedance for Fig. 3.3.1 at Y = 30 dy 64

Fig. 3.3.6 Characteristic Impedance for Fig. 3.3.1 at Y = 50 dy 65

Fig. 3.3.7 Characteristic Impedance for Fig. 3.3.1 at Y = 150 dy 65

Fig. 4.1.1 Geometry Structure of Trenched Coplanar Waveguide Transmission Lines without a Bottom Ground Plane 68

Fig. 4.1.2 Effective Relative Permittivity for Fig. 4.1.1 between Y = 130dy & 150dy 69

Fig. 4.1.3 Dielectric Loss for Fig. 4.1.1 between Y = 130dy & 150dy 69

Fig. 4.1.4 Conductor Loss for Fig. 4.1.1 between Y = 130 dy & 150 dy 70

Fig. 4.1.5 Characteristic Impedance for Fig. 4.1.1 at Y = 150 dy 70

Fig. 4.1.6 Electric & Magnetic Fields Distributions at 15 GHz at Y=150 dy in X-Z Plane for Fig. 4.1.1 with h = 0 cm 71

Fig. 4.1.7 Electric & Magnetic Fields Distributions at 15 GHz at Y=150 dy in X-Z Plane for Fig. 4.1.1 with h = 0.016932 cm 72

Fig. 4.1.8 Geometry Structure of Trenched Coplanar Waveguide Transmission Line with a Bottom Ground Plane 75

Fig. 4.1.9 Effective Relative Permittivity for Fig. 4.1.8 between Y = 130dy & 150dy 76

Fig. 4.1.10 Dielectric Loss for Fig. 4.1.8 between Y = 130 dy & 150 dy 76

Fig. 4.1.11 Conductor Loss for Fig. 4.1.8 between Y = 130 dy & 150 dy 77

Fig. 4.1.12 Characteristic Impedance for Fig. 4.1.8 at Y = 150 dy 77

Fig. 4.1.13 Electric & Magnetic Fields Distributions at 15 GHz at Y=150 dy in X-Z Plane for Fig. 4.1.8 with h = 0 cm 78

Fig. 4.1.14 Electric & Magnetic Fields Distributions at 15 GHz at Y=150 dy in X-Z

Plane for Fig. 4.1.8 with h = 0.016932 cm 79

Fig. 4.2.1 Geometry Structure of Micromachined Coplanar Waveguide Transmission Line with a Bottom Ground Plane 82

Fig. 4.2.2 Cross Sections for Fig. 4.2.1 for Calculations 83

Fig. 4.2.3 Effective Relative Permittivity for Fig. 4.2.1 between Y = 130dy & 150dy 84

Fig. 4.2.4 Dielectric Loss for Fig. 4.2.1 between Y = 130 dy & 150 dy 84

Fig. 4.2.5 Conductor Loss for Fig. 4.2.1 between Y = 130 dy & 150 dy 85

Fig. 4.2.6 Characteristic Impedance for Fig. 4.2.1 at Y = 150 dy 85

Fig. 4.2.7 Electric & Magnetic Fields Distributions at 15 GHz at Y=150 dy in X-Z Plane for Case 2 in Fig. 4.2.2 86

Fig. 4.2.8 Electric & Magnetic Fields Distributions at 15 GHz at Y=150 dy in X-Z Plane for Case 4 in Fig. 4.2.2 87

Fig. 4.2.9 Geometry Structure of Micromachined Coplanar Waveguide Transmission Line without a Bottom Ground Plane 90

Fig. 4.2.10 Effective Relative Permittivity for Fig. 4.2.9 between Y = 130 dy & 150 dy 91

Fig. 4.2.11 Dielectric Loss for Fig. 4.2.9 between Y = 130 dy & 150 dy 91

Fig. 4.2.12 Conductor Loss for Fig. 4.2.9 between Y = 130 dy & 150 dy 92

Fig. 4.2.13 Electric & Magnetic Fields Distributions at 15 GHz at Y=150 dy in X-Z Plane in Fig. 4.2.9 with W_1 = 0.021165 cm 93

Fig. 4.2.14 Electric & Magnetic Fields Distributions at 15 GHz at Y=150 dy in X-Z Plane in Fig. 4.2.9 with W_1 = 0.033864 cm 94

Fig. B.1 Effective Relative Permittivity for Fig. 3.2.1 between Y = 130 & 150 dy with grids 160 dx * 300 dy * 80 dz 104

Fig. B.2 Dielectric Loss for Fig. 3.2.1 between Y =130 & 150 dy with grids 160 dx * 300 dy * 80 dz 104

Fig. B.3 Conductor Loss for Fig. 3.2.1 between Y =130 & 150 dy with grids 160 dx * 300 dy * 80 dz 105

Fig. B.4 Characteristic Impedance for Fig. 3.2.1 at Y = 30 dy with grids 160 dx * 300 dy * 80 dz 105

Fig. B.5 Characteristic Impedance for Fig. 3.2.1 Y = 50 dy with grids 160 dx * 300 dy * 80 dz. 106

Fig. B.6 Characteristic Impedance for Fig. 3.2.1 Y = 150 dy with grids 160 dx * 300 dy * 80 dz. 106

Fig. B.7 Effective Relative Permittivity for Fig. 3.2.1 for L = 10 dy. 107

Fig. B.8 Effective Relative Permittivity for Fig. 3.2.1 for L = 40 dy. 107

Fig. C.1 Effective Relative Permittivity for Fig. 3.2.1 between Y = 130 dy & 150 dy with Time Steps 8000. 108

Fig. C.2 Effective Relative Permittivity for Fig. 3.2.1 between Y = 130 dy & 150 dy with Time Steps 20000. 109

CHAPTER 1

Introduction

Planar transmission lines are of prime importance for a variety of applications, notably those concerning monolithic microwave or millimeter-wave integrated circuits (MMIC), millimeter-wave components and wireless communication system. The planarization of transmission lines to microstrip, stripline or coplanar-waveguide form provides great flexibility in design, reduced weight and volume, and compatibility with active devices and radiating elements. Furthermore, modern wireless communication systems are moving steadily to higher frequencies at millimeter-wave frequency band in order to obtain a wide bandwidth. An important wireless communication system is the Local Multipoint Distribution Systems (LMDS) that operates around 28 GHz. EHF satellites use 20-30 GHz. Other systems, such as point-to-point communications and collision avoidance radar use frequencies from 40 GHz to 70 GHz or even higher.

However, ohmic loss, dielectric loss and dispersion in transmission systems and active circuitry increases drastically with the increase of frequency especially at millimeter-wave frequencies. In addition, despite the success achieved in most MMIC, high power has remained a challenge. The low output power of solid-state source, along with their low impedance, is further hindered by conventional transmission line characteristics, resulting in very low efficiency. Besides, the transitions in MMIC have loss and connections such as bondwires in chips become too inductive. Thus, looking for new transmission system configurations and chip packages become necessary.

Recently, several novel planar transmission lines including the microstrip and coplanar waveguide were proposed and have attracted much attention due to their excellent performance over the conventional counterparts at microwave and millimeter-wave frequency bands. In this thesis, several types of low loss planar transmission lines, such as micromachined, inverted micromachined and trenched ones and their various characteristics parameters are studied extensively.

1.1 Literature Survey

The first planar transmission line, the stripline, was introduced almost fifty years ago and created the basis of a new and revolutionary hybrid technology which has evolved to the monolithic one, drastically increasing operating frequencies and consequently reducing weight and volume. In a conventional transmission line, the power is propagated by creating an RF voltage difference between two planar conductors printed on the same (coplanar waveguides, coplanar strip lines) or opposite surface (stripline, microstrip line, coupled strip lines) of a dielectric slab structure. In most cases, the geometry of the conventional lines permits great design flexibility, tremendous reduction of the space occupied by the circuit, and realization of very large scale, very high frequency applications.

The planarization of the conductors in the above transmission lines provides the capability of integration but also generates fringing in the electromagnetic fields, leading to unwanted radiation and dispersion, and enhanced ohmic loss and electromagnetic coupling. These phenomena are frequency dependent and impose serious limitations at millimeter-wave frequency range. The ability to find new geometries which reduce or eliminate the above loss or coupling mechanism but do not affect the monolithic characteristics of the line will extend the operating frequencies high into the millimeter-wave band region and will improve circuit performance in existing applications.

A new type of monolithic planar transmission line, a microshield line appropriate for circuit or array applications, was proposed by N. I. Dib et al. [1] in 1991. Its geometry is shown in Fig. 1.1.1. It may be considered as the evolution of the conventional microstrip or coplanar structures and are characterized by reducing radiation loss and electromagnetic interference. By using membrane technology, it eliminates dielectric loss which could be high at millimeter-wave frequencies. One of the advantages of the microshield lines, compared with the other conventional ones such as microstrip lines or coplanar waveguide, is the ability to operate without the need for via-holes or the use of air-bridges for ground equalization. Specifically, by varying the size of the shielded waveguide, the per unit length capacitance of the line can increase or decrease from the value of the corresponding microstrip lines or coplanar waveguide resulting in the lower or higher values of the characteristic impedance. The wavelength of the propagating wave in the structure is closer to the free space wavelength or equal to it due to the membrane. Furthermore, it radiates less than the conventional microstrip line or coplanar waveguide (CPW) and can provide a wide range of characteristic impedances due to the many parameters for design. The analysis method they used is the space domain integral equation method. In 1992, N. Dib et al. [27] calculated the characteristic impedance of microshield lines using both computational intensive point matching method (PMM) and analytical conformal mapping method (CMM). Their features with respect to other conventional planar transmission lines are highlighted. The effect of finite extent ground planes on the characteristics impedance was demonstrated. It was found that small ground planes suffice to insure negligible effect on the line characteristics.

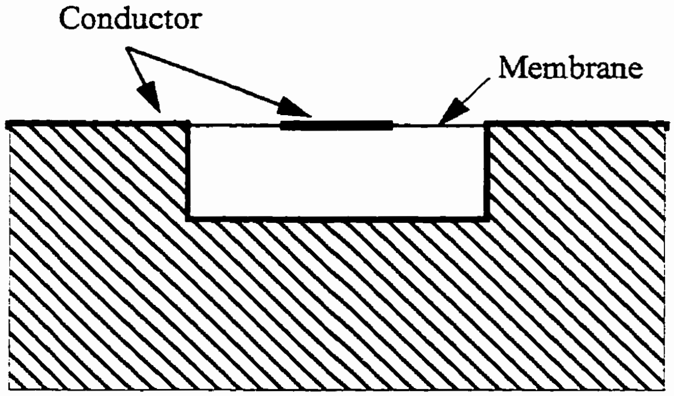

Fig. 1.1.1 The Geometry of Microshield Line

In 1993, T. M. Weller et al. [2] provided the first experiment data on microshield transmission line circuits using the membrane technology. Several types of microshield circuits were fabricated and measured, including stepped-impedance filters, stubs and transitions from grounded coplanar waveguide (GCPW) to microshield. The results showed that the microshield structures are able to improve the performance relative to conventional planar transmission line structures. The desirable waveguide properties were also exhibited, including pure TEM propagation and zero dispersion in a wide single mode frequency band, low radiation loss, zero dielectric loss and a broad range of possible line impedance.

Linda P. Katehi et al. summarized their experimental work about the micromachined circuits for millimeter and sub-millimeter-wave application done at the University of Michigan in 1993 [3]. Two techniques had shown promise and had extensively used micromachining to realize novel circuits. The first utilized a membrane-supported transmission-line configuration, namely microshield line, and has the most superior performance. It is characterized by zero dielectric loss, very low radiation loss, reduced electromagnetic interference and compatibility with conventional microstrip or coplanar waveguide. Membrane supported transmission lines are quasi-planar configurations, in which a pure, non-dispersive TEM wave is propagated through a two-conductor system, embedded in a homogeneous environment. The experiment results demonstrated extremely low propagation loss and faster wave velocities of micromachined transmission lines than those of the conventional monolithic transmission lines up to 500 GHz. The second technique introduced new concepts in packaging for miniaturized circuits, using integrated-shielding cavities and emphasized size/volume/cost reduction. The measured data showed that the total loss is 3 dB lower for the micromachined circuits from 10 GHz to 40 GHz due to lower parasitic radiation. Both methods can reduce ohmic loss and eliminated electromagnetic-parasitic effects without affecting the monolithic characteristics. Operating frequencies can be thereby extended.

T. M. Weller et al. [4] examined the conductor loss and effective dielectric constant of microshield lines and presented results on transitions to conventional coplanar waveguide, right-angle bends, different stub configurations, lowpass and bandpass filters. Experimental data as well as numerical results derived from an integral equation method had demonstrated the performance superior to the conventional coplanar waveguide circuits as high as 40 GHz. There were clear performance difference between the microshield line and a substrate-supported line, including larger circuit dimensions due to the low dielectric constant and the use of thin dielectric membrane.

In 1996, S. Robertson et al. [5] studied two types of micromachined planar transmission lines at W-Band frequencies (75 - 110 GHz): microshield line and shielded membrane microstrip (SMM) line. In both of their structures, the conducting lines are suspended on thin dielectric membranes. The transmission lines are essentially 'floating' in the air, possess negligible levels of dielectric loss and do not suffer from the parasitic effects of radiation and dispersion. They tested a 90 GHz low pass filter and several 95 GHz band pass filters and obtained excellent performance which can not be achieved with traditional substrate supported circuits in CPW or microstrip configurations. In addition, finite-difference time-domain (FDTD) method was used to verify the measured performance of the W-Band circuits and compare the performance of membrane supported circuits and equivalent substrate supported circuits. It demonstrated the ability of micromachined transmission lines to provide very high performance planar circuits at millimeter-waveband. Consequently, it was concluded that micromachining and membrane technology are good options to effectively eliminate dispersion, radiation loss and dielectric loss on high performance millimeter-wave planar circuits.

Chen-Yu Chi et al. [29] fabricated planar microwave and millimeter-wave inductors and capacitors suspended on the membrane over high-resistivity silicon substrates using micromachining technologies to reduce the parasitic capacitance to ground. The resonant frequency of a 1.2 nH and a 1.7 nH inductors have been increased from 22 GHz and 17

GHz to around 70 GHz and 50 GHz respectively. It was found the membrane inductors and capacitor built using micromachining technologies showed much better performance than their Silicon/GaAs counterparts.

In 1994, M. Vaughan et al. [28] studied the micromachined microstrip patch antenna over high dielectric constant substrate, e. g. GaAs. It was reported that removing all of the substrate underneath the patch can effectively eliminate surface waves and increases the efficiency and directivity as well as removing the ripple in the radiation pattern. Thus, the micromachined technology improved the radiation patterns of microstrip patch antennas. In 1996, M. Stotz et al. [31] reported that planar aperture coupled millimeter-wave microstrip patch antennas on thin SiN_x membranes over GaAs substrate operating at 77GHz were fabricated and tested. Their triple patch antennas exhibited symmetrical radiation patterns with a 10 dB mainbeam width of 38°. The method of moments in spectral domain was used. Chen-Yu Chi et al. [32] reported stripline resonators on thin dielectric membranes that showed dispersion-free, conductor-loss limited performance at 13.5 GHz, 27.3 GHz and 39.6 GHz. The unloaded-Q of the resonators increases as $f^{1/2}$ with frequency and was measured to be 386 at 27 GHz. The micromachined filter made from the stripline resonator exhibited a passband return loss better than -15 dB and a conductor-loss limited 1.7 dB port-to-port insertion loss at 20.3 GHz.

Micromachining transmission lines were also used for self-packaged high frequency circuits [30]. In the work done by R. F. Drayton etc. [30], they developed miniaturized housing to shield individual passive components, active elements by employing silicon micromachining technology. Self-packaged configurations that are fabricated in this way can reduce the overall size and weight of a circuit and provide the isolation between neighbour circuits. Therefore, the resulting characteristics make these micropackaged components appropriate for high density, multilevel interconnect circuits. Delay lines, a short-end/open-end tuning stub and stepped impedance lowpass filters were developed. The measured data shows that the monolithic incorporation of a shielding cavity with the circuit can improve performance.

A wide-band self-packaged 20 dB directional coupler was designed and fabricated on a thin dielectric membrane using membrane-support transmission lines by S. Robertson et al. [8] in 1998. The fabrication process is compatible with monolithic microwave integrated circuit (MMIC) techniques and the coupler can be integrated into a planar-circuit layout. The use of membrane-support transmission lines resulted in less than 0.5 dB insertion loss in the coupler from 10 to 60 GHz. In addition, micropackaging techniques were used to create a shield circuit which is extremely compact and lightweight.

Micromachining microstrip transmission line technologies are applied excellently not only to the microwave and millimeter-wave components, but also to the design of low resistive loss microstrip antennas. G. P. Gauthier et al. [33] designed, fabricated and tested 77 GHz dual-polarized microstrip antennas suspended on the $SiO_2/Si_3N_4/SiO_2$ membrane over silicon wafer for automotive collision avoidance systems. The measurements indicated a 2 GHz bandwidth with a -18 dB isolation between the orthogonal ports. Almost at the same period, tapered slot antennas operating at 35 GHz were fabricated on thick (1.27 mm) low relative dielectric constant ($\varepsilon_r = 2.2$) substrate using micromachining technologies and were tested [34]. Several periodic hole structures were machined into the substrate and the resulting antenna pattern measurements were compared. The micromachining of the substrate improves the antenna patterns due to the reduction of the effective dielectric constant of the substrate.

G. P. Gauthier et al. [35] applied the closely paced holes underneath a microstrip antenna on a high relative dielectric constant substrate ($\varepsilon_r = 10.8$) to synthesize a localized low relative dielectric constant environment ($\varepsilon_r = 2.3$). The measured radiation efficiency of a microstrip antenna on a micromachined 635-μm thick $\varepsilon_r = 10.8$ Duroid 6010 substrate increased from 48% to 73% at 12.8 - 13.0 GHz.

I. Papapolymerou et al. [36] proposed the use of selective lateral etching based on micromachining techniques to enhance the performance of rectangular microstrip patch antennas printed on high-index wafers such as Silicon, GaAs, and InP. Micromachined patch antennas on Si substrates have shown superior performance over conventional designs where the bandwidth and the efficiency have increased by as much as 64% and 28% respectively. In their work, the silicon material was removed laterally underneath the patch antenna to produce a cavity which consists of a mixture of air and substrate with equal or unequal thicknesses. Characterization of the micromachined patch antenna showed the improvement of bandwidth, smoother E-plane radiation patterns, higher efficiency compared to the conventional patch designed on high-index materials. In addition, the overall dimensions of the radiating element are determined by the effective dielectric constant of the material and can range from its smallest size in a high-index material such as silicon ($\varepsilon_r = 11.7$) to its largest size in an air substrate ($\varepsilon_r = 1$) region.

V. M. Lubecke et al. applied micromachining technologies on terahertz applications [37]. Their work focused on the development of antennas and frontend components which can be integrated in large numbers for focal-plane arrays or low-cost terahertz systems. Waveguide antennas, transmission lines and mixer block assemblies were fabricated through various economical micromachining techniques, with performance comparable to that of costly conventionally produced components. Micromachining is shown to provide a low-cost alternative to expensive conventional machined-waveguide technology, resulting in antennas with excellent radiation patterns, low-loss tuner and three-dimensional micromachined structures suitable for terahertz application.

W. Chamma & L. Shafai et al. [24] studied the dispersion characteristics of suspended microstrip line on the segmented dielectric substrate where the dielectric permittivity of the lower substrate was changed along the transverse direction using FDTD and Method of Lines (MOL). Their results showed that propagation characteristics of this type of transmission lines vary widely with the change of the relative dielectric constant of the lower substrate. In 1998, N. Gupta & L. Shafai et al. [25] proposed a new inverted grooved microstrip line structure for low loss configuration. Some simulation and experimental work had been done to analyse the dispersion characteristics of this line in the frequency range of 1-16 GHz. The conductor and dielectric loss were calculated and compared with the experimental results.

Besides micromachining microstrip transmission lines, micromachined or trenched coplanar waveguide transmission lines are other types of low loss transmission lines which are important in wireless communication systems and MMIC. V. Milanovic et al. [6] designed, fabricated and measured a new kind of micromachining coplanar waveguide transmission lines for sensors and analog and digital integrated circuits. It was found the absence of the lossy silicon substrate after etching results in significantly improved insertion-loss characteristics, dispersion characteristics, and higher phase velocity. The measurements of the waveguides both before and after micromachining performed at frequencies from 1 to 40 GHz using a Vector Network Analyser, showed the improvement of the loss characteristics in orders of magnitude. For the entire range of frequencies 0~40 GHz for the 50Ω layout, the insertion loss does not exceed 4 dB/cm which are due to the small width and thickness of the metal strips. Before etching, insertion loss are as high as 38 dB/cm because of the currents in the underlying substrate. Phase velocity in the micromachined coplanar waveguide transmission lines is close to that in free space.

P. Salzenstein et al. [41] designed and fabricated coplanar waveguide transmission lines on Si_3N_4 and polyimide membranes deposited on GaAs substrates. Their on-wafer measurements of scattering parameters up to 75 GHz for several line configurations showed a constant phase velocity of $2.9*10^8$ m/s and a predominance of metallic loss with a square root frequency dependence. T. L. Willke et al. [39] introduced a new class of three-dimensional micromachined microwave and millimeter-wave planar transmission lines and filters using LIGA process. The LIGA process allows tall (10 μm to1 mm), high-aspect ratio metal structures to be very accurately patterned and is compatible with integrated circuit-fabrication processes. The tall metal transmission lines will enable the development of high-power monolithic circuits as well as couplers and filters that require very high coupling. Bandpass and low-pass filters fabricated using 200-μm-tall nickel microstrip lines are demonstrated at X-band.

In 1998, K. Herrick et al. [38] designed and built Si-micromachined lines and circuit components operated between 2-110 GHz and measured their characteristics. In these lines, which are a finite-ground coplanar (FGC) type, Si micromachining is used to remove the dielectric material from the aperture regions in order to reduce dispersion and minimize propagation loss. This new class of Si micromachined lines has demonstrated excellent performance, ease in design and fabrication and very low cost in development due to their ability to excite a TEM mode, operate free of parasitic parallel-plate modes and operate without vias. Micromachined FGC lines have been used to develop V- and W-band bandpass filters. The W-band micromachined FGC filter has shown a 0.8 dB improvement in insertion loss at 94 GHz over a conventional FGC line. This approach offers an excellent alternative to the membrane technology, exhibiting very low loss, no dispersion, and mode-free operation without using membranes to support the interconnect structure. The same group measured and evaluated state-of-the-art planar transmission lines and vertical interconnect for use in high-density unilateral circuits for silicon and SiGe-based monolithic high-frequency circuits [7]. Depending on the application, both micromachined microstrip and FGC waveguide were used in highly dense circuits areas. They had shown substantial loss reduction with minimal silicon removal in the aperture regions. All the vertical interconnects have been fabricated on high-resistivity Si and have demonstrated excellent performance at frequencies up to 110 GHz. In addition, the use of silicon had allowed for the development of a variety of micromachined shapes that may provide lower parasitic and better performance.

Low RF loss trenched coplanar waveguide (CPW) transmission line structures using evaporated aluminium tracks on a high-resistivity (10-k$\Omega \cdot$ cm) silicon (HRS) substrate were established experimentally and simulated using semiconductor device simulation package with the finite-element analysis by S. Yang et al. [40] in1998. By introducing a vertical trench in the gaps between signal transmission line and ground planes, and by DC biasing the CPW line, RF loss can be reduced. Their experimental results showed that the reduction of RF loss in comparison with conventional aluminium conductor CPW line structures may be as much as 0.5 dB /cm at 30 GHz and by proper positive DC biasing of a CPW line on a p-type HRS substrate a further reduction (0.2 dB/cm) in RF loss at 30 GHz will be achieved. The reason for the reduction of RF loss is primarily due to the smaller substrate leakage conduction current and to the reduction in conductor loss owing to the removal of field concentration from the vicinity of the conductor edges.

However, most of the previous work focused on experiment. Rigorous theoretical analyse is needed in order to design low loss microwave & millimeter-wave planar transmission lines, planar microwave & millimeter-wave circuits or components better and quicker.

1.2 Purpose of this Thesis

The purpose of this thesis is to analyse the low loss microwave and millimeter-wave planar transmission lines using the Finite-Difference Time-Domain (FDTD) method. Due to the geometrical and material generality of FDTD method, this research will give the following significant contributions to the area of the low loss microwave and millimeter-wave planar transmission lines:

1. It is the first time that some frequency-dependent parameters, such as effective relative permittivity, characteristic impedance, dielectric loss and conductor loss are offered systematically for various groove widths or trench depths of micromachined or trenched planar transmission lines so that wireless transmission system, antenna and MMIC designers can choose appropriate data for their experimental designs at millimeter-wave fre-

quency so that the design cycle can be reduced.

2. The electric and magnetic fields distributions of trenched and micromachined coplanar waveguide transmission lines are obtained for the first time and the mechanism for lower dielectric loss is analysed.

The organization of this thesis is: Chapter 2 deals with the FDTD theory. It presents some factors which might influence the FDTD algorithm, such as stability, dispersion, interface between media, absorbing boundary conditions and choice of excitation. A conventional microstrip patch antenna is analyzed in Chapter 3. Its reflection coefficient S_{11} and electric field distributions in different time steps are shown. In Chapter 3, micromachined planar microstrip transmission lines with different groove widths are also calculated. The effective relative permittivity, dielectric loss, conductor loss and characteristic impedance as well as electric and magnetic fields distributions in frequency domain are given. In Chapter 4, 4 new kinds of coplanar waveguide transmission lines are studied. They are trenched or micromachined coplanar waveguide transmission lines with or without a bottom ground plane. Their characteristics of attenuation, impedance, effective relative dielectric constant as well as electric and magnetic field distributions are plotted out. Chapter 5 is the conclusion and some suggestion for the future work.

CHAPTER 2

FDTD Theory

The Finite-Difference Time-Domain (FDTD) originally proposed by K. S. Yee in 1966 [9] has progressed very rapidly for solving electromagnetic problems in the past decade, due to the development of high speed and large memory computers. It is also used extensively for the analysis and design of microstrip structures at microwave and millimeter-wave frequencies. It offers several advantages over other methods. It can easily model inhomogeneous structures, characterizing microstrip geometries without complex mathematical formulations. As a full wave analysis method, FDTD's another advantage is its time-domain solution where using the time response of the problem calculated in a single running cycle, one can obtain the frequency response over a wide frequency range using Discrete Fourier Transformation. Also, FDTD provides an extensive volume of electric and magnetic field components history inside the computational domain comprising the modelled geometry.

Furthermore, using FDTD, Maxwell's equations are discretized into both time and spatial central finite difference equations. Knowing the initial, boundary and excitation conditions, the fields on the nodal points of the space-time mesh can be calculated in a leapfrog time marching manner. In 1988, X. Zhang and K. K. Mei et al. calculated the dispersive characteristics of microstrips and frequency-dependent characteristics of microstrip discontinuities using FDTD [10-11]. They compared their results with other published ones and verified that FDTD is a viable method for modelling microstrip components. In 1989 FDTD was first used to analyse microstrip patch antennas by A. Reineix et al. [12] and some frequency-dependent parameters were given using FFT. In 1990, D. M. Sheen et al. [13] presented FDTD results for various microstrip structures, including microstrip rectangular patch antenna, a low-pass filter and a branch-line coupler.

Due to the advantages of FDTD aforementioned, it was applied in this research to analyse novel low loss microwave and millimeter-wave planar transmission lines.

2.1 Maxwell's Equations

The propagation of electromagnetic waves can be represented with the time-domain Maxwell's curl equations. They are:

$$\nabla\times\boldsymbol{H} = \varepsilon\frac{\partial \boldsymbol{E}}{\partial t} + \sigma\boldsymbol{E} \tag{2.1}$$

$$\nabla\times\boldsymbol{E} = -\mu\frac{\partial H}{\partial t} \tag{2.2}$$

where **E** is the electric field in *volt/meter*; **H** is the magnetic field in *ampere/meter*; ε is the electric permittivity in *farad/meter*; μ is the magnetic permeability in *henry/meter*; σ is the conductivity in *mhos(siemens)/meter*. Assuming isotropic physical parameters, Maxwell's equations can be written in the rectangular coordinates as:

$$\mu\frac{\partial H_x}{\partial t} = \frac{\partial E_y}{\partial z} - \frac{\partial E_z}{\partial y} \tag{2.3}$$

$$\mu\frac{\partial H_y}{\partial t} = \frac{\partial E_z}{\partial x} - \frac{\partial E_x}{\partial z} \tag{2.4}$$

$$\mu\frac{\partial H_z}{\partial t} = \frac{\partial E_x}{\partial y} - \frac{\partial E_y}{\partial x} \tag{2.5}$$

$$\varepsilon\frac{\partial E_x}{\partial t} = \frac{\partial H_z}{\partial y} - \frac{\partial H_y}{\partial z} - \sigma E_x \tag{2.6}$$

$$\varepsilon\frac{\partial E_y}{\partial t} = \frac{\partial H_x}{\partial z} - \frac{\partial H_z}{\partial x} - \sigma E_y \tag{2.7}$$

$$\varepsilon\frac{\partial E_z}{\partial t} = \frac{\partial H_y}{\partial x} - \frac{\partial H_x}{\partial y} - \sigma E_z \tag{2.8}$$

2.2 FDTD Theory and Formulas

The Finite-Difference Time-Domain (FDTD) method was a direct solution of the time-dependent Maxwell's equations (2.1) and (2.2) in time-domain using finite-difference technique. As the first step, the space containing the structure of interests is divided into a number of small elements called "Yee Cells", shown in Fig. 2.1.1. The E and H fields in each "Yee Cell" are interleaved both in time and space. This permits the space and time derivatives in Maxwell's equation to be approximated by central difference operations with the second order accuracy. Six FDTD time-stepping expressions are thus derived from Maxwell's curl equations [9]. After applying an electromagnetic excitation and setting initial values for all of the field components, the fields are calculated iteratively using these finite equations as long as the response is of interest.

FDTD algorithm solves the partial differential equations (2.3) to (2.8) by first filling up the computation space with a number of "Yee" cells. One of them is shown in Fig. 2.1.1.

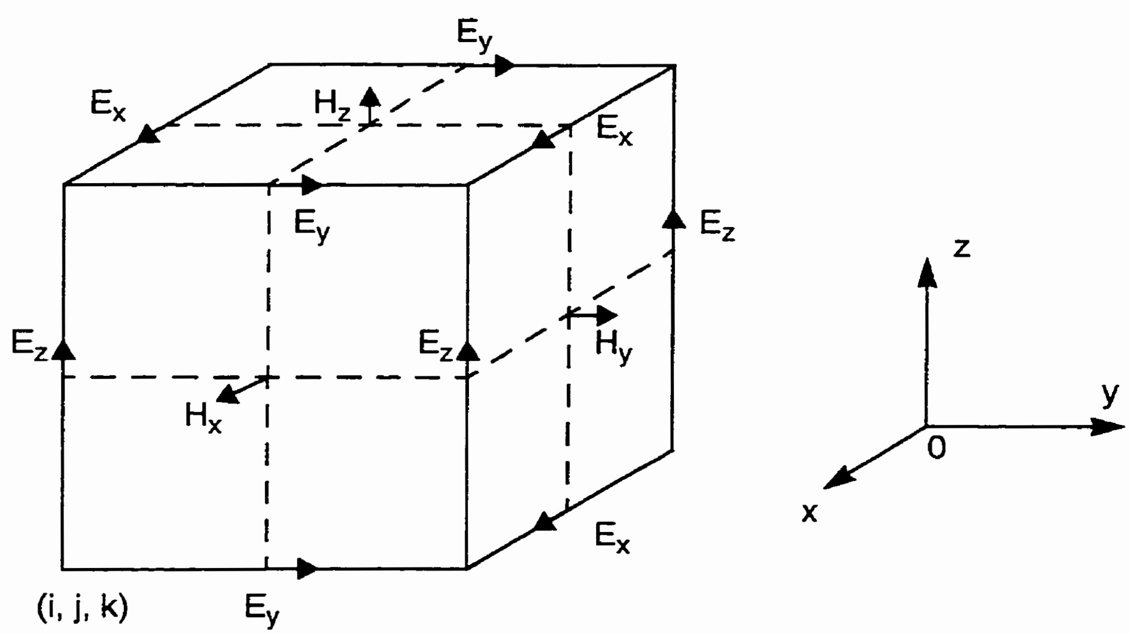

Fig. 2.1.1 Relative Spatial Positions of Field Components at a "Yee" Unit Cell

The relative spatial arrangement of the E fields and H fields on the "Yee" cell is the key of this algorithm, because it enables the space derivatives in equation (2.3) to (2.8) to be approximated by central difference operations with the second order accuracy shown from (2.9) to (2.11):

$$\frac{\partial \phi}{\partial x}(i\Delta x, j\Delta y, k\Delta z, n\Delta t) = \frac{\phi^n(i+0.5, j, k) - \phi^n(i-0.5, j, k)}{\Delta x} + O\left[(\Delta x)^2\right] \quad (2.9)$$

$$\frac{\partial \phi}{\partial y}(i\Delta x, j\Delta y, k\Delta z, n\Delta t) = \frac{\phi^n(i, j+0.5, k) - \phi^n(i, j-0.5, k)}{\Delta y} + O\left[(\Delta y)^2\right] \quad (2.10)$$

$$\frac{\partial \phi}{\partial z}(i\Delta x, j\Delta y, k\Delta z, n\Delta t) = \frac{\phi^n(i, j, k+0.5) - \phi^n(i, j, k-0.5)}{\Delta z} + O\left[(\Delta z)^2\right] \quad (2.11)$$

where $\phi^n(i, j, k) = \phi(i\Delta x, j\Delta y, k\Delta z, n\Delta t)$ is one of the six field components at the lattice point $(i, j, k) = (i\Delta x, j\Delta y, k\Delta z)$ at time step n, Δx, Δy and Δz are the space increments in the x, y and z direction respectively. Δt is the time increment.

A similar central difference scheme is also applied to the time derivatives:

$$\frac{\partial \phi}{\partial t}(i\Delta x, j\Delta y, k\Delta z, n\Delta t) = \frac{\phi^{n+0.5}(i, j, k) - \phi^{n-0.5}(i, j, k)}{\Delta t} + O\left[(\Delta t)^2\right] \quad (2.12)$$

By applying the above approximations in equations (2.3) to (2.8), the system of partial difference equations can be transformed to the following six FDTD time-stepping expressions:

$$H_x^{n+0.5}(i,j+0.5,k+0.5) = H_x^{n-0.5}(i,j+0.5,k+0.5) +$$
$$\frac{\Delta t}{\mu\Delta z}\left(E_y^n(i,j+0.5,k+1) - E_y^n(i,j+0.5,k) \right) -$$
$$\frac{\Delta t}{\mu\Delta y}\left(E_z^n(i,j+1,k+0.5) - E_z^n(i,j,k+0.5) \right) \tag{2.13}$$

$$H_y^{n+0.5}(i+0.5,j,k+0.5) = H_y^{n-0.5}(i+0.5,j,k+0.5) +$$
$$\frac{\Delta t}{\mu\Delta x}\left(E_z^n(i+1,j,k+0.5) - E_z^n(i,j,k+0.5) \right) -$$
$$\frac{\Delta t}{\mu\Delta z}\left(E_x^n(i+0.5,j,k+1) - E_x^n(i+0.5,j,k) \right) \tag{2.14}$$

$$H_z^{n+0.5}(i+0.5,j+0.5,k) = H_z^{n-0.5}(i+0.5,j+0.5,k) +$$
$$\frac{\Delta t}{\mu\Delta y}\left(E_x^n(i+0.5,j+1,k) - E_x^n(i+0.5,j,k) \right) -$$
$$\frac{\Delta t}{\mu\Delta x}\left(E_y^n(i+1,j+0.5,k) - E_y^n(i,j+0.5,k) \right) \tag{2.15}$$

$$E_x^{n+1}(i+0.5,j,k) = \frac{2\varepsilon - \sigma\Delta t}{2\varepsilon + \sigma\Delta t}\left(E_x^{n}(i+0.5,j,k) \right) +$$

$$\frac{\Delta t}{(2\varepsilon+\sigma\Delta t)\,\Delta y}\left(H_z^{n+0.5}(i+0.5,j+0.5,k)\;-H_z^{n+0.5}(i+0.5,j-0.5,k)\;\right)-$$

$$\frac{\Delta t}{(2\varepsilon+\sigma\Delta t)\,\Delta z}\left(H_y^{n+0.5}(i+0.5,j,k+0.5)\;-H_y^{n+0.5}(i+0.5,j,k-0.5)\;\right)$$

(2. 16)

$$E_y^{\,n+1}(i,j+0.5,k)\;=\;\frac{2\varepsilon-\sigma\Delta t}{2\varepsilon+\sigma\Delta t}\left(E_y^{\,n}(i,j+0.5,k)\;\right)+$$

$$\frac{\Delta t}{(2\varepsilon+\sigma\Delta t)\,\Delta z}\left(H_x^{n+0.5}(i,j+0.5,k+0.5)\;-H_x^{n+0.5}(i,j+0.5,k-0.5)\;\right)-$$

$$\frac{\Delta t}{(2\varepsilon+\sigma\Delta t)\,\Delta x}\left(H_z^{n+0.5}(i+0.5,j+0.5,k)\;-H_z^{n+0.5}(i-0.5,j+0.5,k)\;\right)$$

(2.17)

$$E_z^{\,n+1}(i,j,k+0.5)\;=\;\frac{2\varepsilon-\sigma\Delta t}{2\varepsilon+\sigma\Delta t}\left(E_y^{\,n}(i,j,k+0.5)\;\right)+$$

$$\frac{\Delta t}{(2\varepsilon+\sigma\Delta t)\,\Delta x}\left(H_y^{n+0.5}(i+0.5,j,k+0.5)\;-H_y^{n+0.5}(i-0.5,j,k+0.5)\;\right)-$$

$$\frac{\Delta t}{(2\varepsilon+\sigma\Delta t)\,\Delta y}\left(H_x^{n+0.5}(i,j+0.5,k+0.5)\;-H_x^{n+0.5}(i,j-0.5,k+0.5)\;\right)$$

(2.18)

Before applying these FDTD time-stepping expressions, the "Yee cells" filling up the computational geometrical volume will be assigned with the appropriate permittivity, permeability and conductivity values in terms of the corresponding media. Then an electromagnetic excitation and initial electric field E values are specified at t = 0.

The appearance of half time steps in equations from (2.13) to (2.18) indicates that

E and H fields are calculated alternately. The new value of a field vector component at any lattice point depends only on its previous values and on the previous values of the field vector components at the adjacent points. For example, at t = 0.5Δt, H fields are calculated from the knowledge of E fields at the adjacent points at t = 0 using equations from (2.13) to (2.15). Then the new H fields values are kept for calculating E fields in the future. At the next time step t = Δt, E fields are computed from the saved values of H fields at the neighbour points at t = 0.5Δt using equations from (2.16) to (2.18). The updated E fields values are saved for calculating H fields at the next time step t = 1.5Δt. This iteration process continues for as long as the steady-state behavior is achieved and the response is of interest. It is illustrated in Fig. 2.1.2. Due to the nature of the interleaved calculations of the E & H fields, this algorithm is often referred to as the "leapfrog" scheme.

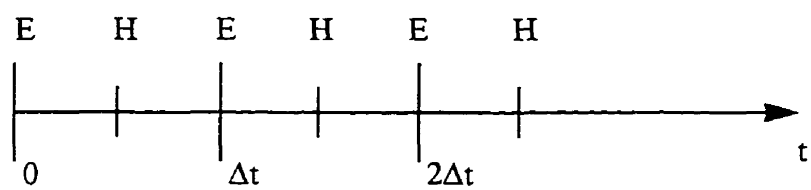

Fig. 2.1.2 The "Leapfrog" Scheme to Calculate Electromagnetic Fields

Thus, at each time step, the system of equations updating the field components is fully explicit. The analytical expense is low and the numerical expense is high. However, the method is efficient since it only stores the field distribution at one moment in memory instead of working with a large system matrix. Furthermore, unlike the moment method and the finite-element method, there is no need to solve matrix inversion.

2.3 Numerical Stability

The iteration process may not converge unless the time increment Δt is chosen correctly. In this case, FDTD is said to be unstable. The condition for numerical stability can be obtained by decomposing FDTD algorithm into separate time and space eigenvalue problems and requiring that the complete spectrum of spatial eigenvalues contained within the stable range [16]. The resulting stability criterion places an upper limitation on Δt as shown below:

$$c_{max}\Delta t \le \frac{1}{\sqrt{\frac{1}{(\Delta x)^2} + \frac{1}{(\Delta y)^2} + \frac{1}{(\Delta z)^2}}} \tag{2.19}$$

where c_{max} is the maximum wave phase velocity expected within the media, including inhomogeneous isotropic media. Equation (2.19) is also known as CFL (Courant, Friedrichs and Lewy) stability criterion. Physically, it states that the time step Δt must be less than the shortest time taken for wave to travel between the adjacent cells to satisfy causality. Namely, any one of Δx, Δy, Δz should be small enough to be compared to the shortest wavelength. Generally, max(Δx, Δy, Δz) should be less than $\lambda/20$ [17], under which the uncertainty in the computed field magnitude will be less than 2%.

2.4 Numerical Dispersion

Besides numerical stability, the inherent errors of a numerical scheme are also important. Numerical dispersion is one of the most important sources of errors in the application of FDTD algorithm. It is caused by the fixed spatial segmentation of space into rectangular grids, which appear different electric sizes for waves of different frequency. Consequently, this dispersion causes the phase and group velocities to be dependent on frequencies. Hence, an electromagnetic pulse will distort when passing through FDTD grids. A detail analysis of this phenomena was reported by A. Taflove [26][18].

In a homogeneous medium, the numerical dispersion during FDTD computation can be reduced to any desired degree if only FDTD grids are fine enough. The pulse distortion can be limited by obtaining the Fourier spatial frequency spectrum of the desired pulse and selecting a grid cell size such that the principle spectral components are resolved with 10-20 cells per wavelength. Such grid division will limit the spread of numerical phase velocities of the principle spectral components to less than 1%, regardless of the wave propagation angle in the grid.

2.5 Interface Between Media

FDTD time-stepping algorithm (2.13) to (2.18) are suitable for most media encountered in microwave engineering. However, special care must be taken when calculating the fields lying between two different media. Generally, there are two types of cases that need to be considered. One is the interface between dielectric and conductor and the other is the interface between two different types of dielectric materials. First of all, it is assumed that the material boundaries will always lie on a plane defined by two tangential E fields and one normal H field. Namely, all the media interfaces coincide with the edge of the "Yee Cells".

The interface between a dielectric and a conductor can be handled by simply assigning all fields on the boundary, i.e. the components of the electric field parallel to and the component of the magnetic field perpendicular to the boundary, constantly to zero. This is similar to the "Electric Walls" boundary conditions often encountered in solving electromagnetic problems.

For the interface between two types of dielectric material, including dielectric and dielectric, dielectric and the air, the standard FDTD expressions can still be used to calculate the normal component of H since the value of μ doesn't change across the interface of two different dielectric. Nevertheless, the tangential E fields lying on the boundary must be calculated using different FDTD expressions. Supposing that there is an interface plane lying in the y-z plane between two different dielectric materials with parameters (σ_1, ε_1) and (σ_2, ε_2) respectively, it can be shown that the E_y and E_z can be expressed in the following equations [11]:

$$\frac{\sigma_1+\sigma_2}{2}E_y+\frac{\varepsilon_1+\varepsilon_2}{2}\frac{\partial E_y}{\partial t}=\frac{\partial H_x}{\partial z}-\frac{\Delta H_z}{\Delta x} \tag{2.20}$$

$$\frac{\sigma_1+\sigma_2}{2}E_z+\frac{\varepsilon_1+\varepsilon_2}{2}\frac{\partial E_z}{\partial t}=\frac{\Delta H_y}{\Delta x}-\frac{\partial H_x}{\partial y} \tag{2.21}$$

These equations are derived from the field continuity conditions across the boundary as given in Appendix A. After discretizing (2.20) and (2.21) using the usual difference central scheme, the resulting expressions are of the same form as equations (2.17) and (2.18) except that the average values of the parameters of the media are used. As a result, the interfaces between different dielectric materials in the FDTD simulation are handled by substituting the average values for the parameters of the materials involved.

2.6 Absorbing Boundary Conditions

A basic consideration with the FDTD approach to solve electromagnetic wave interaction problems is that many geometries of interest are defined in "open" regions where the spatial domain of the computed field is unbounded in one or more coordinate directions. Obviously, no computer can store an unlimited amount of data and therefore the field computation domain must be truncated in size. The computation domain must be large enough to enclose the structure of interest, and a suitable boundary condition on the outer perimeter of the domain must be used to simulate its extension to infinite. Depending on their theoretical basis, the outer grid boundary conditions can be called either radiation boundary conditions (RBC) or absorbing boundary condition (ABC).

ABCs can not be obtained directly from the numerical algorithms for Maxwell's curl equations expressed by the finite-difference time-domain formulas from (2.13) to (2.18). It's mainly because these formulas employ a central spatial difference scheme that requires the knowledge of the field one-half space cell to each side of the observation point. Central difference can not be implemented at the outmost lattice points, since by definition there is no information concerning the fields at points one-half space cell outside of these points. Although backward finite differences could conceivably be used, these are generally of lower accuracy for a given space discretization and have apparently not been used in the major FDTD algorithm.

There have been many ABCs until now along with the extensive use of FDTD. The quest for a new ABC that produces negligible reflections has been and continues to be an active area of FDTD research. Most of the popular ABCs can be grouped into those that are derived from differential equations and those that employ a material absorber. Differential-based ABCs are generally obtained by factoring the wave equation, and by allowing a solution which permits only outgoing waves. These ABCs include Engquist and Madja ABC, Liao ABC, Mur ABC [19] etc.. Material-based ABCs, on the other hand, are constructed so that fields are dampened as they propagate into an absorbing medium. Berenger's PML ABC belongs to this category [20]. Other techniques sometimes used are exact formulations and superabsorption, for example, Mei-Fang Superabsorption is a kind of error cancellation method [21].

Partial differential equations that permit wave propagation only in certain directions are called one-way wave equations. The most popular form of these equations are derived by Engquist and Majda [22] and has been used to solve numerical electromagnetic problems. In their derivations, the ABC is obtained from the approximation of pseudo-difference operators which result from factoring the wave equations. The scalar wave equation in rectangular coordinates is:

$$\frac{\partial^2 U}{\partial x^2}+\frac{\partial^2 U}{\partial y^2}+\frac{\partial^2 U}{\partial z^2}-\frac{\partial^2 U}{\partial t^2}\frac{1}{c^2} = 0 \tag{2.22}$$

or

$$LU = 0 \tag{2.23}$$

where:

$$L \equiv \frac{\partial^2}{\partial x^2}+\frac{\partial^2}{\partial y^2}+\frac{\partial^2}{\partial z^2}-\frac{\partial^2}{\partial t^2}\frac{1}{c^2} \equiv D_x^2+D_y^2+D_z^2-\frac{1}{c^2}D_t^2 \tag{2.24}$$

is a partial differential operator which can be factored in the following way [23]:

$$LU = L^{+}L^{-}U \tag{2.25}$$

with L^- defined as:

$$L^{-} = D_x-\frac{D_t}{c}\sqrt{1-\left(\frac{cD_y}{D_t}\right)^2-\left(\frac{cD_z}{D_t}\right)^2} \tag{2.26}$$

The definition L^+ is similar except a position sign is used after the first term.

It has been shown that the application of L^- to the function U at a planar boundary at x = 0, will completely absorb plane waves travelling in the -x direction independent of the incident angles [22]. The L^+ operator produces the same effect for a plane wave propagating in the x direction and at a boundary $x = +x_0$.

L^+ and L^- are classified as pseudo-differential operators for the inclusion of square-root functions in their definition which makes the direct numerical implementations of these operators impossible. In actual application, the square-root function (2.26) is often approximated using the Taylor series expansions as follows.

One term approximation is given in (2.27):

$$\sqrt{1-\left(\frac{cD_y}{D_t}\right)^2-\left(\frac{cD_z}{D_t}\right)^2} \approx 1 \tag{2.27}$$

Two terms approximation is given in (2.28):

$$\sqrt{1-\left(\frac{cD_y}{D_t}\right)^2-\left(\frac{cD_z}{D_t}\right)^2} \approx 1-\frac{1}{2}\left[\left(\frac{cD_y}{D_t}\right)^2+\left(\frac{cD_z}{D_t}\right)^2\right] \tag{2.28}$$

Substituting (2.27) or (2.28) into (2.26), then the first and second order ABCs for absorbing waves travelling in the -x direction are obtained. The first and second order ABC are given in (2.29) and (2.30) respectively.

$$\frac{\partial U}{\partial x}-\frac{1}{c}\frac{\partial U}{\partial t} = 0 \tag{2.29}$$

$$\frac{\partial^2 U}{\partial x \partial t}-\frac{1}{c}\frac{\partial^2 U}{\partial t^2}+\frac{c}{2}\left(\frac{\partial^2 U}{\partial y^2}+\frac{\partial^2 U}{\partial z^2}\right) = 0 \tag{2.30}$$

The ABCs in (2.29) and (2.30) have to be converted to forms suitable for integration with the FDTD algorithm. Mur proposed one scheme which is so popular that the resulting equations named after him as Mur ABC. Let $U^n(0, j, k)$ represent a tangential component of E or H at the x = 0 boundary, as illustrated in Fig. 2.1.3. The Mur scheme approximates the partial derivative of (2.29) as numerical central differences expanded about the auxiliary U component, $U^n(0.5, j, k)$, located one-half space cell from the grid boundary. Firstly, the mixed x and t derivative is written as:

$$\left.\frac{\partial^2 U}{\partial x \partial t}\right|_{0.5, j, k}^{n} = \frac{1}{2\Delta t}\left(\left.\frac{\partial U}{\partial x}\right|_{0.5, j, k}^{n+1} - \left.\frac{\partial U}{\partial x}\right|_{0.5, j, k}^{n-1}\right) \tag{2.31}$$

$$= \frac{1}{2\Delta t}\left[\frac{U^{n+1}(1, j, k) - U^{n+1}(0, j, k)}{\Delta x} - \frac{U^{n-1}(1, j, k) - U^{n-1}(0, j, k)}{\Delta x}\right]$$

Next, the second time derivative is written as the average of the second time derivatives at the adjacent points (0,j,k) and (1,j,k):

$$\left.\frac{\partial^2 U}{\partial t^2}\right|_{0.5, j, k}^{n} = \frac{1}{2}\left(\left.\frac{\partial^2 U}{\partial t^2}\right|_{0, j, k}^{n} - \left.\frac{\partial^2 U}{\partial t^2}\right|_{1, j, k}^{n}\right)$$

$$= \frac{1}{2}\left[\frac{U^{n+1}(0, j, k) - 2U^{n}(0, j, k) + U^{n-1}(0, j, k)}{\Delta t^2}\right]$$

$$-\frac{1}{2}\left[\frac{U^{n+1}(1, j, k) - 2U^{n}(1, j, k) + U^{n-1}(1, j, k)}{\Delta t^2}\right] \tag{2.32}$$

The second y derivative is written as the average of the second y derivatives at the adjacent points (0,j,k) and (1,j,k):

$$\left.\frac{\partial^2 U}{\partial y^2}\right|^{n}_{0.5,j,k} = \frac{1}{2}\left(\left.\frac{\partial^2 U}{\partial y^2}\right|^{n}_{0,j,k} - \left.\frac{\partial^2 U}{\partial y^2}\right|^{n}_{1,j,k}\right)$$

$$= \frac{1}{2}\left[\frac{U^n(0,j+1,k) - 2U^n(0,j,k) + U^n(0,j-1,k)}{\Delta y^2}\right]$$

$$-\frac{1}{2}\left[\frac{U^n(1,j+1,k) - 2U^n(1,j,k) + U^n(1,j-1,k)}{\Delta y^2}\right] \tag{2.33}$$

Similarly, the second z derivative is written as the average of the second z derivatives at the adjacent points (0,j,k) and (1,j,k):

$$\left.\frac{\partial^2 U}{\partial z^2}\right|^{n}_{0.5,j,k} = \frac{1}{2}\left(\left.\frac{\partial^2 U}{\partial z^2}\right|^{n}_{0,j,k} - \left.\frac{\partial^2 U}{\partial z^2}\right|^{n}_{1,j,k}\right)$$

$$= \frac{1}{2}\left[\frac{U^n(0,j,k+1) - 2U^n(0,j,k) + U^n(0,j,k-1)}{\Delta z^2}\right]$$

$$-\frac{1}{2}\left[\frac{U^n(1,j,k+1) - 2U^n(1,j,k) + U^n(1,j,k-1)}{\Delta z^2}\right] \tag{2.34}$$

Substituting the expressions (2.31) through (2.34) into (2.30) and solving for $U^{n+1}(0,j,k)$, the following time-stepping equation for U along the x = 0 grid boundary is obtained:

$$
\begin{aligned}
U^{n+1}(0,j,k) &= -U^{n-1}(1,j,k) \\
&+ \left(\begin{array}{l} \dfrac{c\Delta t - \Delta x}{c\Delta t + \Delta x}\left(U^{n+1}(1,j,k) + U^{n-1}(0,j,k) \right) \\ \quad + \dfrac{2\Delta x}{c\Delta t + \Delta x}\left(U^{n}(1,j,k) + U^{n}(0,j,k) \right) \end{array} \right) \\
&+ \frac{(c\Delta t)^2 \Delta x}{2\Delta y^2 (c\Delta t + \Delta x)} \left(\begin{array}{l} U^{n}(0,j+1,k) - 2U^{n}(0,j,k) + U^{n}(0,j-1,k) \\ U^{n}(1,j+1,k) - 2U^{n}(1,j,k) + U^{n}(1,j-1,k) \end{array} \right) \\
&+ \frac{(c\Delta t)^2 \Delta x}{2\Delta z^2 (c\Delta t + \Delta x)} \left(\begin{array}{l} U^{n}(0,j,k+1) - 2U^{n}(0,j,k) + U^{n}(0,j,k-1) \\ U^{n}(1,j,k+1) - 2U^{n}(1,j,k) + U^{n}(1,j,k-1) \end{array} \right)
\end{aligned}
\tag{2.35}
$$

Equation (2.35) is called the second order Mur ABC. The Mur ABCs at the other grid boundaries can be obtained using a similar method. The first order Mur ABC can be obtained by removing y and z terms. At x = 0, the first Mur ABC is:

$$
U^{n+1}(0,j,k) = U^{n}(1,j,k) + \frac{c\Delta t - \Delta x}{c\Delta t + \Delta x}\left(U^{n+1}(1,j,k) - U^{n}(0,j,k) \right) \tag{2.36}
$$

This equation (2.36) can also be used in y and z directions. In this thesis, the first order Mur ABC is used due to the dispersion characteristics of microstrip structures [10-

11] [13] and no special treatment for the fields at the corners.

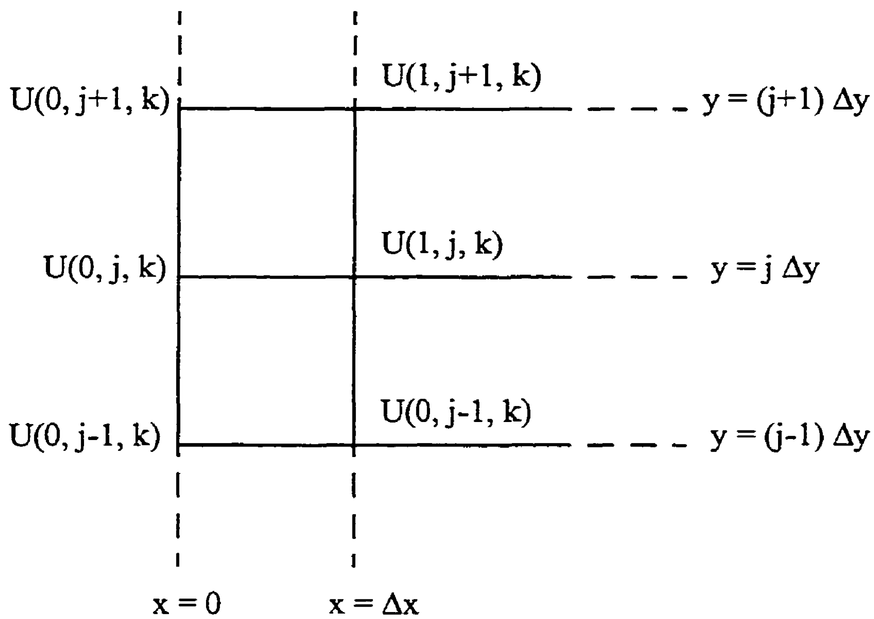

Fig. 2.1.3 Boundary Points at x = 0 Used in the Mur ABC Difference Scheme

2.7 Choice of Excitation

When FDTD was used to solve electromagnetic problems in the early stages, sinusoidal excitation was often used because it is easy to implement. Time stepping is continued until steady-state field values are observed throughout the computational domain. As a result, the structure will be analysed at one frequency per computational cycle. This is similar to other frequency method. It's time costing when the interested band of frequency is wide.

A pulse excitation is one of the best methods proposed to reduce the computational time because one pulse contains extensive frequency spectrum components. It is like injecting many frequencies to the target structure simultaneously and only one analysis cycle is needed. The frequency-domain characteristics can be obtained via the Fourier Transform [10]. However, longer simulation time is usually required and high frequency noise are generated since the bandwidth of a pulse is theoretically infinite. But the advantages of pulse-excited FDTD usually outweight its disadvantages because the overall computational time can be reduced significantly.

Gaussian pulse is a popular choice for pulse-excited FDTD codes. It can be represented in the following formula:

$$g(t) = e^{-(t-t_0)^2/T^2} \tag{2.37}$$

Its Fourier Transform is also Gaussian pulse in the frequency domain:

$$G(f) = \sqrt{\pi}Te^{-\pi^2T^2f^2}e^{-j2\pi ft_0} \tag{2.38}$$

The parameters T & t_0 should be chosen so that:

a. the Gaussian pulse can provide relatively high signal levels within the frequency range of interest to ensure good numerical accuracy;

b. the Gaussian pulse can provide small signal levels for high frequency components which wavelengths are comparative to the step size for reducing noise and instability;

c. the Gaussian pulse must be wide enough to contain enough space divisions for a good resolution after the space discretization interval Δ has been chosen to be fine enough to represent the smallest dimension of the geometry structure and the time discretization interval Δt has been selected small enough to meet the stability criterion;

d. the spectrum of the pulse must be wide enough (or the pulse must still be narrow enough) to maintain a substantial value within the frequency value of interest;

If the last two conditions can not be met simultaneously, the space discretization interval Δ has to be re-chosen.

The pulse width W generally should be greater than 20 space steps. The pulse width is defined as the width between the two symmetric points which have 5 percent of the maximum value of the pulse. It can be estimated using the following formula [11].

$$W = \frac{2\sqrt{3}vT}{\Delta} \tag{2.39}$$

Therefore, T is determined from:

$$T = \frac{10\Delta}{\sqrt{3} \cdot v} \tag{2.40}$$

The maximum frequency which can be calculated is [11]:

$$f_{max} = \frac{1}{2T} = \frac{\sqrt{3} \cdot v}{20 \cdot \Delta} \tag{2.41}$$

where v is the minimum velocity of pulse in the structure under consideration and Δ is the space step. With the specific Δ, f_{max} is high enough to cover the whole frequency range of interest.

The choice of the parameter t_0 should be made so that the initial "turn on" of the excitation will be small and smooth. In the current work, t_0 is set to 3T so that the pulse is down to e^{-9} of its maximum value at the truncation time $t = 0$ or $t = 2t_0$. Since the single precision floating point is used in this study, the choice of t_0 is reasonable.

CHAPTER 3

Analysis of Conventional and Micromachined Microstrip Circuits

In this chapter, three types of microstrip circuits will be analysed. They are: conventional substrate microstrip patch antenna, micromachined and inverted micromachined planar microstrip transmission lines

3.1 Analysis of Conventional Substrate Microstrip Patch Antenna

FDTD method has been used effectively to study the frequency-dependent characteristics of microstrip discontinuities [10-11]. Using 3D FDTD analysis, this section will discuss in detail the application of FDTD, the source of excitation and Absorbing Boundary Conditions to the microstrip line-fed patch antenna to get its time-domain waveforms and calculate the frequency-dependent scattering parameters.

FDTD is chosen because it has many advantages over other methods. Frequency domain analytical work with complicated microstrip circuits has generally been done using planar circuit concepts in which the substrate is assumed to be thin enough that propagation can be considered in two dimensions by surrounding the microstrip with magnetic walls. Fringing fields are accounted for by using either static or dynamic effective dimensions and permittivities. Limitations of these methods are that fringing, coupling and radiation must all be handled empirically since they are not allowed for in the model. The accuracy is also questionable when the substrate becomes thick relative to the width of microstrip line [13]. It's necessary to use full-wave analysis in order to fully account for these effects. Other advantages of FDTD are its extreme efficiency, quite straightforwardness and can be derived directly from Maxwell's equations.

The detailed geometry of the conventional substrate microstrip line-fed rectangular patch antenna is given in the Fig. 3.1.1. It can be modelled easily by FDTD. The total computational mesh dimensions are 60*100*16 in the x, y, z directions respectively. To

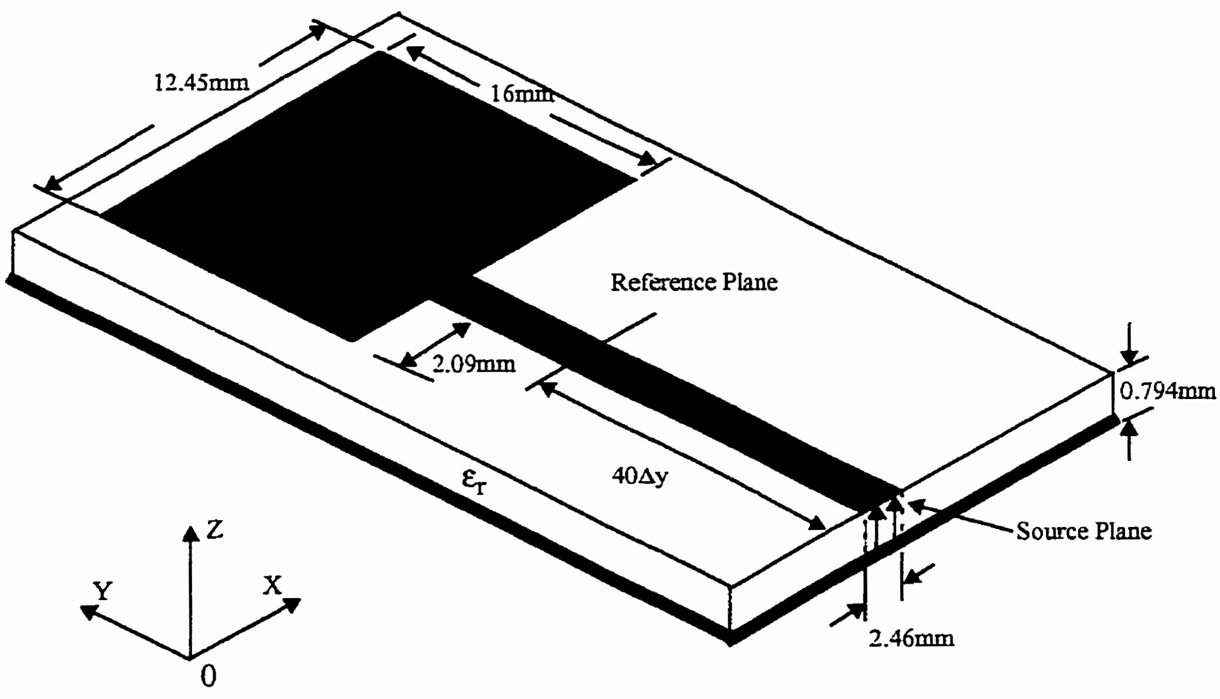

Fig. 3.1.1 Conventional Substrate Microstrip Line-fed Rectangular Patch Antenna

model the thickness of the substrate correctly, Δz is chosen so that three cells exactly match the thickness. Additional 13 nodes are used to model the free space above the substrate. In order to model the patch antenna at x and y dimensions, Δx and Δy have to be chosen so that an integer number of nodes will exactly fit rectangular patch. In this study, the rectangular antenna patch is thus $32\Delta x * 40\Delta y$. The length of the microstrip line from the source plane to the front edge of the patch antenna is $50\Delta y$. The reference plane is placed $40\Delta y$ from the source plane. The microstrip line width is modelled as $6\Delta x$.

In this model, $\Delta x = 0.389$ mm, $\Delta y = 0.4$ mm, $\Delta z = 0.265$ mm, $\Delta t = \Delta z / 2c = 0.4411$ ps. The Gaussian pulse width $T = 15$ ps $= 34\ \Delta t$ and t_0 is set to be 3T so that the Gaussian pulse will be:

$$E_z(t) = e^{-\left(\frac{t - 45 \times 10^{-12}}{15 \times 10^{-12}}\right)^2} (V/m) \tag{3.1.1}$$

Initially, when $t = 0$ all fields in the FDTD computational domain are set to zero. The electrical field E_z is switched on with a Gaussian pulse which can be launched from approximately 0 underneath the microstrip line at the source plane shown in Fig. 3.1.1. The Gaussian pulse waveform in time domain is shown in Fig. 3.1.2 and will be turned off after it passes the source plane. The first order Mur ABC at $y = 0$ will be turned on at the next time step at the source plane. Five Mur ABCs are used to absorb waves travelling in five directions: +x, -x, +y, -y, +z. No ABC is placed at the $z = 0$ plane because there is a ground plane at the bottom of the substrate.

The circuit considered in this study has a conducting ground plane and a single dielectric substrate with metal microstrip line and rectangular patch on the top of this substrate in the common microstrip configuration. These electric conductors are assumed to be perfectly conducting and have zero thickness. The electric field components lying on the conductors are set to be zero. The edge of the conductor should be modelled with one more node with electric field components tangential to the edge of the metal set to be zero.

The Gaussian pulse will propagate along the transmission line until it reaches the junction of the rectangular patch and transmission line. Then a part of the incident pulse will be reflected to the source plane due to the mismatch at this junction and will be absorbed by the ABC at the source plane. The rest of the incident pulse will keep going and will be absorbed by ABC placed at +y end of the computational domain. Fig. 3.1.3 shows that the incident pulse and the reflected response in time domain underneath the microstrip line at the reference plane.

The microstrip line voltage V(t) relative to the ground plane can be obtained by:

$$V(t) = \int_h E_z(t)\, dz \tag{3.1.2}$$

where h is the thickness of the substrate in the z direction.The time domain V(t) can be transformed into frequency domain V(ω) by Discrete Fourier Transform in (3.1.3) :

$$V(\omega) = \int_{-\infty}^{\infty} \left(V(t) \cdot e^{-j\omega t} \right) dt \tag{3.1.3}$$

The return loss S_{11} over a range of frequencies can be obtained from:

$$S_{11}(\omega) = \frac{V_{ref}(\omega)}{V_{inc}(\omega)} = \frac{V_{total}(\omega) - V_{inc}(\omega)}{V_{inc}(\omega)} \tag{3.1.4}$$

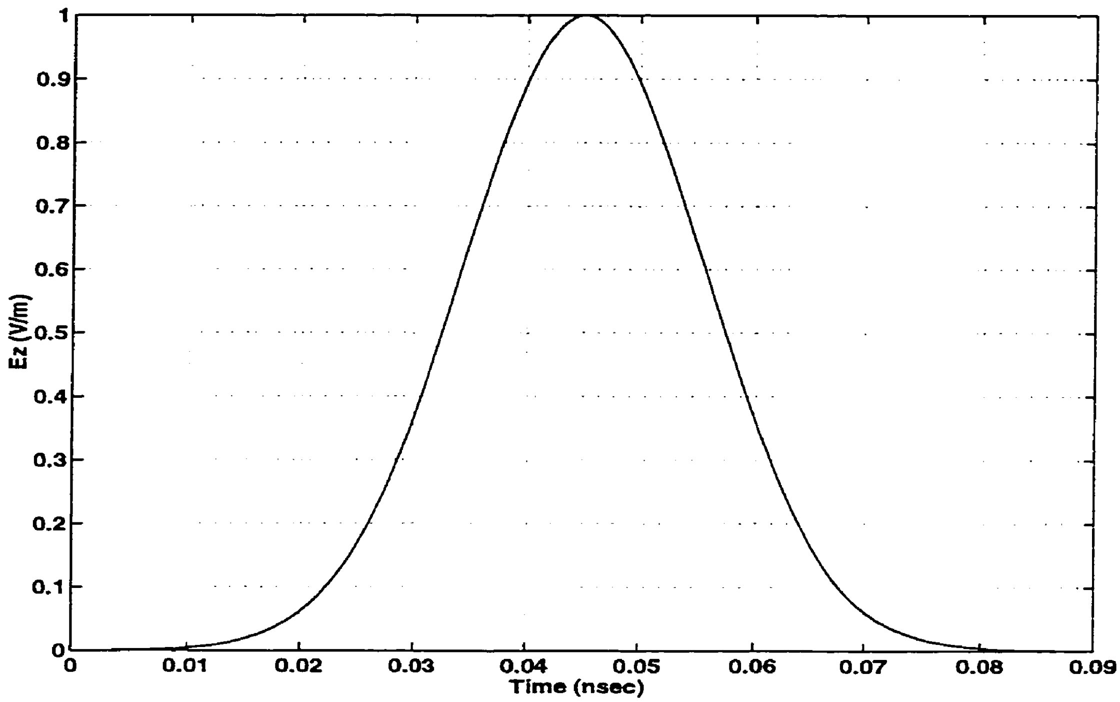

Fig. 3.1.2 Time Domain Gaussian Pulse Waveform used for Excitation of FDTD for Fig. 3.1.1

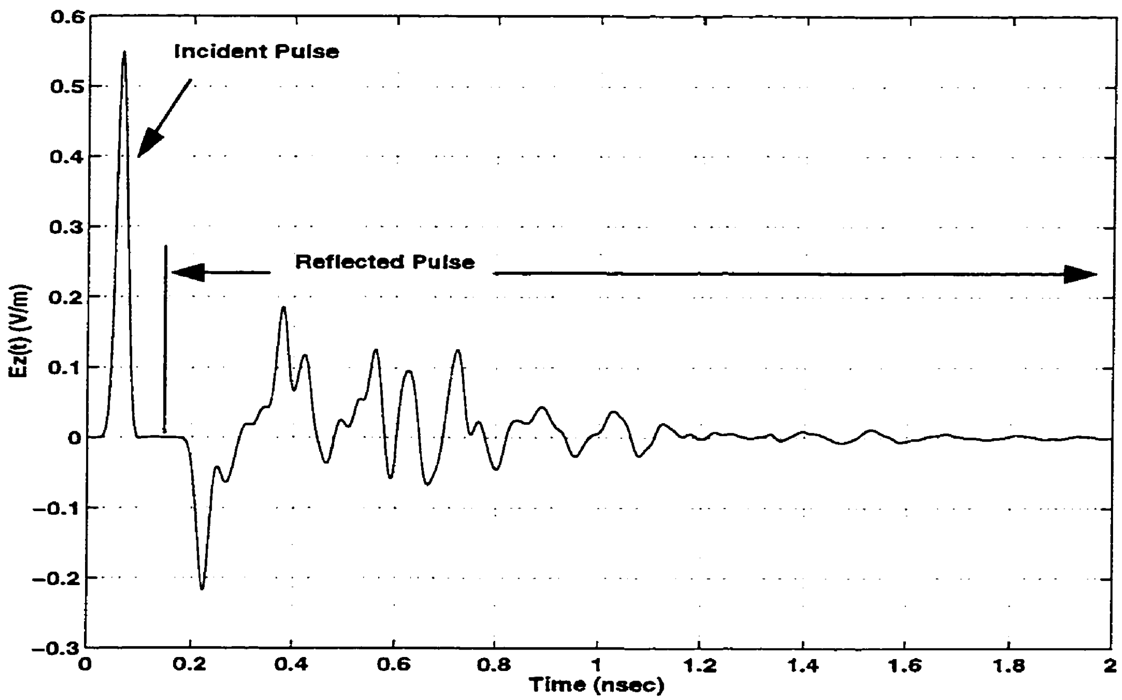

Fig. 3.1.3 Transient E_z Distribution just beneath the Microstrip Line at the Reference Plane

The result of S_{11}, shown in Fig. 3.1.4, agrees very well with the measured result and is better than the published calculated result [13]. Moreover, the field spatial distributions of E_z just underneath the microstrip line at the reference plane along the time steps are shown in Fig. 3.1.5-6 which agree very well with the published results [13]. This demonstrates that programs for FDTD algorithm and ABC used in this study work correctly.

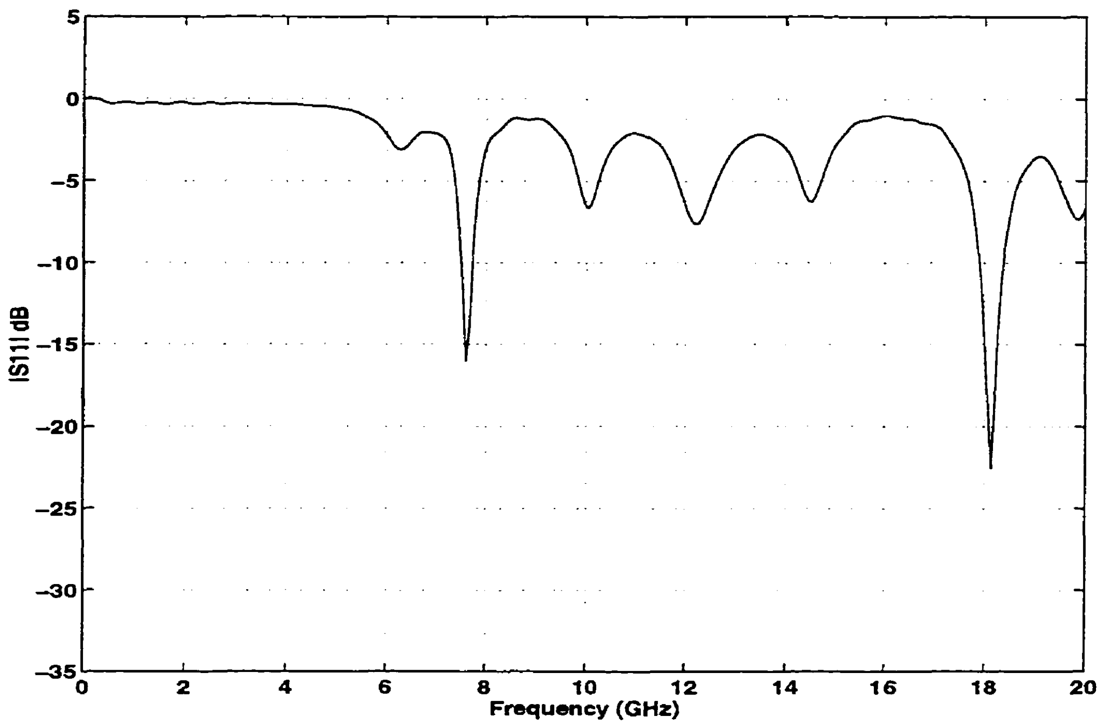

Fig. 3.1.4 Return Loss $|S_{11}|$ for the Microstrip Rectangular Patch Antenna

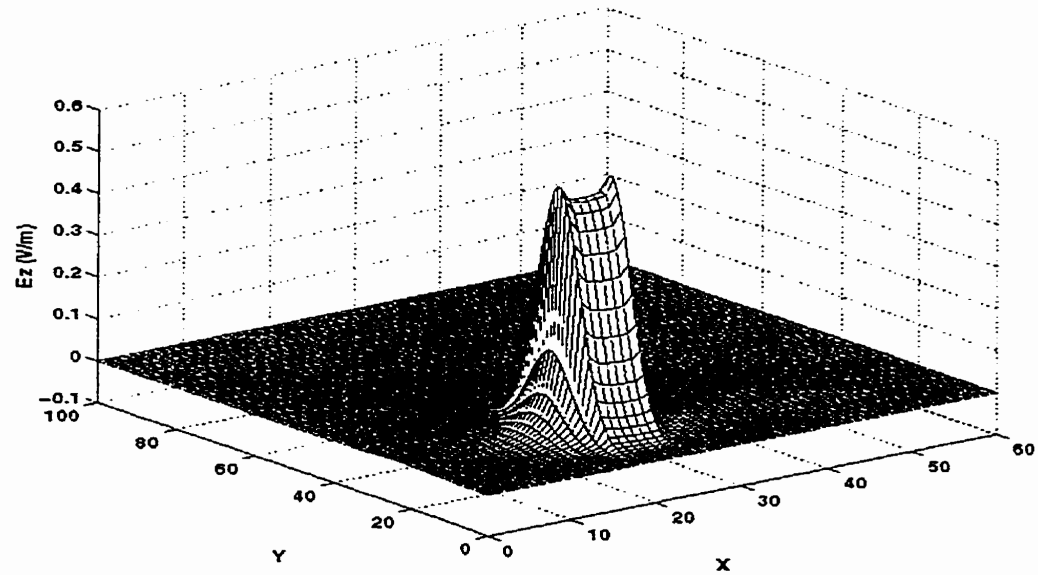

time steps 200

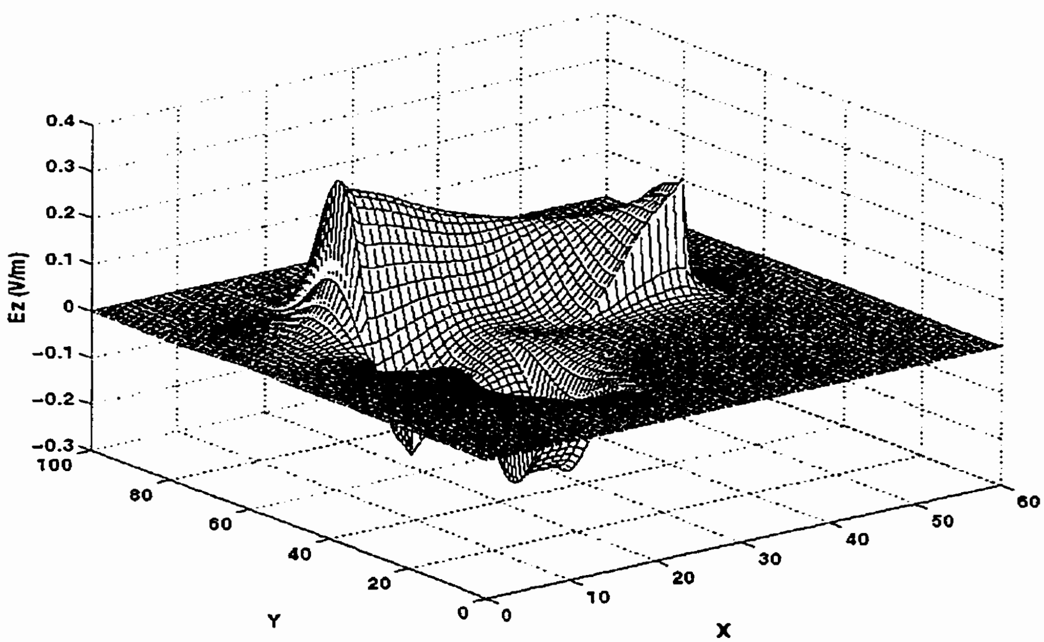

time steps 400

Fig. 3.1.5 The Time Domain Spatial Distributions of E_z beneath the Microstrip Line at the Reference Plane at Time Steps 200, 400

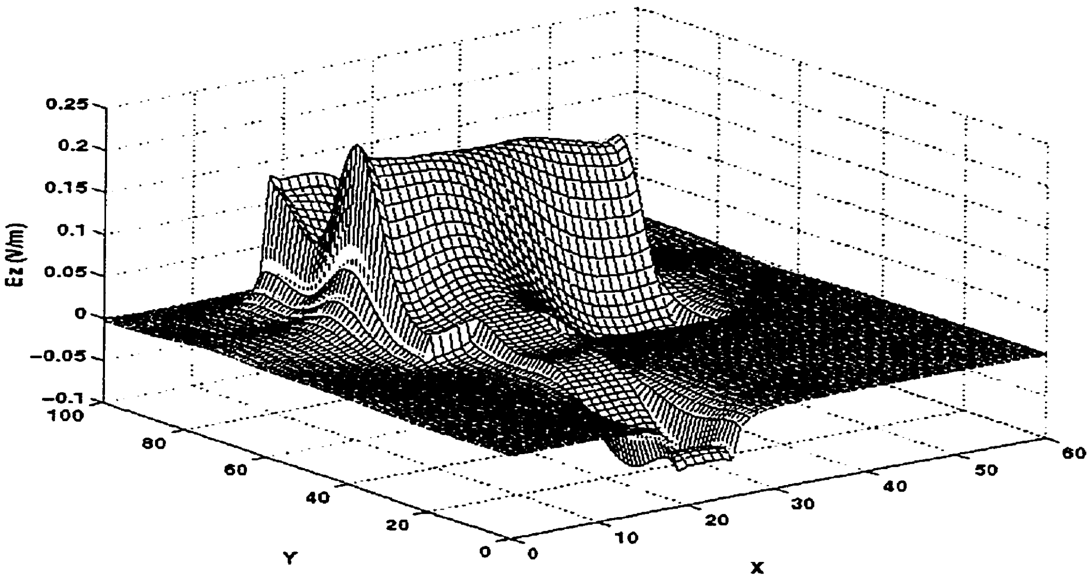

time steps = 600

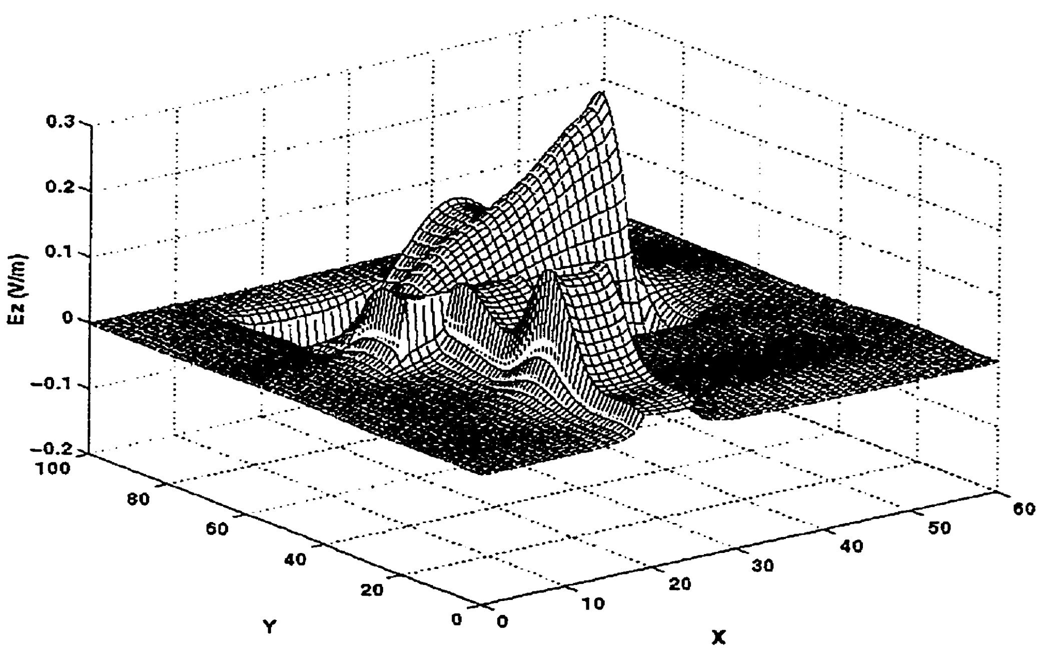

time steps = 800

Fig. 3.1.6 The Time Domain Spatial Distribution of E_z beneath the Microstrip Line at the Reference Plane at Time Steps 600, 800

3.2 Analysis of Micromachined Planar Microstrip Transmission Lines

Micromachined transmission lines are the basis of designing micromachined microwave components and MMIC circuits which will constitute the next generation wireless communication system. However, most of the previous work has focused on experimental measurement. Nevertheless, good theoretical analysis and simulation before fabrication can reduce the design cycle, error and cost greatly. Although a few modellings have been carried out previously by L. Shafai et al. [24-25], more comprehensive, systematic and further study still need to be done.

The types of geometry structures analysed are variations of microstrip lines on a membrane over dielectric substrate on an infinite ground plane. In this study, it is assumed that the fields of the lossy line are not greatly different from the fields of the lossless line [43]. Thus, the perturbation theory is used to avoid the use of the transmission line parameter L, C, R and G, and instead uses the fields of the lossless line.

Fields components in time domain can be obtained from FDTD calculation and consequently be transferred into frequency domain components by Fast Fourier Transform (FFT). From the fields components in frequency domain, effective relative dielectric constant and characteristic impedance can be calculated. As a result, dielectric loss and conductor loss can be calculated through the perturbation theory [24-25] [49-50].

A gaussian pulse was used to excite across the front-end cross section plane ABCD shown in Fig. 3.2.1 which is the general geometry structures of micromachined microstrip transmission lines. Five first order Mur ABCs were used to absorb the propagation waves in +x, -x, +y, -y and +z directions except at z = 0 at which a ground plane is placed. The characteristic impedance of a microstrip line is obtained by $Z(\omega) = V(\omega)/I(\omega)$, where $I(\omega) = \oint_c \boldsymbol{H}_l(\omega)\, dl$, and $V(\omega) = \int_h E_z(\omega)\, dz$. The effective relative permittivity can be calculated from (3.2.1) to (3.2.3),

$$e^{-\gamma(\omega) L} = \frac{E_z(\omega, y = y_2)}{E_z(\omega, y = y_1)}, \qquad L = |y_2 - y_1| \tag{3.2.1}$$

$$\gamma(\omega) = \alpha(\omega) + j\beta(\omega) \tag{3.2.2}$$

$$\varepsilon_{eff}(\omega) = \frac{\beta^2(\omega)}{\varepsilon_0 \mu_0 \omega^2} \tag{3.2.3}$$

where $\gamma(\omega)$, $\alpha(\omega)$ and $\beta(\omega)$ are the complex propagation constant, attenuation constant and phase constants, respectively. According to the perturbation theory, conductor loss is given by (3.2.4) [49-50] where $R_S(\omega)$, given in (3.2.5), is the surface resistance in the unit

$$\alpha_c(\omega) = \frac{R_S(\omega)}{2Z(\omega)} \cdot \frac{\int_l \boldsymbol{J}^2(\omega)\, dx}{\left(\int_l \boldsymbol{J}(\omega)\, dx\right)^2} \qquad (\text{neper/m}) \tag{3.2.4}$$

Ω/m. $Z(\omega)$ is the characteristic impedance obtained from FDTD calculation. $\mathbf{J}(\omega)$ is the surface current density along the width of microstrip line given by (3.2.6) in y direction.

$$R_s(\omega) = \sqrt{\frac{\omega\mu}{2\sigma}} \tag{3.2.5}$$

$$\mathbf{J}(\omega) = \mathbf{n} \times \mathbf{H}_t(\omega) \tag{3.2.6}$$

In (3.2.5), $\omega = 2\pi f$ is a angle frequency, μ is the permeability, σ is the conductivity. In (3.2.6), $\mathbf{H}_t(\omega)$ is the tangential magnetic field just above the microstrip line. In this study, $\mathbf{H}_t(\omega) = \mathbf{H}_x(\omega)$ because only the currents flowing in the y direction are under consideration. Dielectric loss can be calculated from the following formula (3.2.7) [49-50] where k_0 is the wavenumber in free space, and $\tan\delta$ is the tangential loss of metal microstrip line. The value in the unit of neper/m can be transformed into the unit of db /m by multiplying $20*\log_{10}e$ [43].

$$\alpha_d(\omega) = 0.5 k_0 \varepsilon_r \tan\delta \frac{\varepsilon_{eff}(\omega) - 1}{\left(\varepsilon_r - 1\right)\sqrt{\varepsilon_{eff}(\omega)}} \quad (\text{neper/m}) \tag{3.2.7}$$

The metal microstrip lines and ground planes are assumed to be infinitely thin and the conductor is copper. Substrate parameters are $\tan\delta = 0.0009$, $\varepsilon_{r1} = \varepsilon_{r2} = 2.2$. The conductivity of copper is $5.813*10^7$ S/m. The width of the metal microstrip line is W_2 = 0.0254 cm, the width of groove W_1 varies from 0 cm, $2W_2$, $3W_2$, $4W_2$, to the suspended case in which the bottom substrate is replaced with air or $\varepsilon_{r2} = 1$. In all the calculations, the groove space is filled with air. FDTD parameters used in the modelling process are $dx = dy = dz = 4.233 * 10^{-3}$ cm, $dt = dx / 2c = 7.055 * 10^{-14}$ s. The number of grids in x, y, z direction is: $n_x = 80$, $n_y = 300$, $n_z = 30$ respectively. The gaussian pulse parameters are chosen: $T = 1.05825 * 10^{-12}$ s, $t_0 = 3.17475 * 10^{-12}$ s. According to (2.41), the maximum frequency is higher than 60 GHz.

Micromachined microstrip transmission lines with $h_1 = 0.0127$ cm, $h_2 = 0.0254$ cm, the thickness of the upper and bottom substrate, were studied at first. The calculated effective relative permittivity is shown in Fig. 3.2.2 from which it can be seen that the effective relative permittivity decreases along with the increase of the groove width at all frequencies from 0 to 60 GHz. The result from the commercial simulation software PCAAD for the case $W_1 = 0$ is also provided in Fig. 3.2.2 and is lower than the result of FDTD. In Fig. 3.2.3 the dielectric loss versus frequencies from 0 to 60 GHz is shown. It can be seen that dielectric loss increases linearly with the increase of frequencies at a given groove width. At a given frequency, the dielectric loss of micromachined microstrip transmission line decreases as the groove width increases. Micromachined microstrip transmission line without any groove has the highest dielectric loss at any frequency while the suspended micromachined microstrip transmission line has the lowest dielectric loss at all frequencies. This can be explained that with the increase of the groove width, more and more substrate is replaced with the air, $\varepsilon_r = 1$. Consequently, the effective permittivity and the dielectric loss decrease with the increase of the groove width. Fig. 3.2.4 shows conductor loss versus frequencies from 0 to 60 GHz for micromachined microstrip transmission lines. There is little reduction in the conductor loss with the increase of groove width at any given frequency of interest. However, conductor loss is much higher than dielectric loss at all frequencies. Therefore, in micromachined microstrip transmission lines conductor loss is the main source of resistive loss. The dielectric loss, conductor loss and characteristic impedance from PCAAD for the conventional substrate case ($W_1 = 0$) are also plotted in the Fig. 3.2.3-4. The dielectric loss and conductor loss from FDTD are about

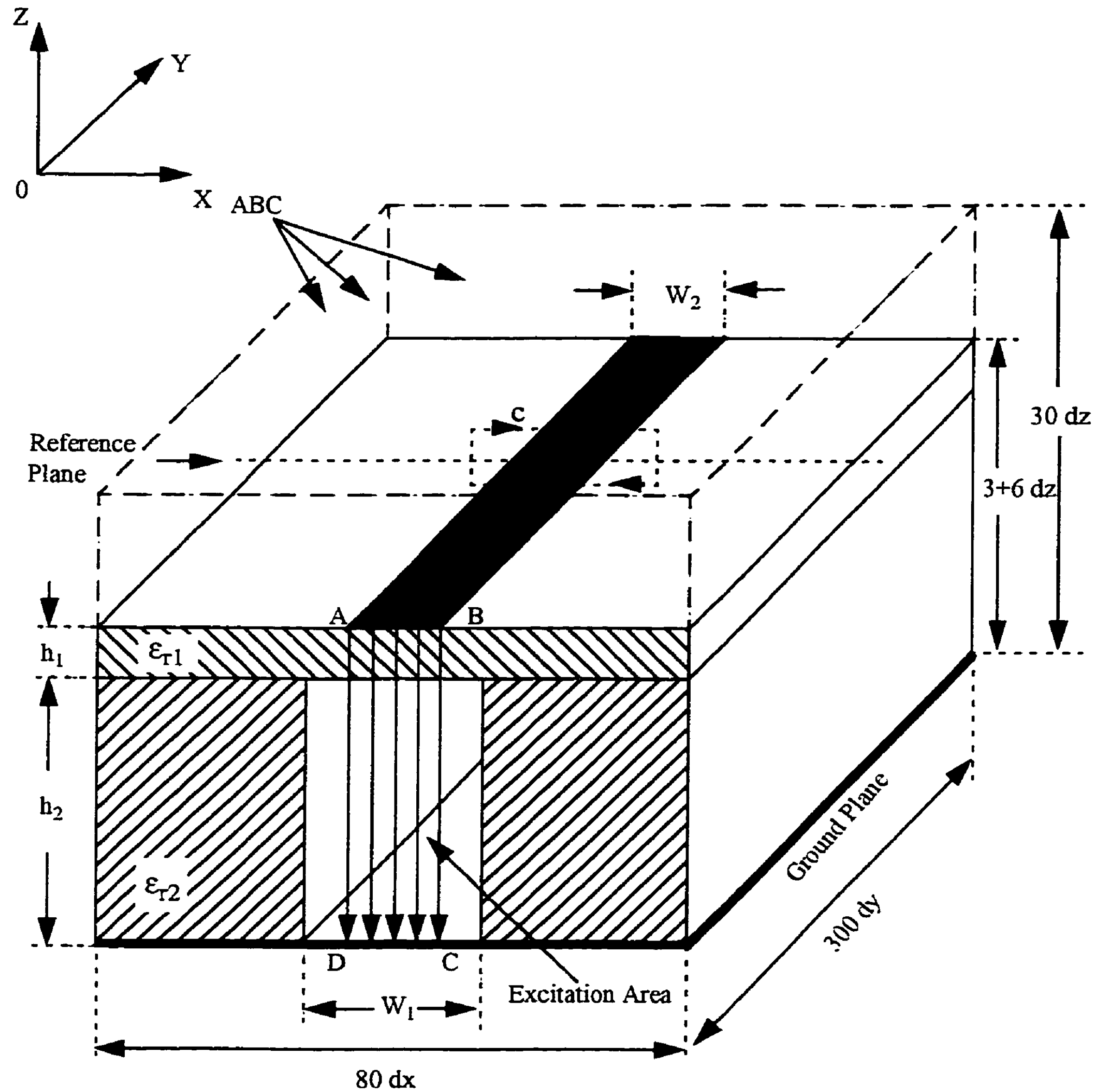

$W_2 = 0.0254$ cm, $\varepsilon_{r1} = \varepsilon_{r2} = 2.2$

$h_1 = 0.0127$ cm $h_2 = 0.0254$ cm $dx = dy = dz = 0.004233$ cm

Fig. 3.2.1 Geometry Structure of Micromachined Microstrip Transmission Line

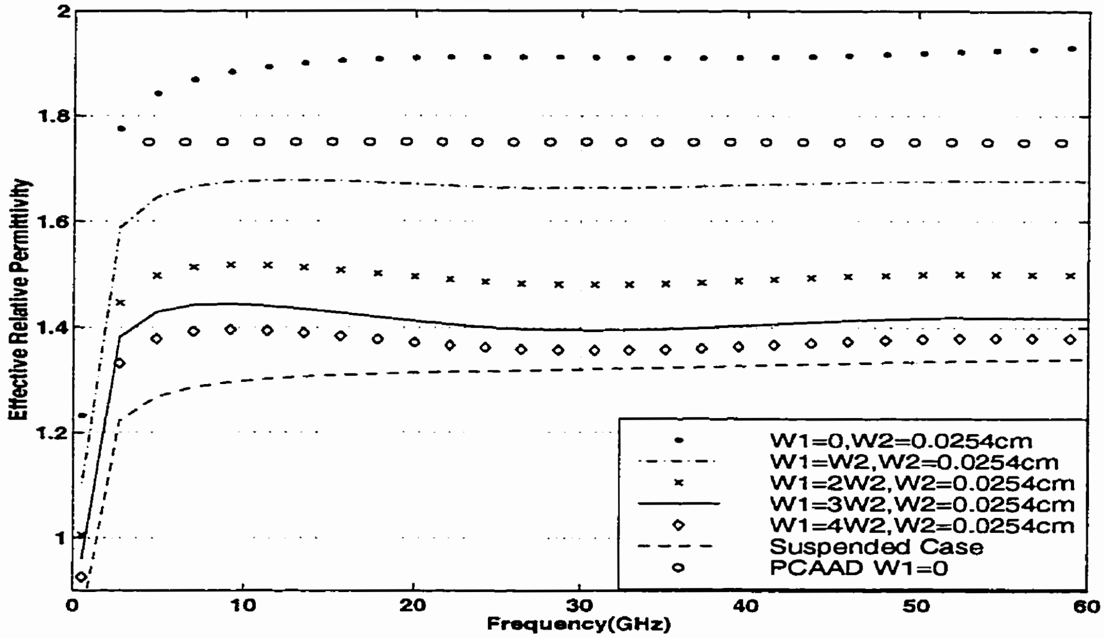

Fig. 3.2.2 Effective Relative Permittivity for Fig. 3.2.1 between Y =130 dy & 150 dy

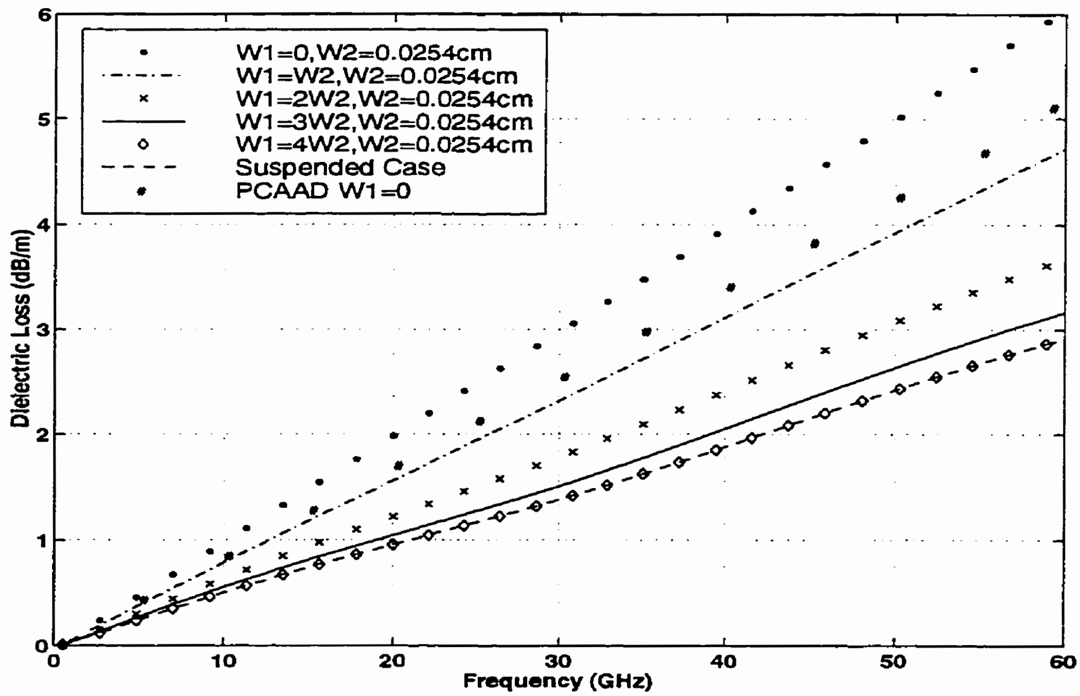

Fig. 3.2.3 Dielectric Loss for Fig. 3.2.1 between Y =130 dy & 150 dy

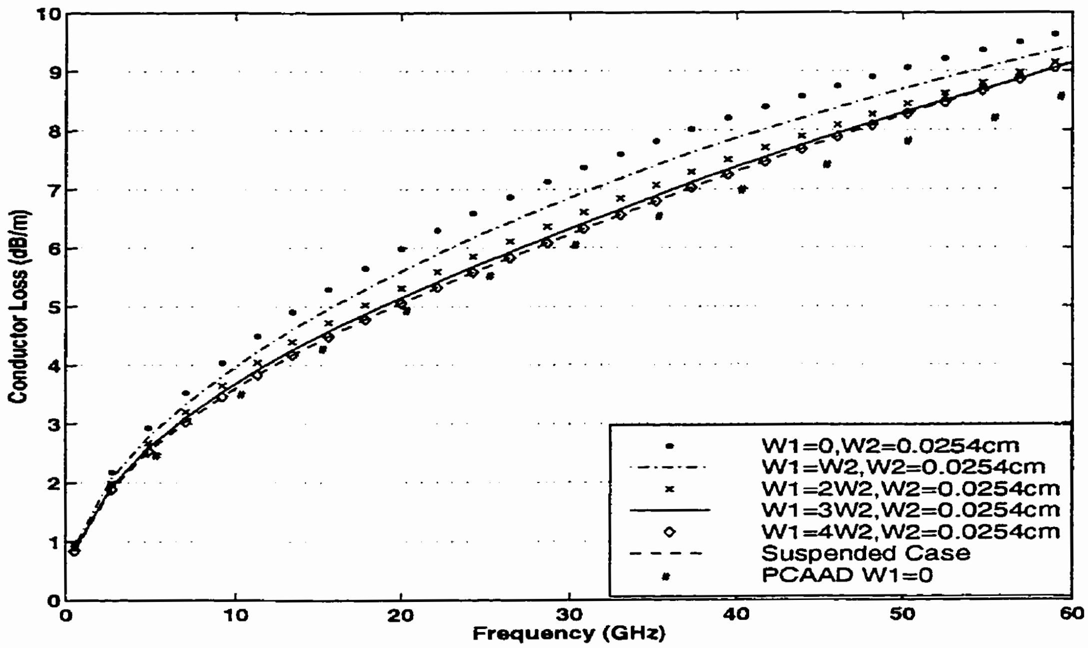

Fig. 3.2.4 Conductor Loss for Fig. 3.2.1 between Y =130 dy & 150 dy

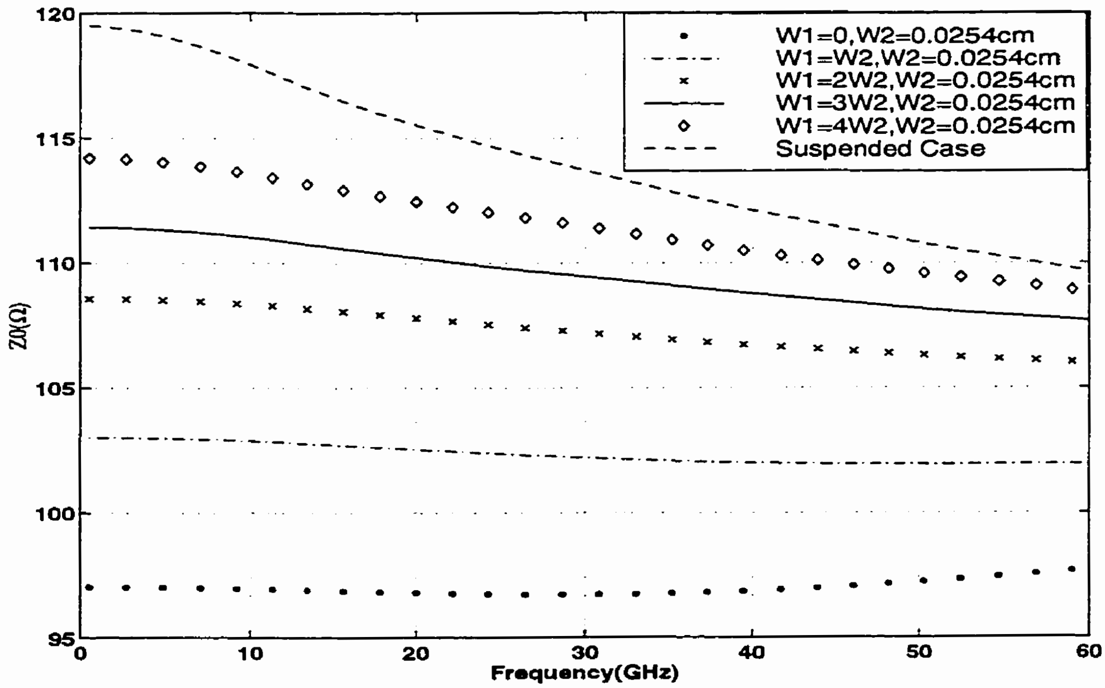

Fig. 3.2.5 Characteristic Impedance for Fig. 3.2.1 at Y = 30 dy

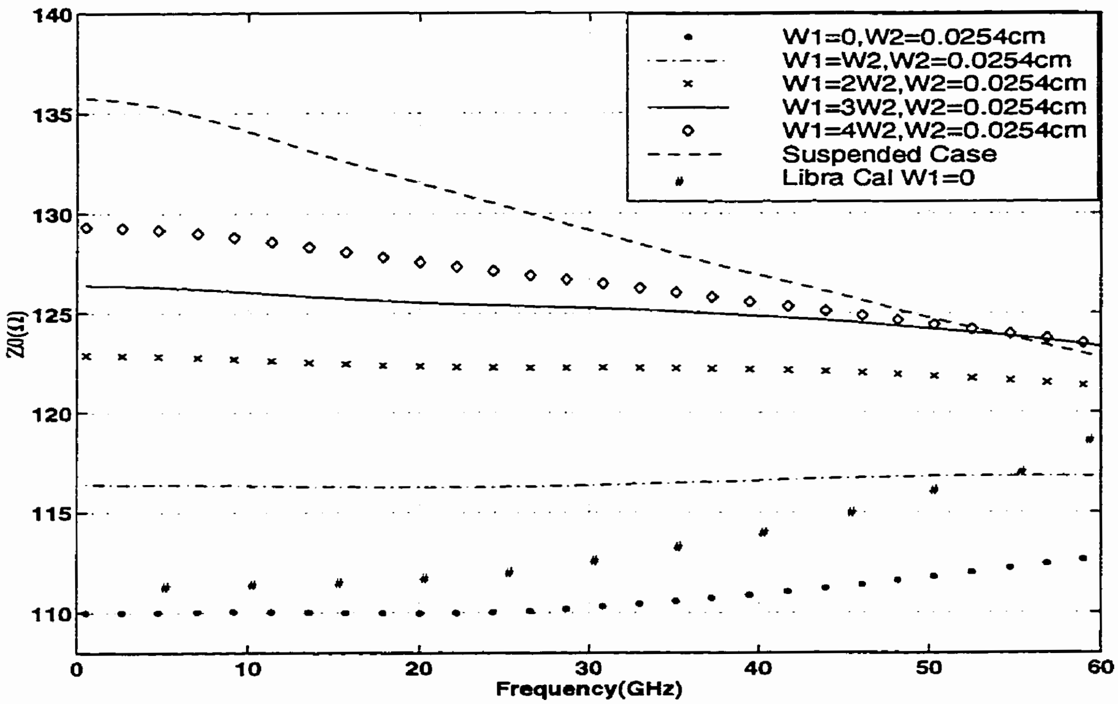

Fig. 3.2.6 Characteristic Impedance for Fig. 3.2.1 at Y = 50 dy

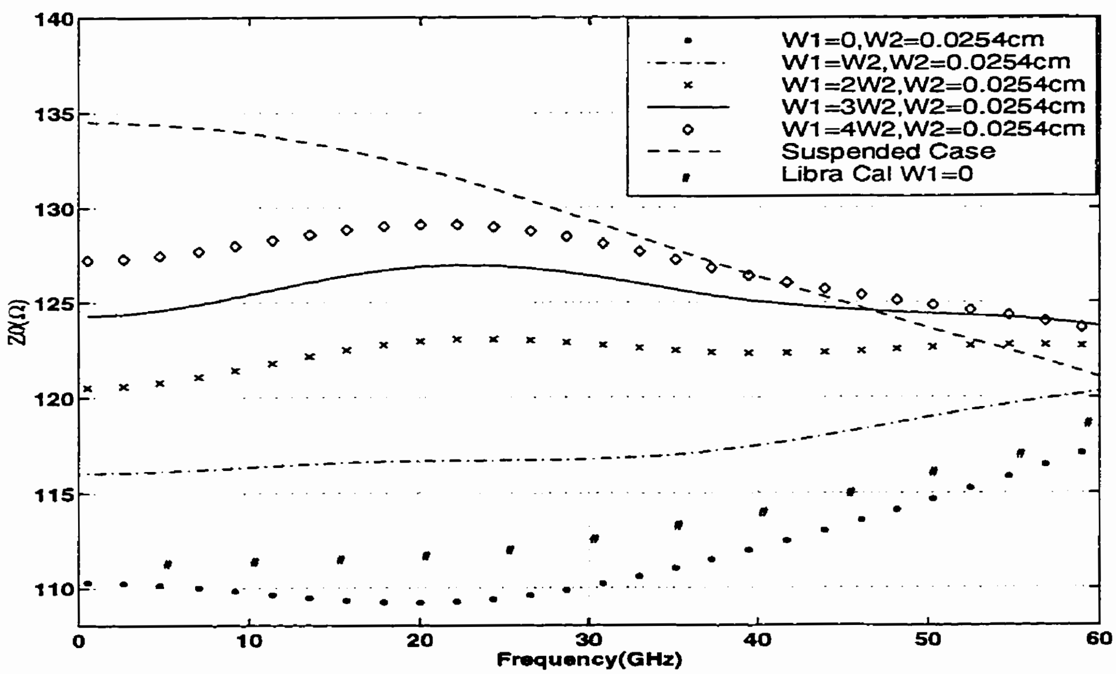

Fig. 3.2.7 Characteristic Impedance for Fig. 3.2.1 at Y = 150 dy

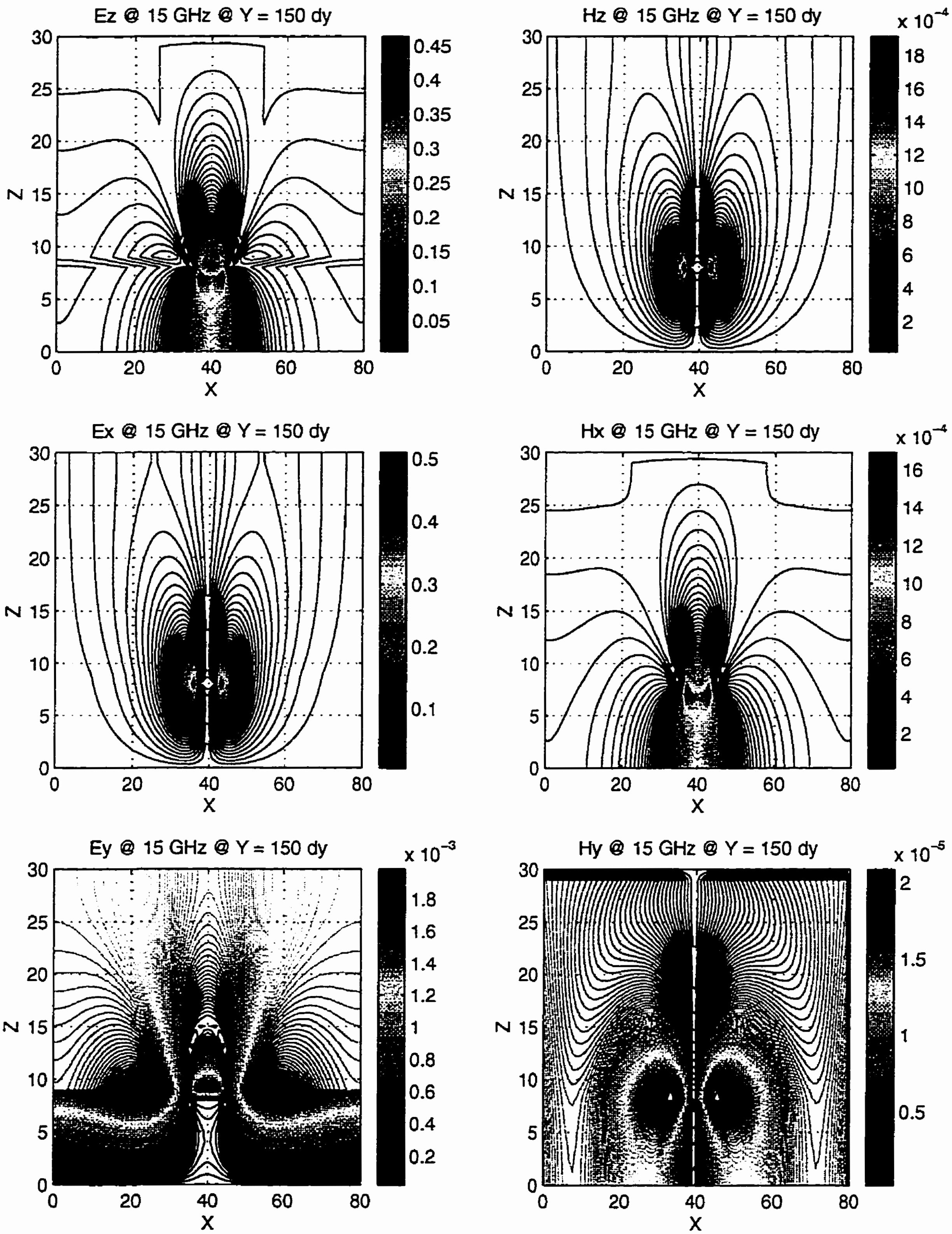

Fig. 3.2.8 Electric & Magnetic Fields Distribution at 15 GHz at Y= 150 dy in X-Z Plane for Fig. 3.2.1 with $W_1 = 0$, Units: E: V/m, H: A/m

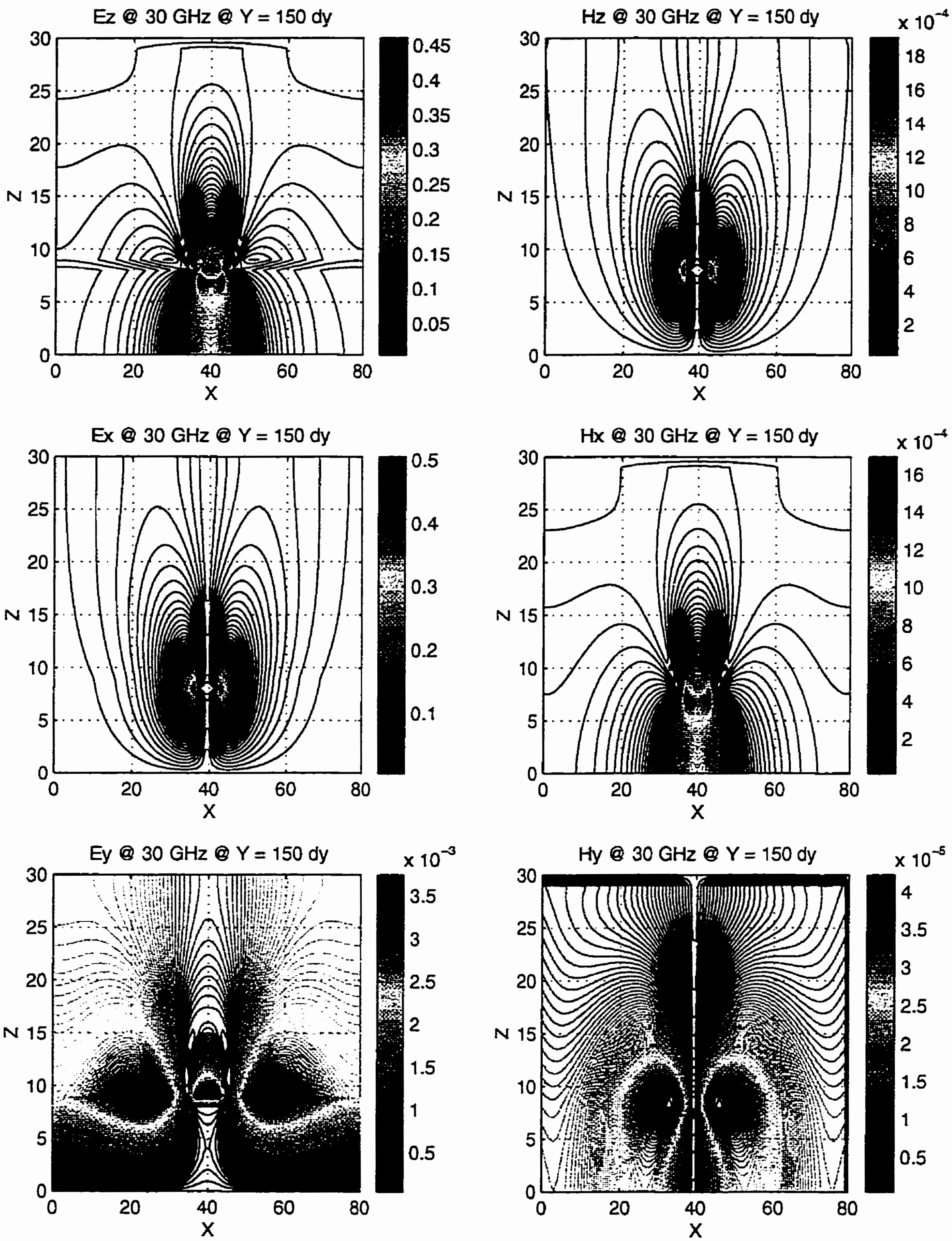

Fig. 3.2.9 Electric & Magnetic Fields Distribution at 30 GHz at Y= 150 dy in X-Z Plane for Fig. 3.2.1 with $W_1 = 0$, Units: E: V/m, H: A/m

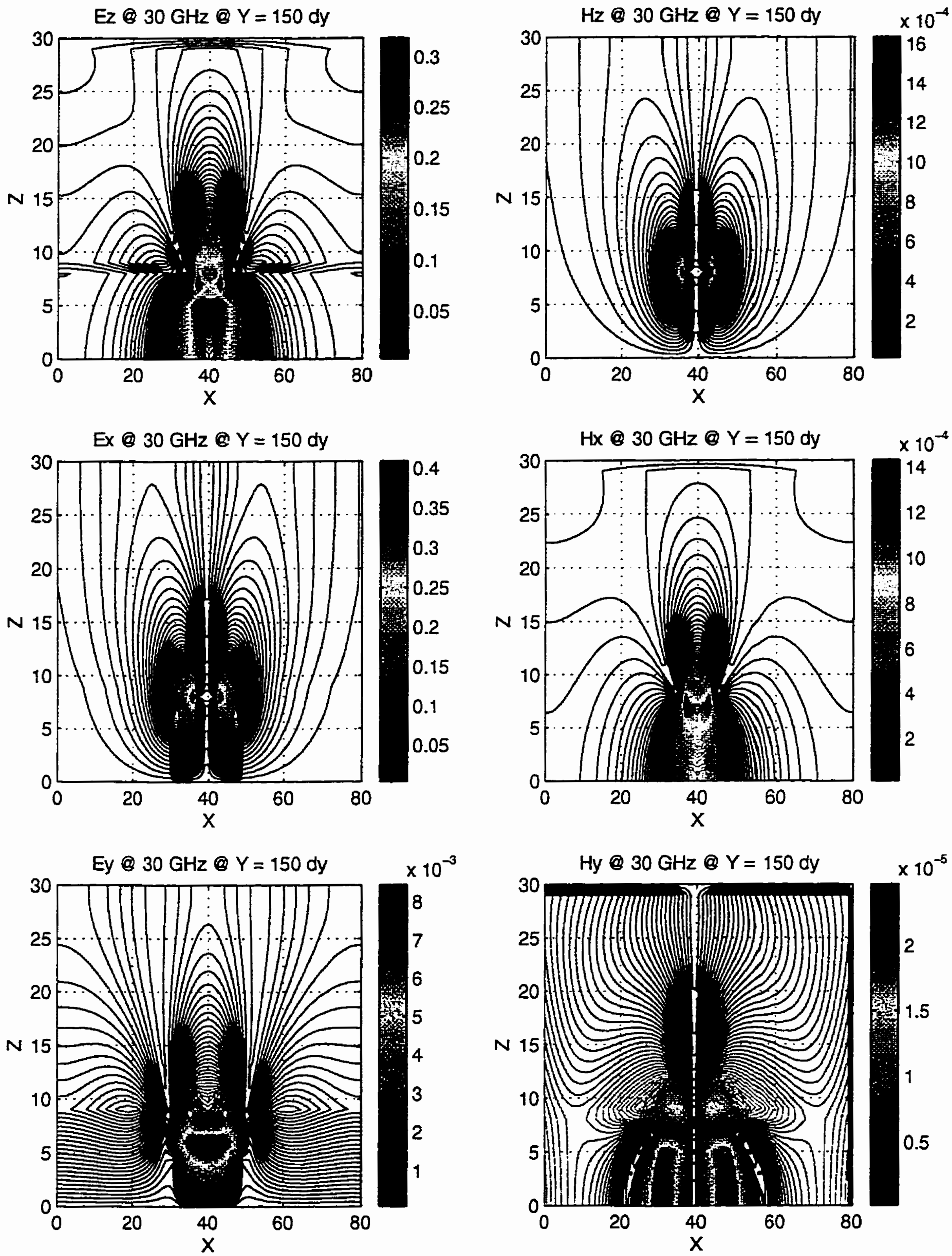

Fig. 3.2.10 Electric & Magnetic Fields Distribution at 30 GHz at Y= 150 dy in X-Z Plane for Fig. 3.2.1 with $W_1 = 3\ W_2$, Units: E: V/m, H: A/m

1 dB/m higher than those from PCAAD at 60 GHz for the case $W_1 = 0$ in Fig. 3.2.3-4. Fig. 3.2.5-7 show characteristic impedances of micro-machined microstrip transmission lines versus frequencies at Y = 30 dy, 50 dy and 150 dy respectively. The characteristic impedance increases with the increase of grooved width for most frequencies in Fig. 3.2.5. For the most groove widths, the characteristic impedance decreases with the increase of frequencies except that the conventional microstrip transmission line at the frequencies higher than 40 GHz. In Fig. 3.2.7 the result of the conventional case $W_1 = 0$ agrees very well with the Libra calculation results. The reason for different characteristic impedances at different positions along y axis is that the electromagnetic wave around the exciting source plane has several modes. When it travels along the +y direction, some modes dies gradually and only quasi-TEM wave exists. That is also why the characteristic impedance at the location far enough from the source plane agrees better with the Libra result. For the suspended case in Fig. 3.2.6-7, when the frequency is close to 60 GHz, the characteristic impedance is even lower than that of the case $W_1 = 3\ W_2$. This needs further investigation. (Fortunately, when the write-up of this thesis was almost done, some encouraging results were obtained from the further study and are appended at the end of this thesis as Appendix B.)

In addition, for the micromachined microstrip transmission lines, the field distributions underneath the microstrip line in frequency domain at 15 & 30 GHz are obtained from FDTD calculation. The six field components distributions of E_x, E_y, E_z, H_x, H_y and H_z for the case of the micromachined microstrip transmission lines for Fig. 3.2.1 with $W_1 = 0$ at 15 & 30 GHz are given in Fig. 3.2.8-9 respectively. The field distributions for the case with $W_1 = 3W_2$ at 30 GHz are shown in Fig. 3.2.10. It is evident that for the conventional microstrip transmission lines without any groove, the most energy of E_y and E_z is focused closely underneath the substrate surface, and E_x concentrates at the both fringes of the conductor microstrip transmission lines. Fig. 3.2.8-9 also show that E_y radiates more towards the outside of the substrate into the free space at high frequencies than it does at low frequencies. However, for the micromachined microstrip transmission lines (groove width $W_1 \neq 0$) in Fig. 3.2.10, all the energy of E_y and E_z are concentrated in the groove which is filled with air. This can explain why the dielectric loss reduces in the micromachined microstrip transmission lines. Moreover, much more information and graphs about this study are shown in [44].

When $h_1 = 0$, the upper substrate in Fig. 3.2.1 is modelled as the infinite thin membrane. The effective relative permittivity, dielectric loss and conductor loss versus frequencies for different groove widths are shown in Fig. 3.2.11-13 respectively. The effective relative permittivity reaches as low as $\varepsilon_r = 1$ at the suspended case just as expected. As a result, the dielectric loss decreases greatly and approaches zero at the suspended case. PCAAD is used to calculate the conventional substrate case and the results are plotted in the corresponding figures too. Fig. 3.2.12-13 show that dielectric loss and conductor loss from FDTD are about 1 dB/m higher than the results from PCAAD for the case $W_1 = 0$ at 60 GHz. Fig. 3.2.14 indicates that characteristic impedance increases from 75 Ω to around 98 Ω with the increase of groove width at all frequencies. The Libra calculation for the characteristics impedance of the conventional microstrip transmission line is also given for comparison in Fig. 3.2.15-16. It is shown that the results of Libra using quasi-static method are about 8 Ω higher than the results of this study which uses FDTD method at all frequencies of interest.

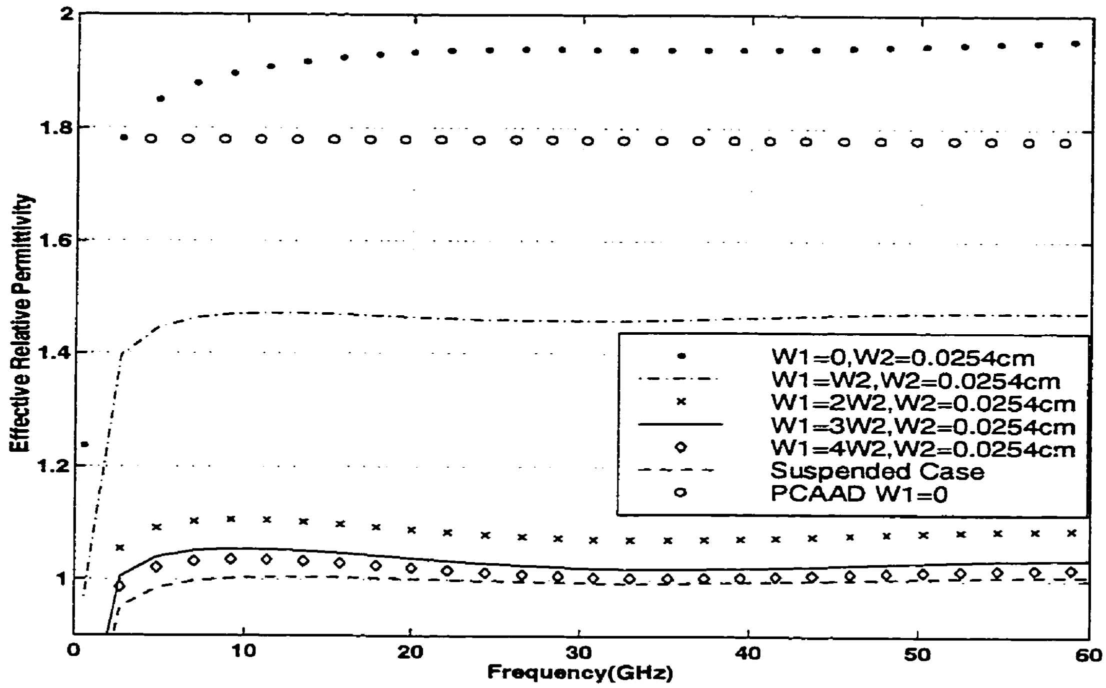

Fig. 3.2.11 Effective Relative Permittivity for Fig. 3.2.1 between Y =130 dy & 150 dy with $h_1 = 0$

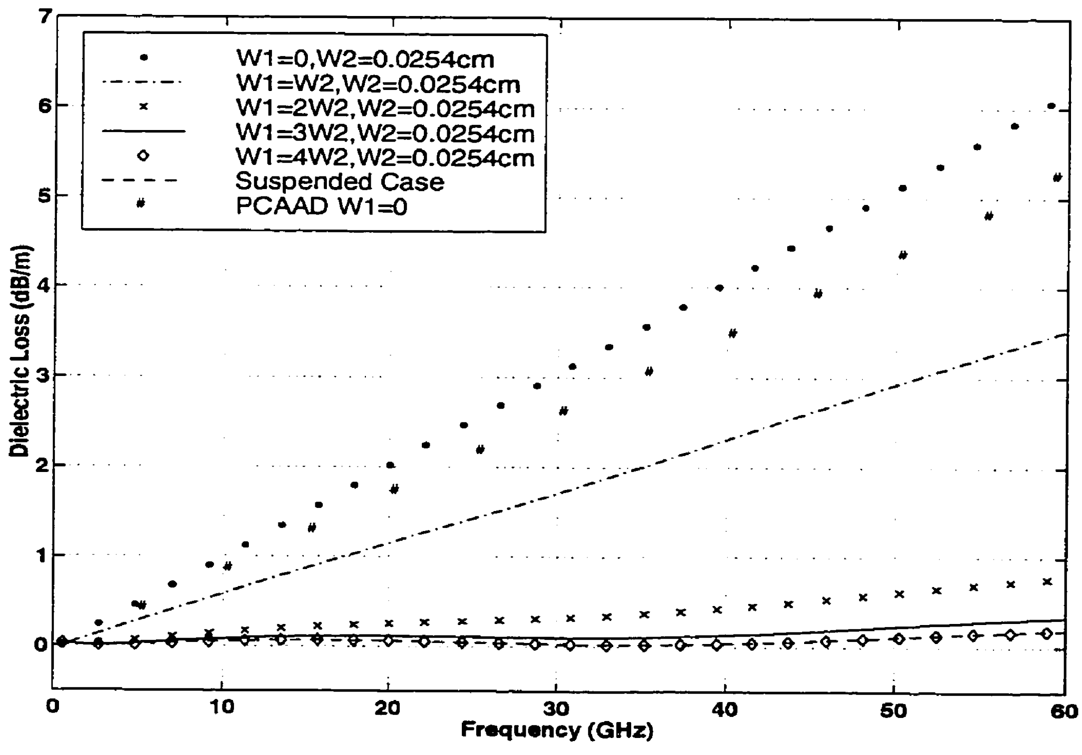

Fig. 3.2.12 Dielectric Loss for Fig. 3.2.1 between Y =130 dy & 150 dy with $h_1 = 0$

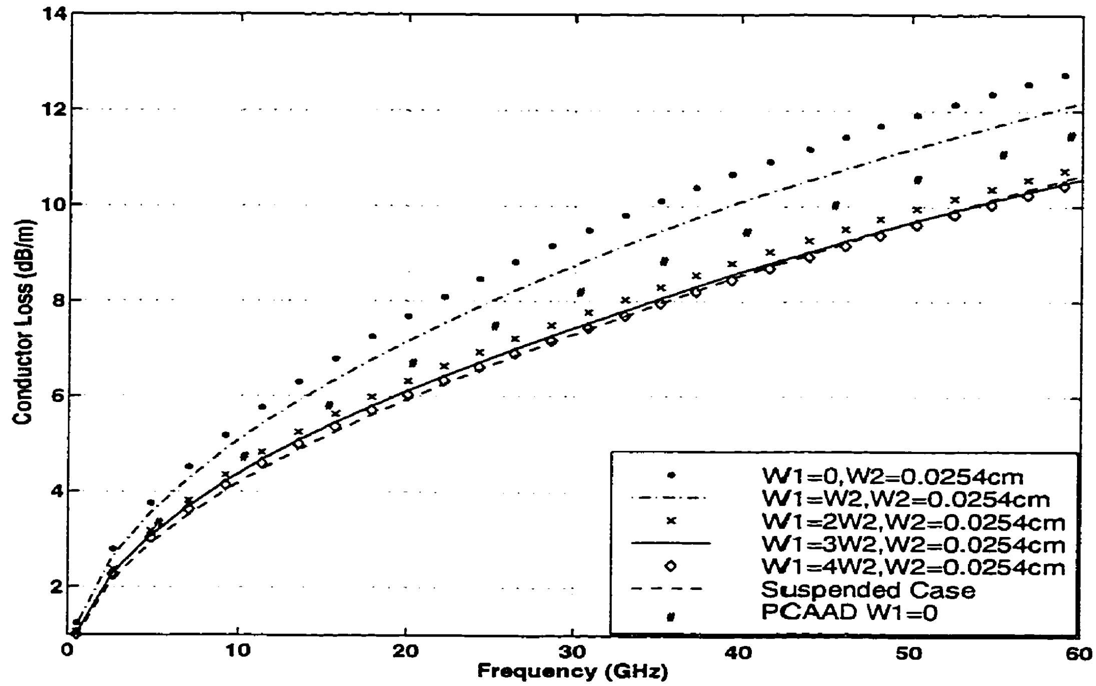

Fig. 3.2.13 Conductor Loss for Fig. 3.2.1 between Y =130 dy & 150 dy with $h_1 = 0$

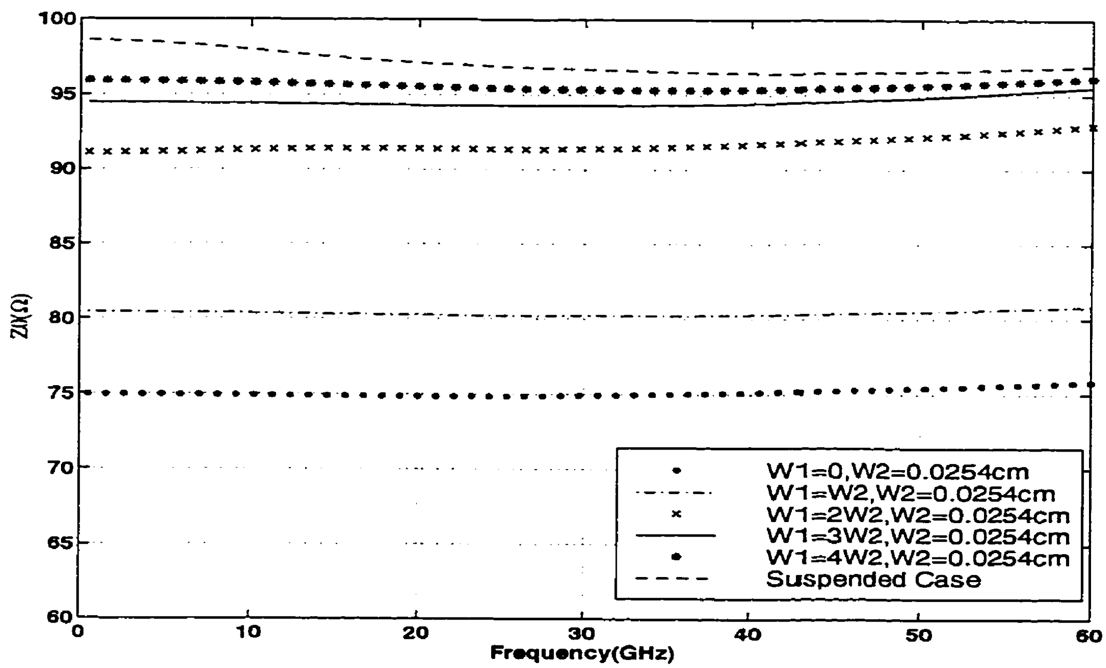

Fig. 3.2.14 Characteristic Impedance for Fig. 3.2.1 with $h_1 = 0$ at Y = 30 dy

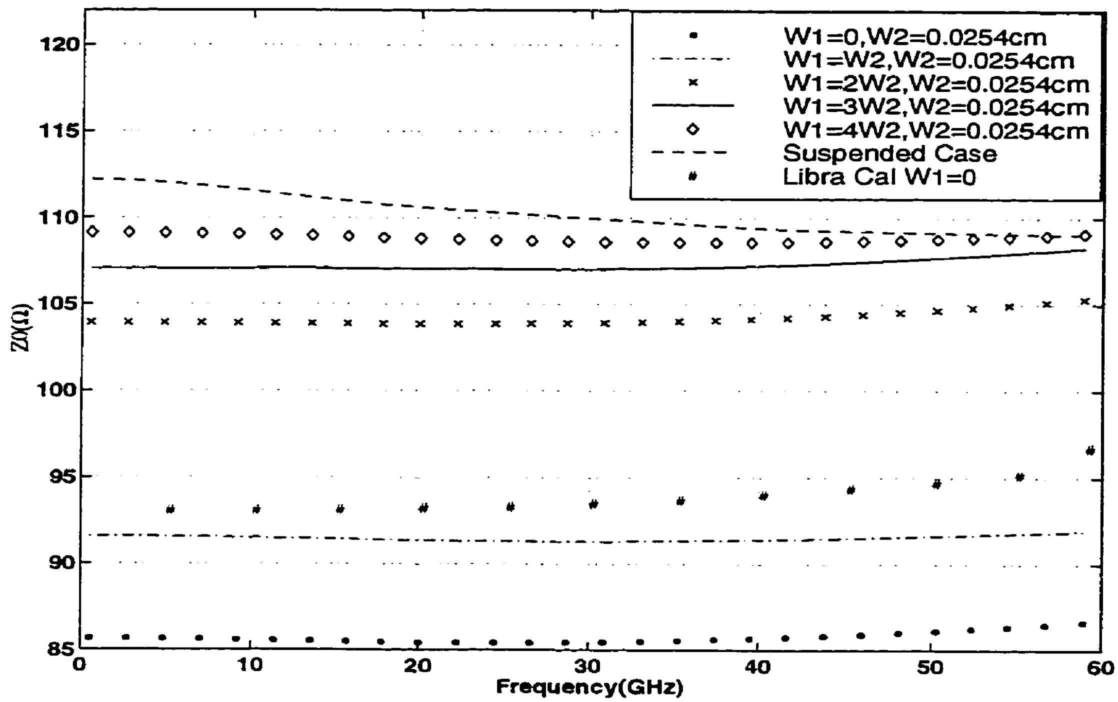

Fig. 3.2.15 Characteristic Impedance for Fig. 3.2.1 with $h_1 = 0$ at Y = 50 dy

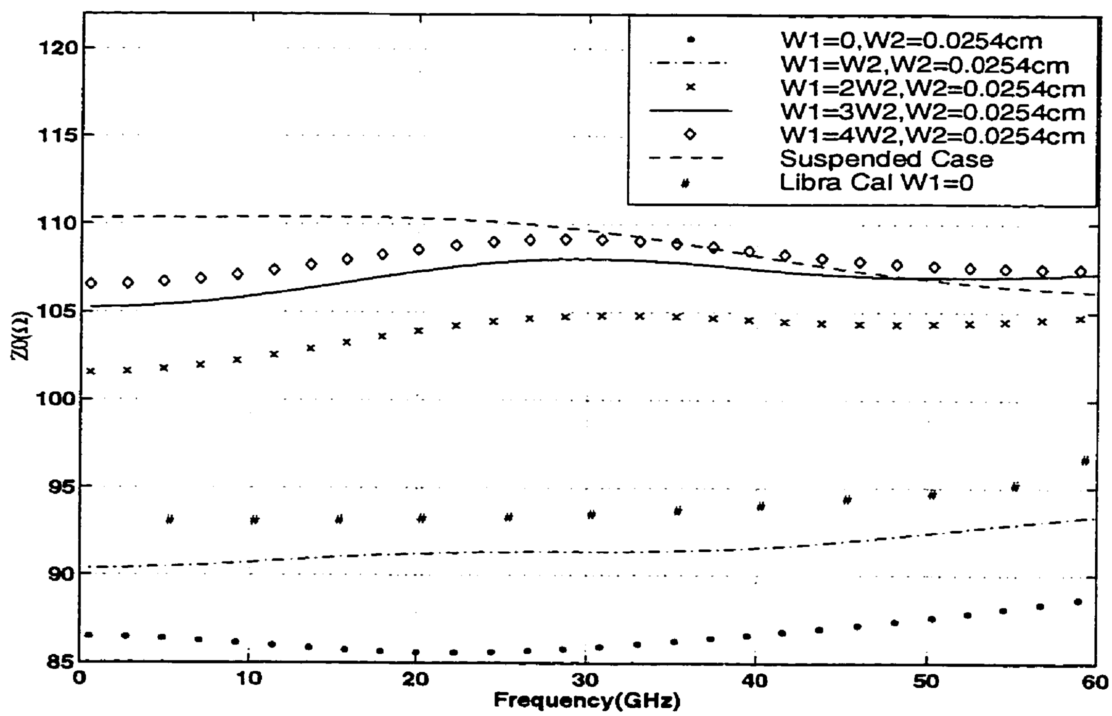

Fig. 3.2.16 Characteristic Impedance for Fig. 3.2.1 with $h_1 = 0$ at Y = 150 dy

3.3 Inverted Micromachined Planar Microstrip Transmission Lines

The inverted micromachined microstrip transmission lines are also studied. The cross-section of the geometry structures is shown in Fig. 3.3.1. The effective relative permittivity, dielectric loss, conductor loss and characteristic impedance are shown in Fig. 3.3.2-7. Conclusions to the inverted micromachined microstrip transmission lines are similar to those obtained from the micromachined microstrip transmission lines.

After comparing these three groups of figures, Fig. 3.2.2-7, Fig. 3.2.11-16 and Fig. 3.3.2-7, for different geometry structures, some conclusions can be obtained. Although an inverted microstrip transmission line with conventional substrate (groove width $W_1 = 0$) has higher dielectric loss in Fig. 3.3.3 than a corresponding conventional microstrip transmission line ($W_1 = 0$) has in Fig. 3.2.12, the other inverted micromachined microstrip transmission lines (groove width $W_1 \neq 0$) have lower dielectric loss than those of the corresponding micro-machined microstrip transmission lines (groove width $W_1 \neq 0$). However, the conductor loss of the inverted micromachined microstrip lines is generally 2 dB higher than that of micromachined counterparts at almost all frequencies and groove widths under the consideration. Moreover, the dielectric loss of the micromachined microstrip transmission lines with two different upper substrate thickness in Fig. 3.2.3 (with h_1 = 0.0127 cm) and Fig. 3.2.12 (with $h_1 = 0$) are also compared. As a result, it is found that the thickness of upper substrate (or membrane) has a great influence to the dielectric loss of the micromachined microstrip transmission lines. The thinner the upper substrate is, the less dielectric loss it will have although the conductor loss does not change too much.

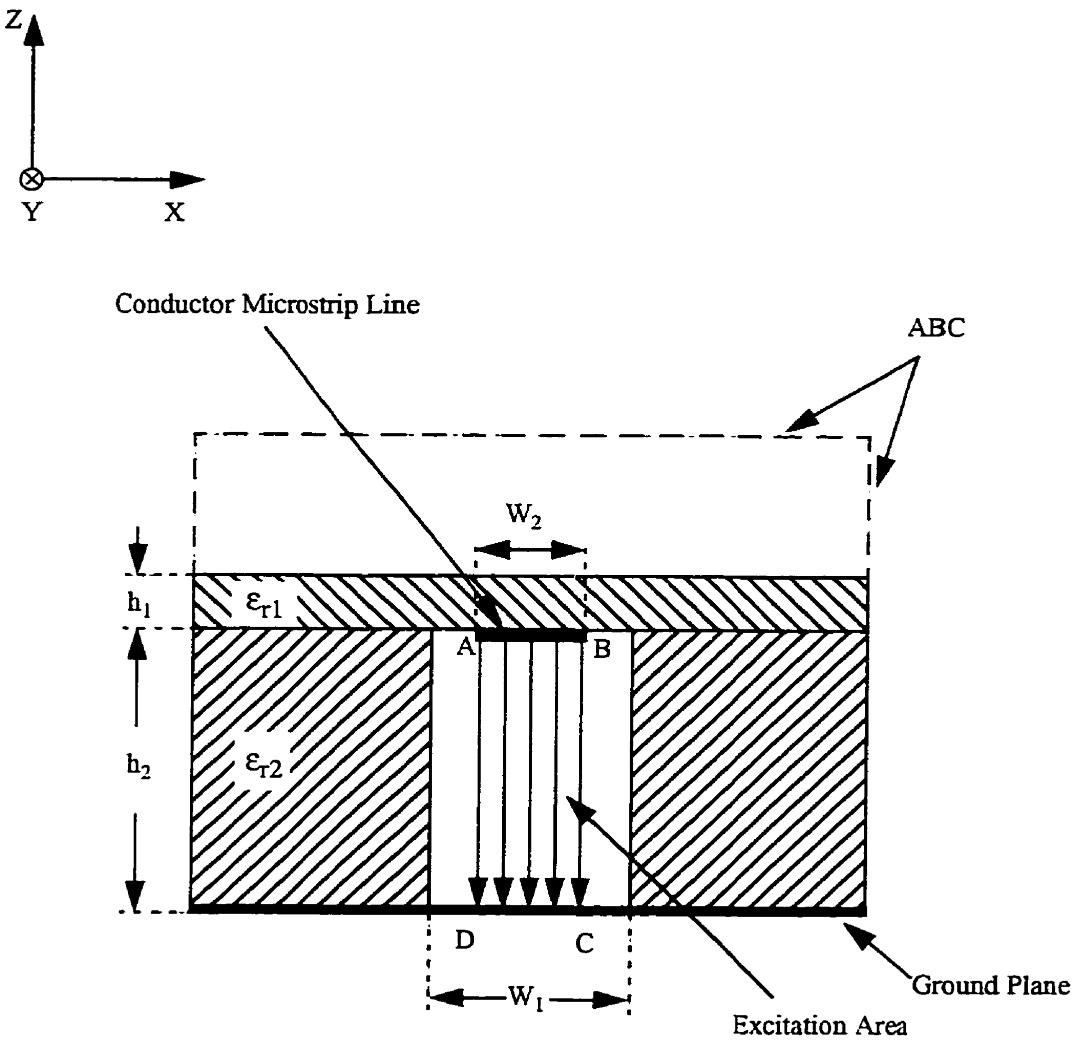

$$W_2 = 0.0254 \text{ cm}, \ \varepsilon_{r1} = \varepsilon_{r2} = 2.2$$

$$h_1 = 0.0127 \text{ cm} \ \ h_2 = 0.0254 \text{ cm}$$

Fig. 3.3.1 Cross Section of Inverted Micromachined Microstrip Transmission Lines

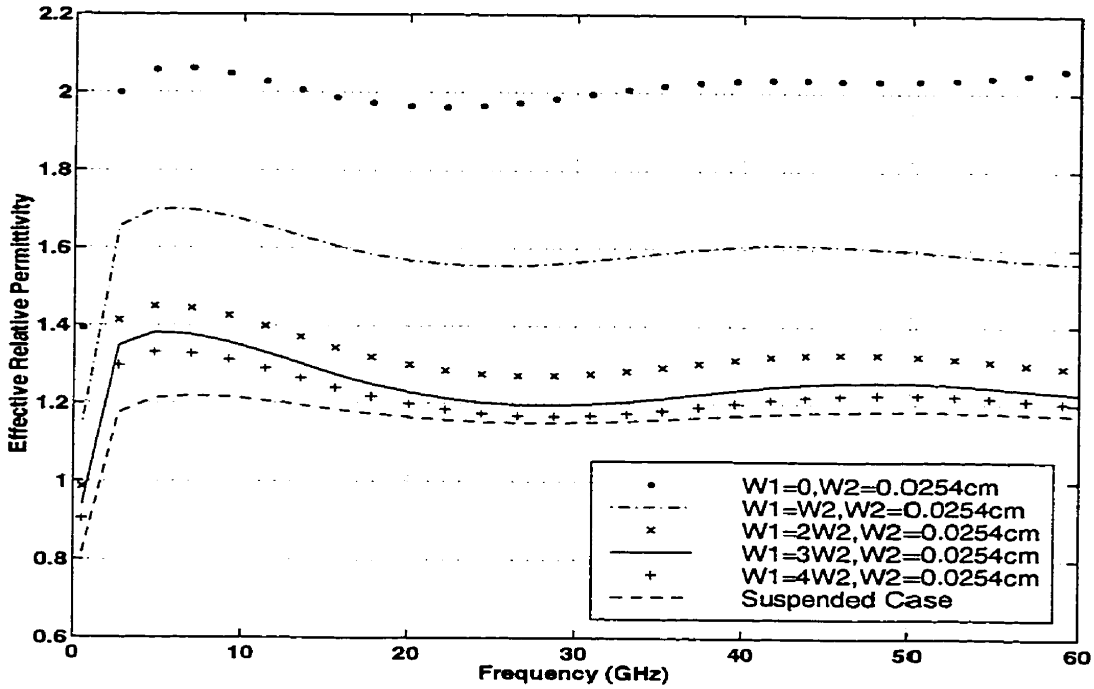

Fig. 3.3.2 Effective Relative Permittivity for Fig. 3.3.1 between Y =130 dy & 150 dy

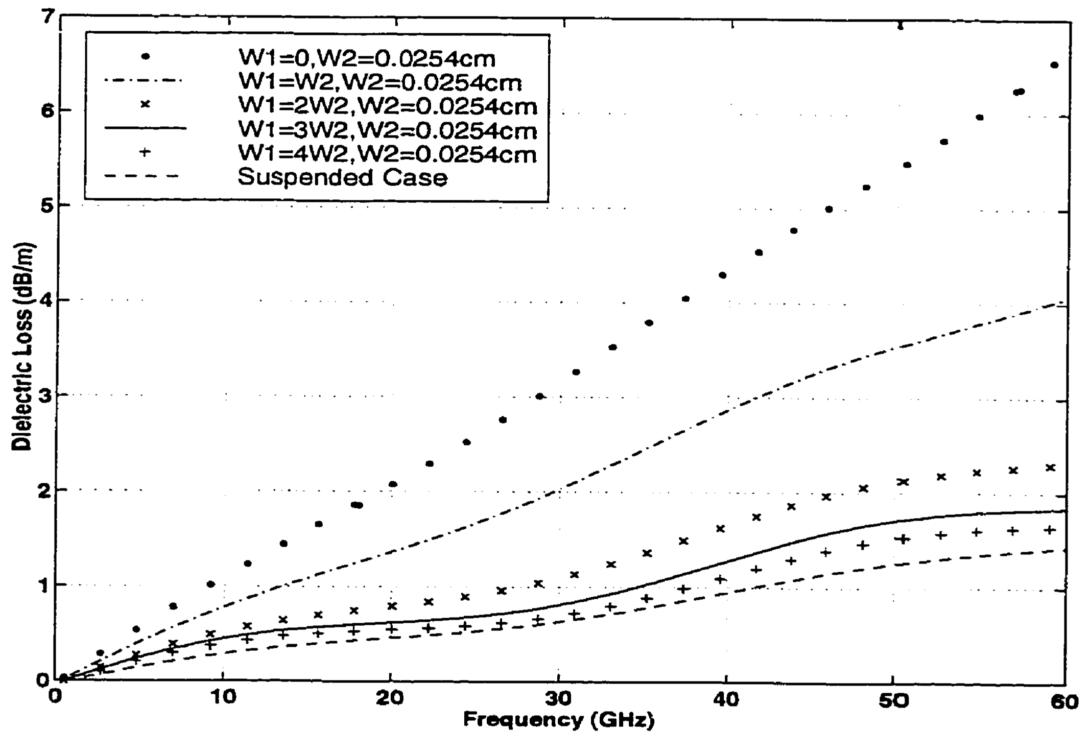

Fig. 3.3.3 Dielectric Loss for Fig. 3.3.1 between Y =130 dy & 150 dy

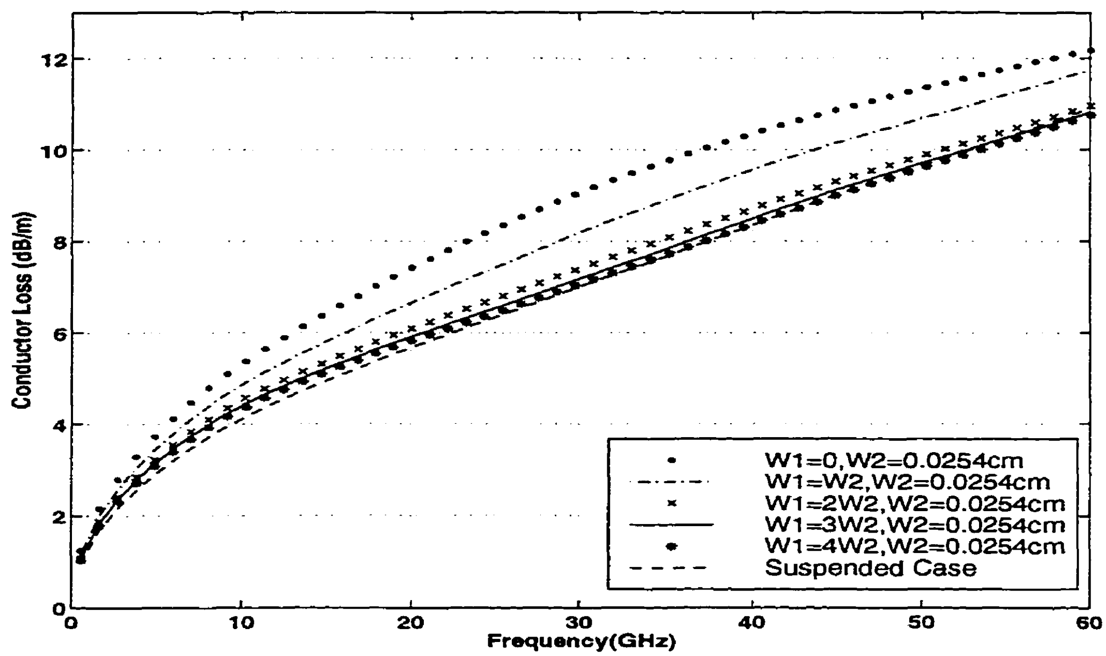

Fig. 3.3.4 Conductor Loss for Fig. 3.3.1 between Y =130 dy & 150 dy

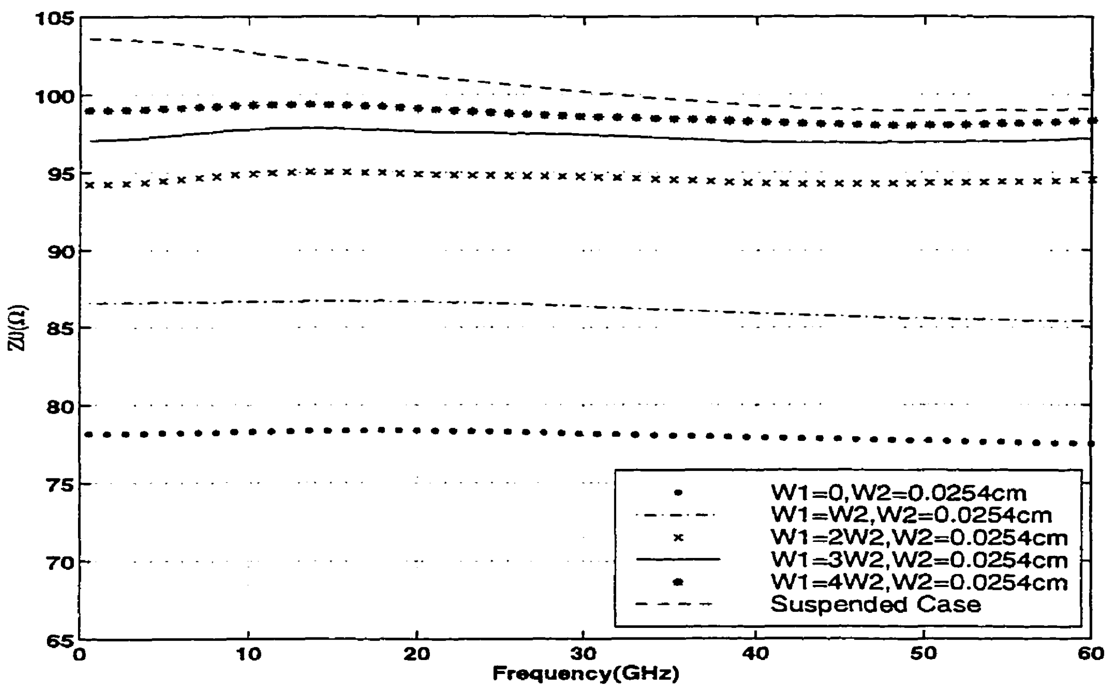

Fig. 3.3.5 Characteristic Impedance for Fig. 3.3.1 at Y = 30 dy

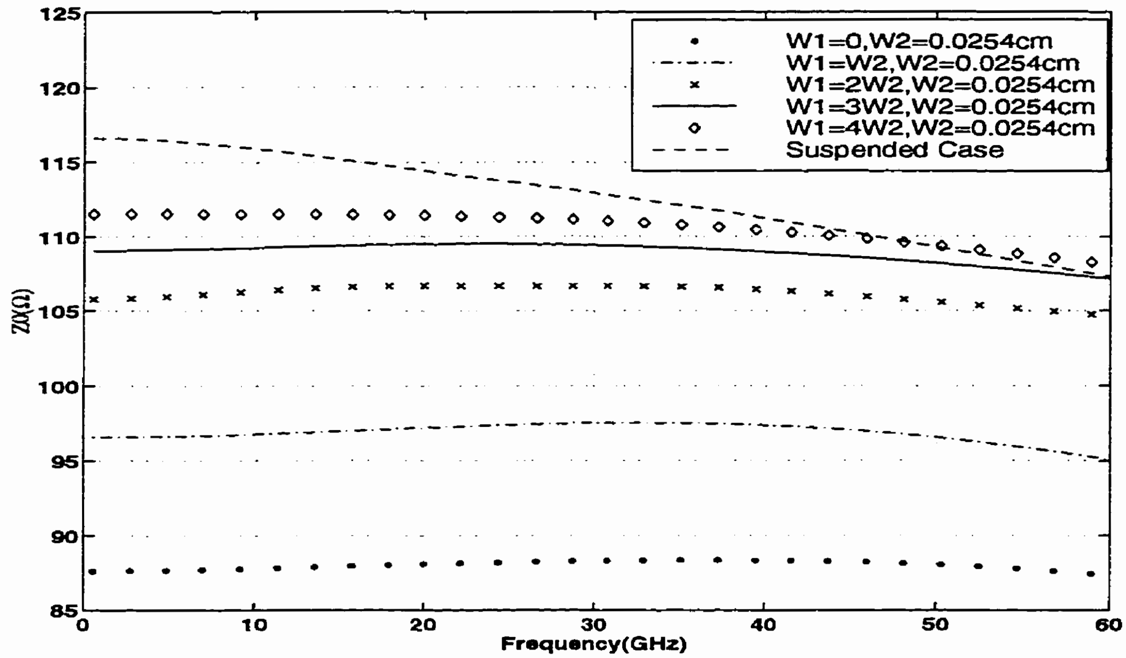

Fig. 3.3.6 Characteristic Impedance for Fig. 3.3.1 at Y = 50 dy

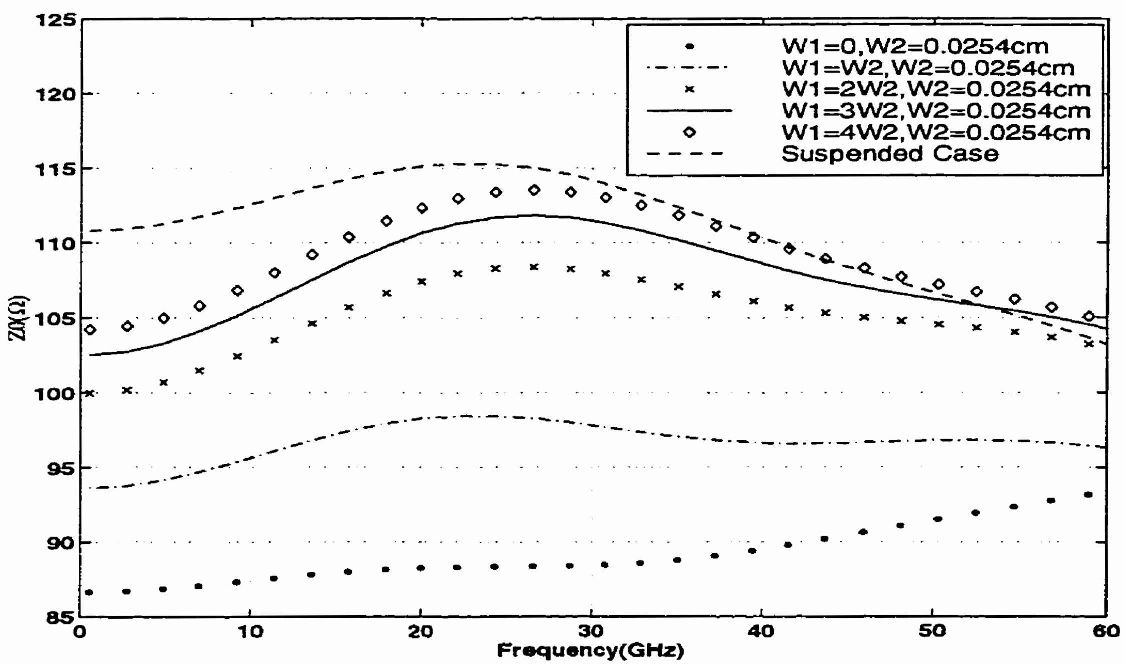

Fig. 3.3.7 Characteristic Impedance for Fig. 3.3.1 at Y = 150 dy

CHAPTER 4

Analysis of Low Loss Coplanar Waveguide Transmission Lines

In this chapter four types of novel low loss coplanar waveguide (CPW) transmission lines are analysed with FDTD. They are trenched or micromachined coplanar waveguide transmission lines with or without a bottom ground plane.

4.1 Analysis of Trenched Coplanar Waveguide Transmission Lines

Coplanar waveguides are used extensively in microwave & millimeter-wave components, circuits, MMIC & wireless communication systems. In this section, FDTD is used for the first time to analyse the resistive loss and other characteristics of trenched coplanar waveguide transmission lines. Two kinds of trenched coplanar waveguides, with and without a bottom ground plane, are studied in this section. Trench coplanar waveguide is formed by trenching two gaps, at both sides of the central transmission line, further inside the substrate. The width of trenches are the same as that of the gaps. The characteristics of a trenched coplanar waveguide transmission line vary as its trench's depth varies.

4.1.1 Trenched Coplanar Waveguide Transmission Lines without a Bottom Ground Plane

The geometry structure of trenched coplanar waveguide transmission lines without a bottom ground plane is shown in Fig. 4.1.1. A central transmission line is placed between two coplanar ground planes. The width of central coplanar waveguide transmission line is $W_2 = 0.0254$ cm. The gap width W_1, the same as the trench width, is equal to the half of the transmission line width W_2, $W_1 = 0.5 * W_2 = 0.0127$ cm. The trench depth is a variable. The substrate relative permittivity is $\varepsilon_r = 2.2$. Six first Mur ABCs are used to absorb the propagation waves in six directions. Initially, all fields are set to zero. At t = 0, two gaussian sources are excited simultaneously between the central transmission line and two coplanar ground planes at the surface of the substrate in the front cross section plane shown in Fig. 4.1.1. Its effective relative permittivity, dielectric loss, conductor loss and characteristic impedance are shown in Fig. 4.1.2-5.

Fig. 4.1.2 shows that effective relative permittivity decreases as the trench depth increases at all frequencies from 0 to 110 GHz. In Fig. 4.1.3 dielectric loss reduces greatly at the end of high frequency with the increase of the trench depth. For a coplanar waveguide without any trench (h = 0), the dielectric loss is 5.5 dB/m at 60 GHz and 10.5 dB/m at 110 GHz respectively. Moreover, with trench depth 0.0381 cm, the dielectric loss is 2.1 dB/m at 60 GHz and 4.1 dB/m at 110 GHz respectively. So the trench depth effects the dielectric loss greatly. In addition, Fig. 4.1.5 indicates the characteristic impedances decrease with the increase of frequency at a given trench depth. This agrees with the

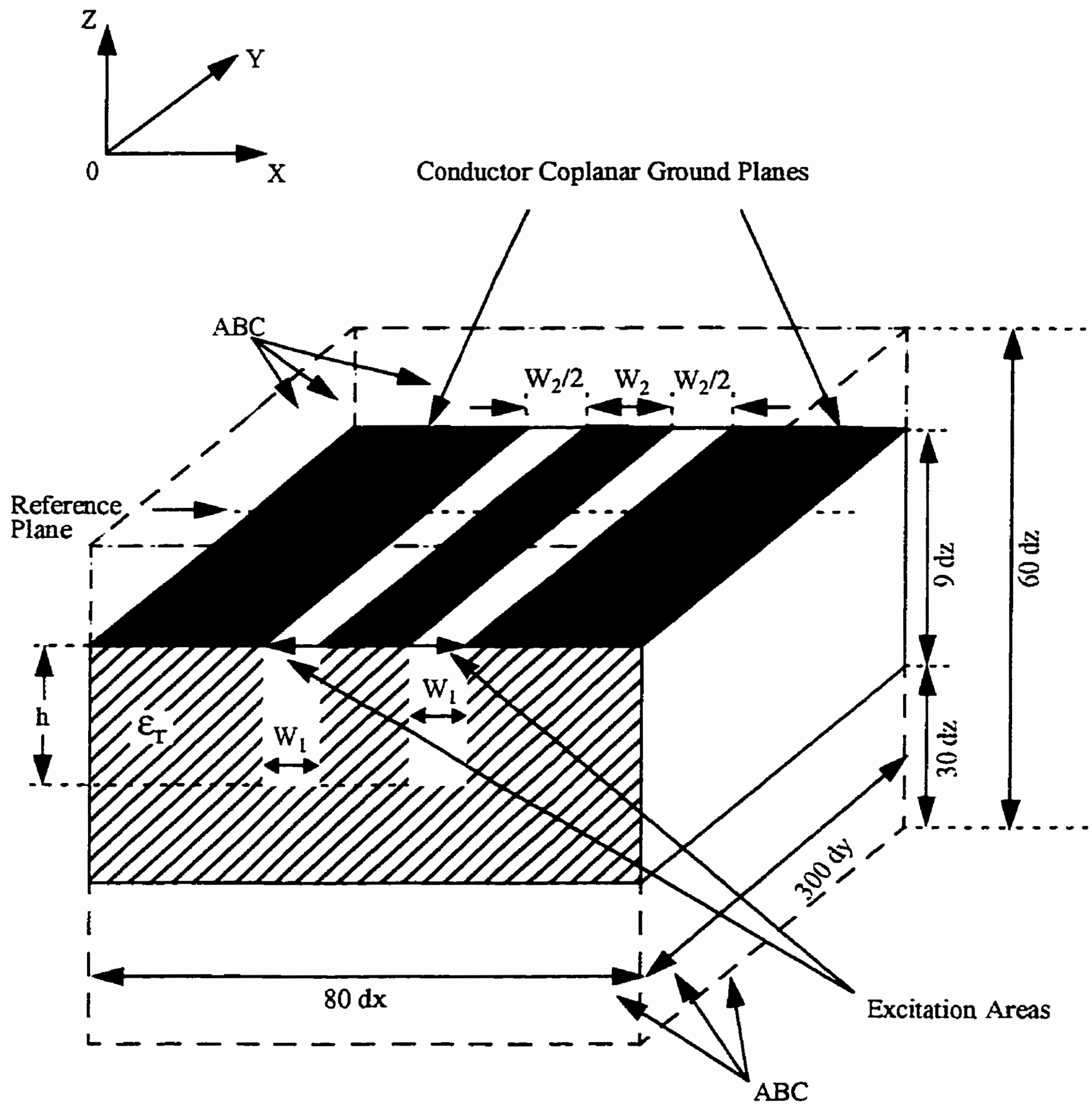

$W_1 = 0.0127$ cm $W_2 = 0.0254$ cm $\varepsilon_r = 2.2$ $dx = dy = dz = 0.004233$ cm

Fig. 4.1.1 Geometry Structure of Trenched Coplanar Waveguide Transmission Lines without a Bottom Ground Plane

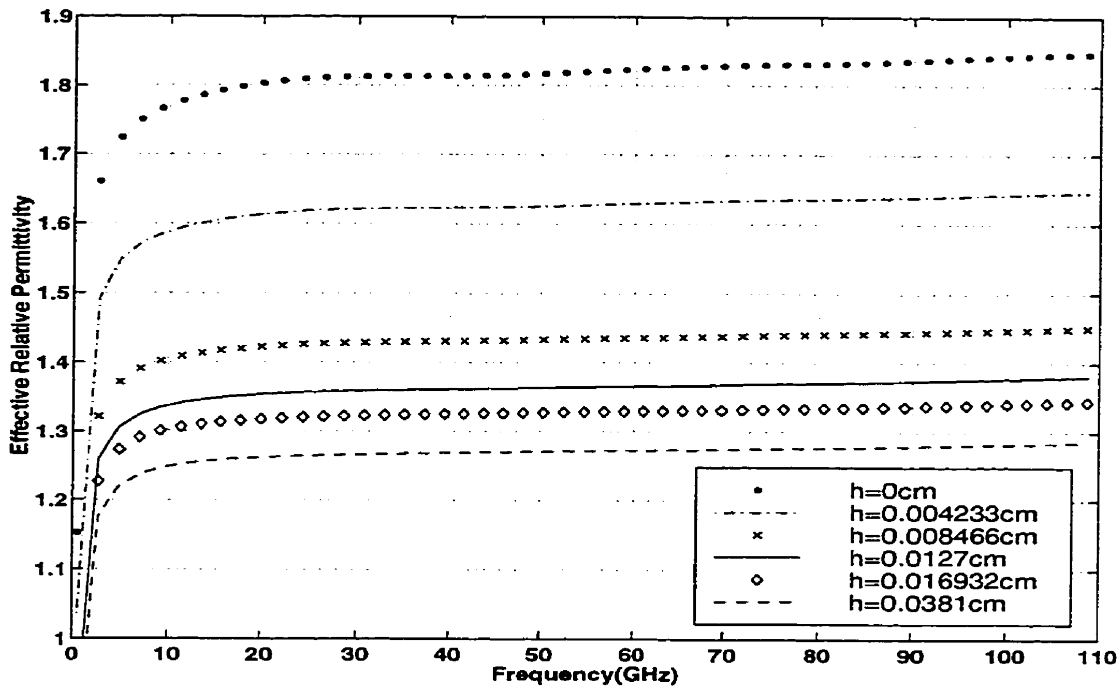

Fig. 4.1.2 Effective Relative Permittivity for Fig. 4.1.1 between Y =130 dy & 150 dy

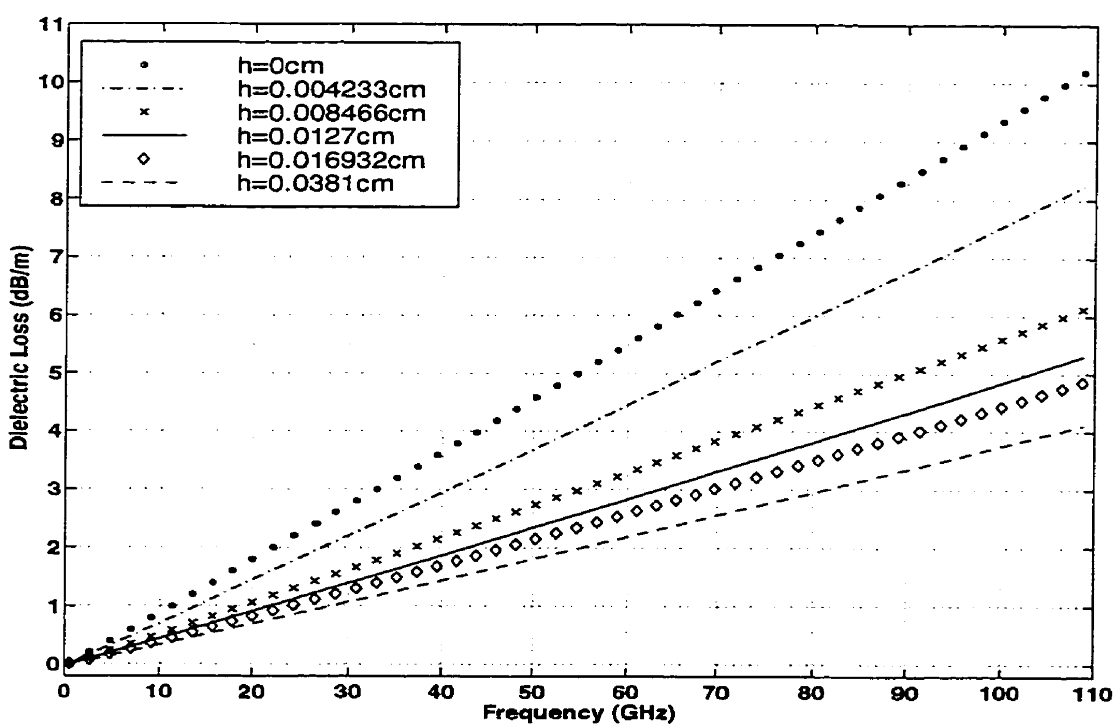

Fig. 4.1.3 Dielectric Loss for Fig. 4.1.1 between Y = 130dy & 150dy

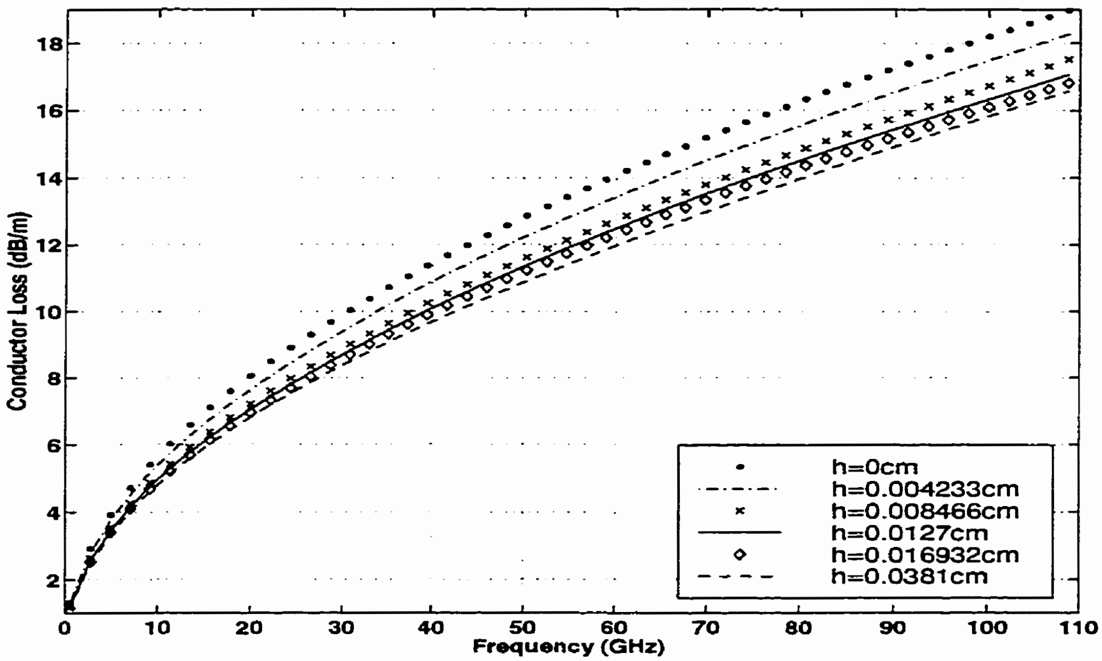

Fig. 4.1.4 Conductor Loss for Fig. 4.1.1 between Y = 130 dy & 150 dy

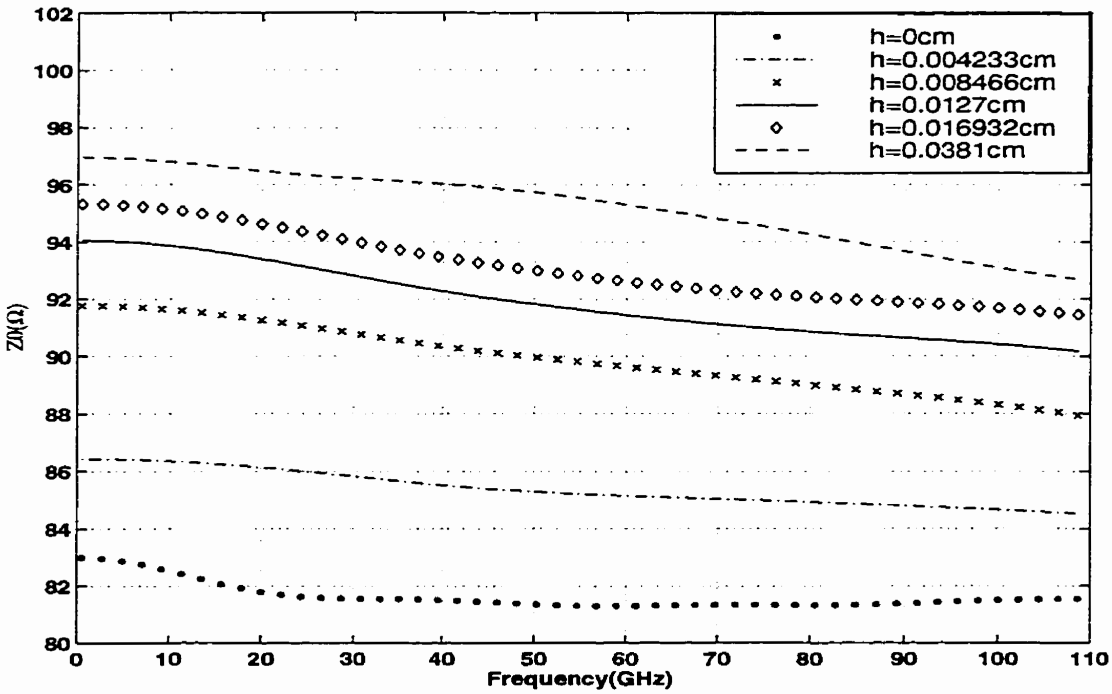

Fig. 4.1.5 Characteristic Impedance for Fig. 4.1.1 at Y = 150 dy

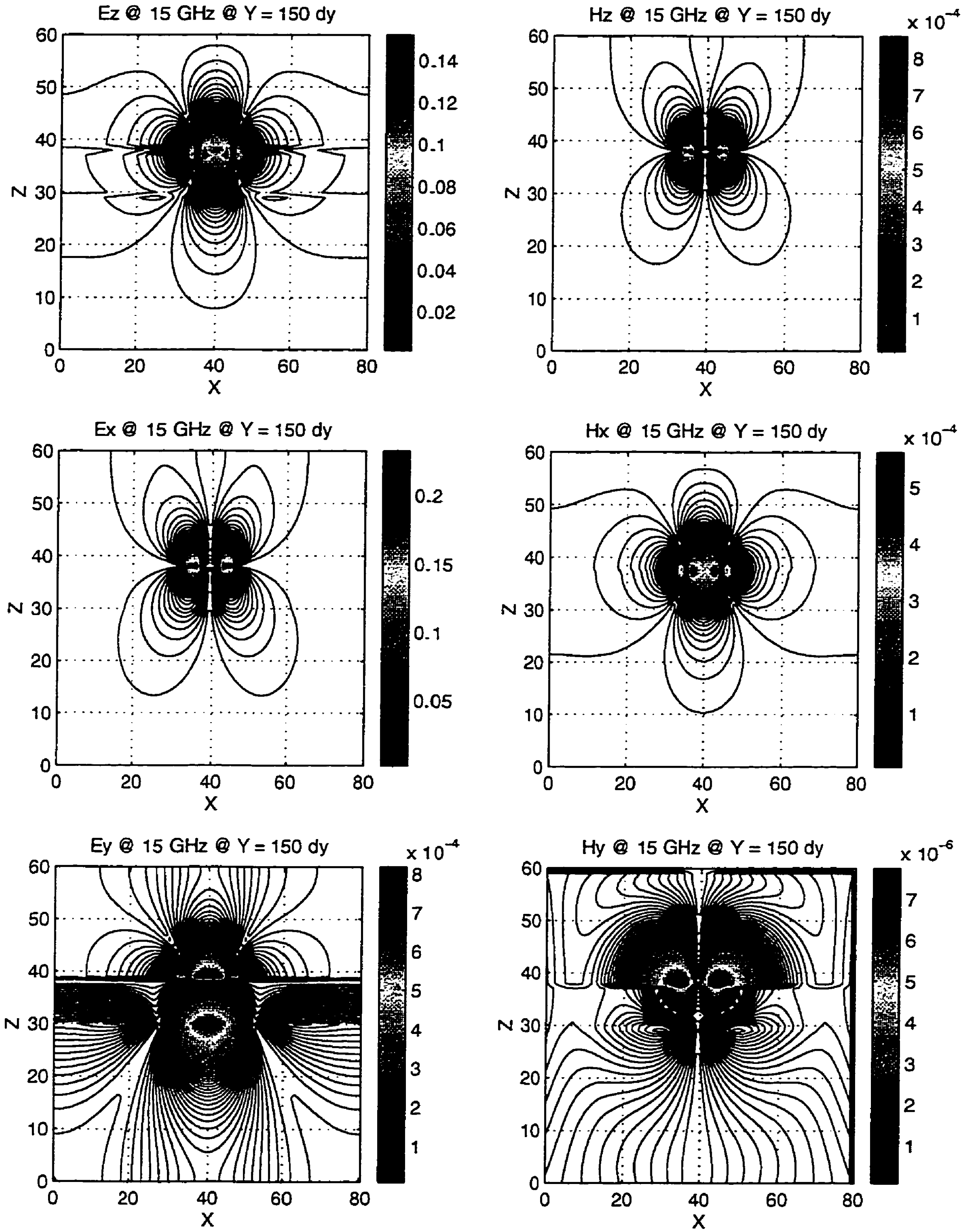

Fig. 4.1.6 Electric & Magnetic Fields Distributions at 15 GHz at Y=150 dy in X-Z Plane for Fig. 4.1.1 with h = 0 cm, Units: E: V/m, H: A/m

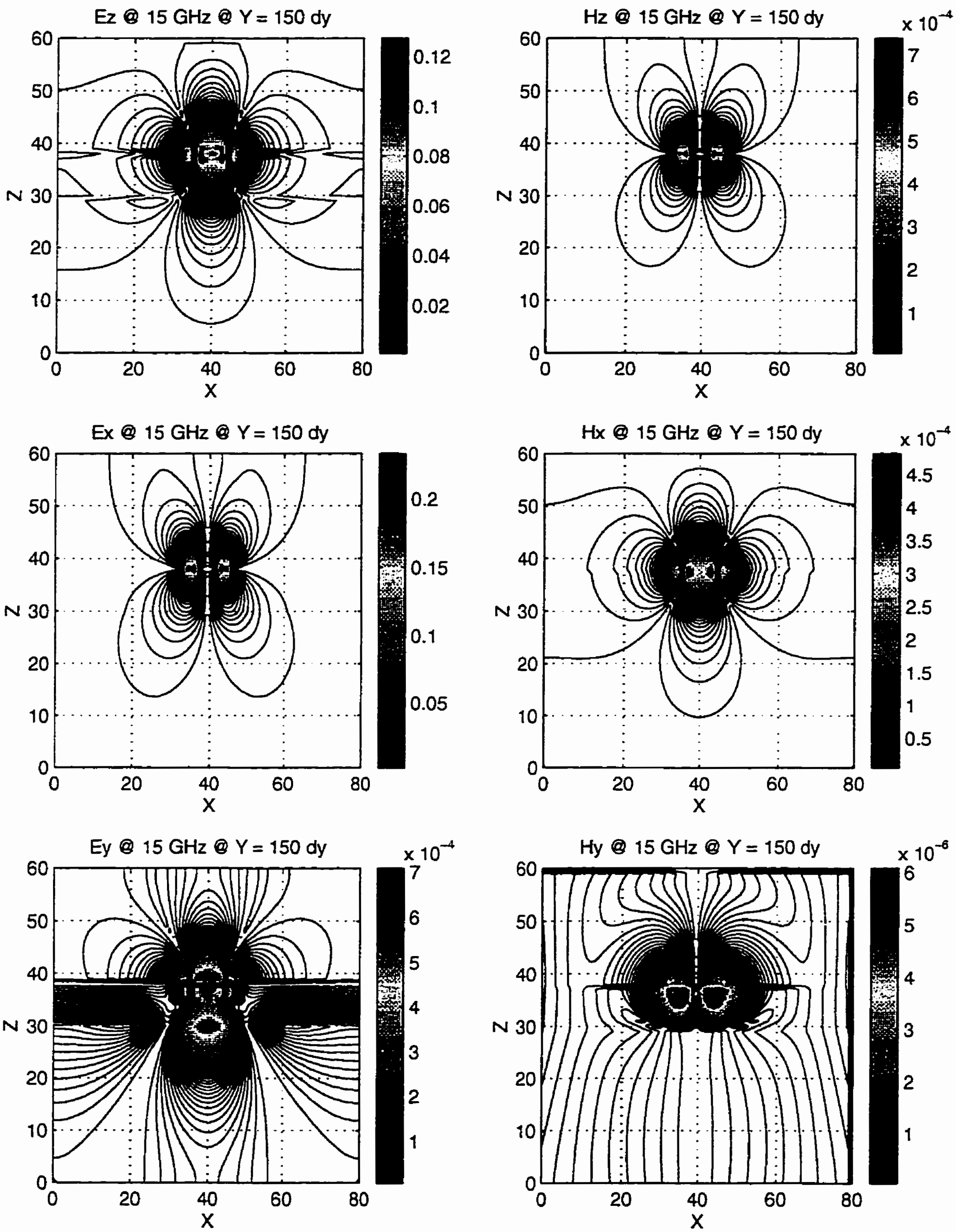

Fig. 4.1.7 Electric & Magnetic Fields Distributions at 15 GHz at Y=150 dy in X-Z Plane for Fig. 4.1.1 with h = 0.016932 cm, Units: E: V/m, H: A/m

conclusion of S. Yang [40]. The characteristic impedance changes little at different locations along Y axis [44]. Therefore, only the characteristic impedance at Y = 150 dy is plotted. The electric and magnetic field distributions at 15 GHz at Y =150 dy in X-Z plane with h = 0 cm, 0.016932 cm are shown in Fig. 4.1.6-7 respectively. Both Fig. 4.1.6-7 show that most of E_x & E_z focuses on the fringes of the conductors due to the singularities. Most of the propagation energy E_y in Fig. 4.1.6 without a trench is focused just above the central conductor transmission line and at the interface between the substrate and the air under the central transmission line. In Fig. 4.1.7 some E_y exists inside the trenches so that the energy focusing at the horizontal interface between the substrate and the air under the central transmission line decreases. Consequently, the effective permittivity and the dielectric loss is reduced.

4.1.2 Trenched Coplanar Transmission Lines with a Bottom Ground Plane

In this subsection trenched coplanar waveguide transmission lines with a bottom ground plane are studied to compare their results with their counterparts without a bottom ground plane. The geometry structure of a trenched coplanar waveguide transmission line with bottom ground plane is shown in Fig. 4.1.8. Three gaussian pulses are excited simultaneously. One of them, is excited between the central conductor transmission line and the bottom ground plane in ABCD area in the front cross-section plane shown in Fig. 4.1.8. The other two are excited between the central conductor transmission line and the coplanar ground plane at the surface of substrate in the front cross-section plane. Due to the three ground planes, the amplitude and phase of three pulses have to be selected properly so that the voltages and phases between the central transmission line and three ground planes are the same in this case. For the practical use, one has to be careful to choose excitation pulses. In addition, five first order Mur ABCs are used to absorb propagation waves in five directions because there is a bottom ground plane at z = 0. The corresponding effective relative permittivity, dielectric loss, conductor loss and characteristic impedance are shown in Fig. 4.1.9-12. The results are quite similar to the counterparts without a bottom ground plane described in the previous subsection.

The comparison between Fig. 4.1.2 and Fig. 4.1.9 shows that the trenched coplanar waveguide transmission lines with a bottom ground plane have higher effective relative permittivity than those without bottom ground planes at a given trench depth at all frequencies. Fig. 4.1.10 shows the dielectric loss at 60 GHz with a trench depth h = 0 cm, 0.0381 cm are 6 dB/m, 3 dB/m respectively which are 0.5 dB/m, 0.9 dB/m higher than the counterparts without a bottom ground plane in Fig. 4.1.3. In Fig. 4.1.12, the characteristic impedance decreases with the increase of frequencies at a given trench depth. The characteristic impedance increases along with the increase of a trench depth. Besides, the comparison between Fig. 4.1.5 and Fig. 4.1.12 indicates that the trenched coplanar waveguide transmission lines with a bottom ground plane have lower characteristic impedance than the corresponding ones without a bottom ground plane at all frequencies for all the given trench depths.

The electric and magnetic fields distributions at 15 GHz at Y = 150 dy in X-Z plane with h = 0 cm, 0.016932 cm are shown in Fig. 4.1.13-14 respectively which indicate that most of E_x & E_z focuses on the fringes of the conductors due to the singularities. In Fig. 4.1.13, there is a small E_z field between the upper conductor plane and the bottom ground plane. While in Fig. 4.1.14, some energy of E_y exists in the trenches which are filled with the air. As a result, the effective permittivity and the dielectric loss decrease.

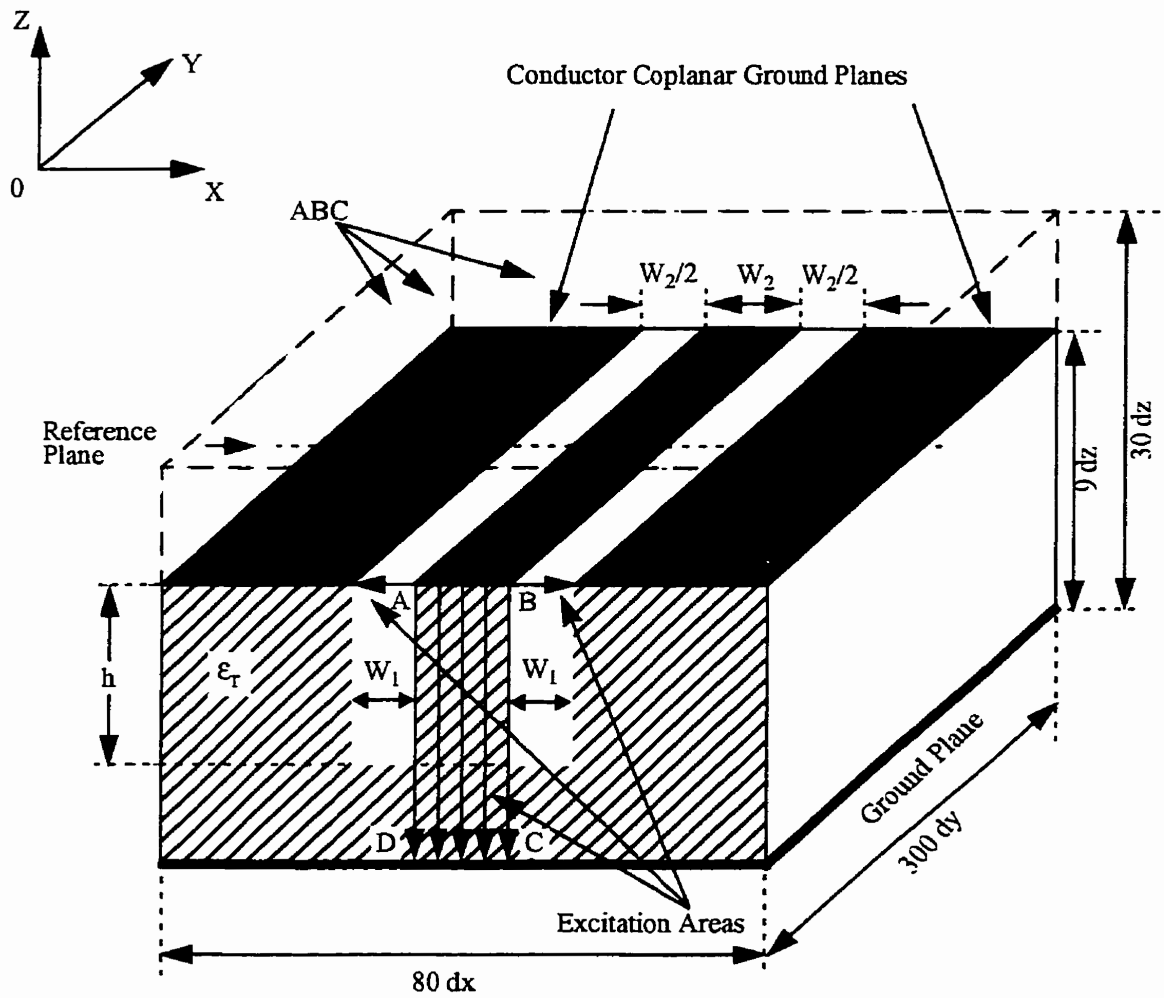

$W_1 = 0.0127$ cm $W_2 = 0.0254$ cm $\varepsilon_r = 2.2$ $dx = dy = dz = 0.004223$ cm

Fig. 4.1.8 Geometry Structure of Trenched Coplanar Waveguide Transmission Line with a Bottom Ground Plane

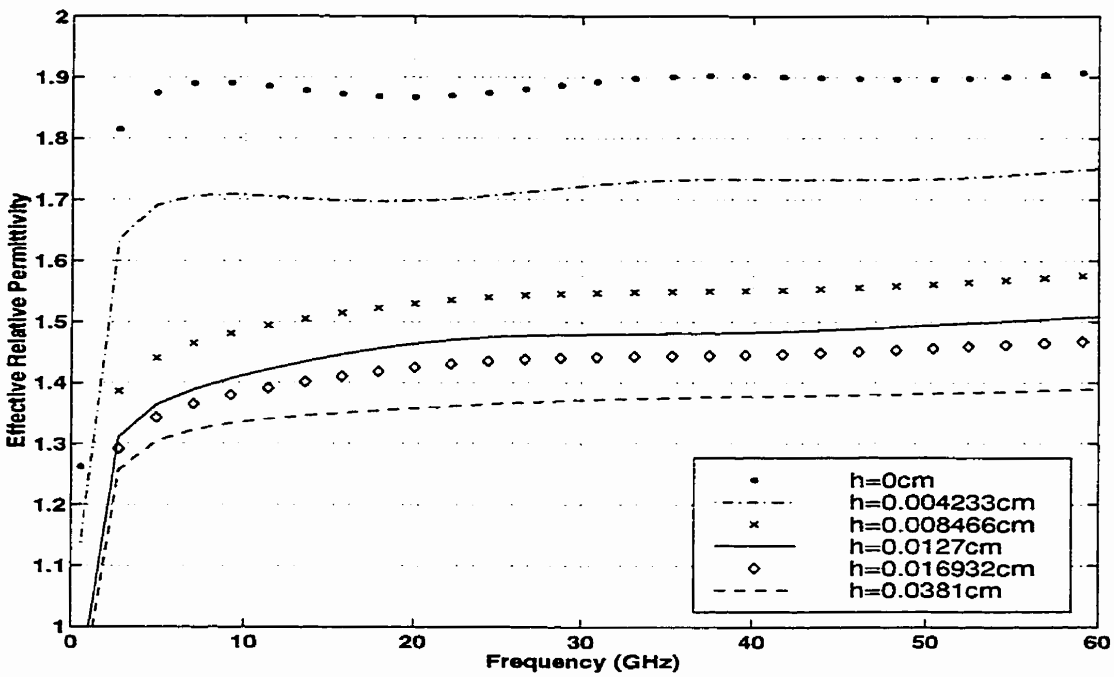

Fig. 4.1.9 Effective Relative Permittivity for Fig. 4.1.8 between Y = 130 dy & 150 dy

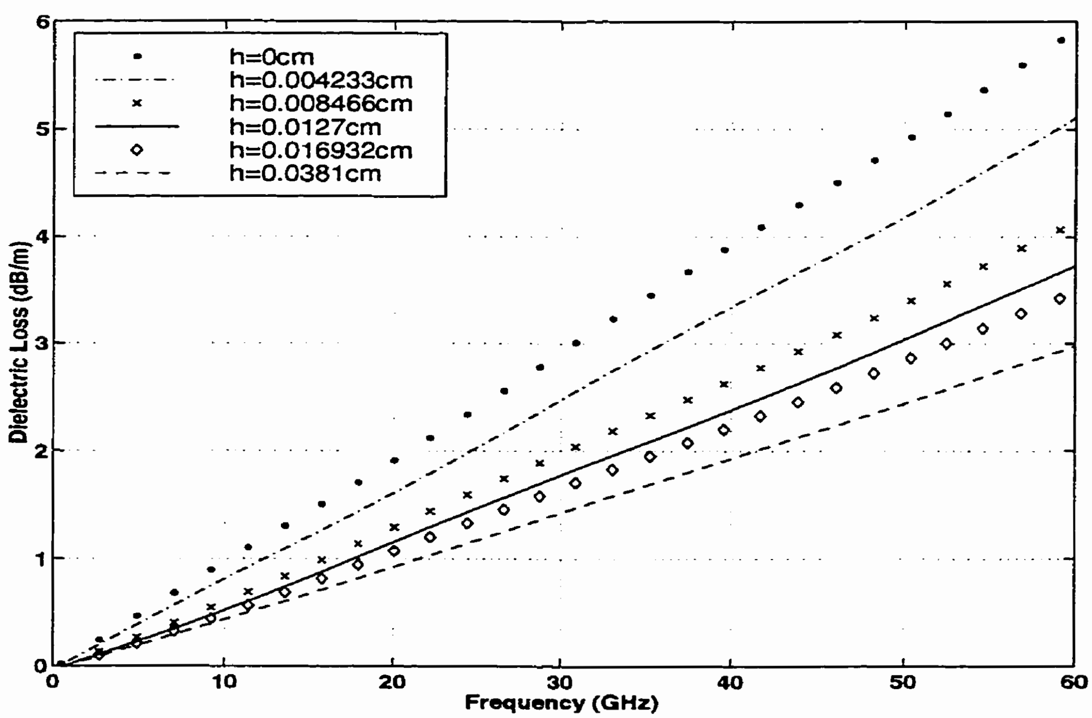

Fig. 4.1.10 Dielectric Loss for Fig. 4.1.8 between Y = 130 dy & 150 dy

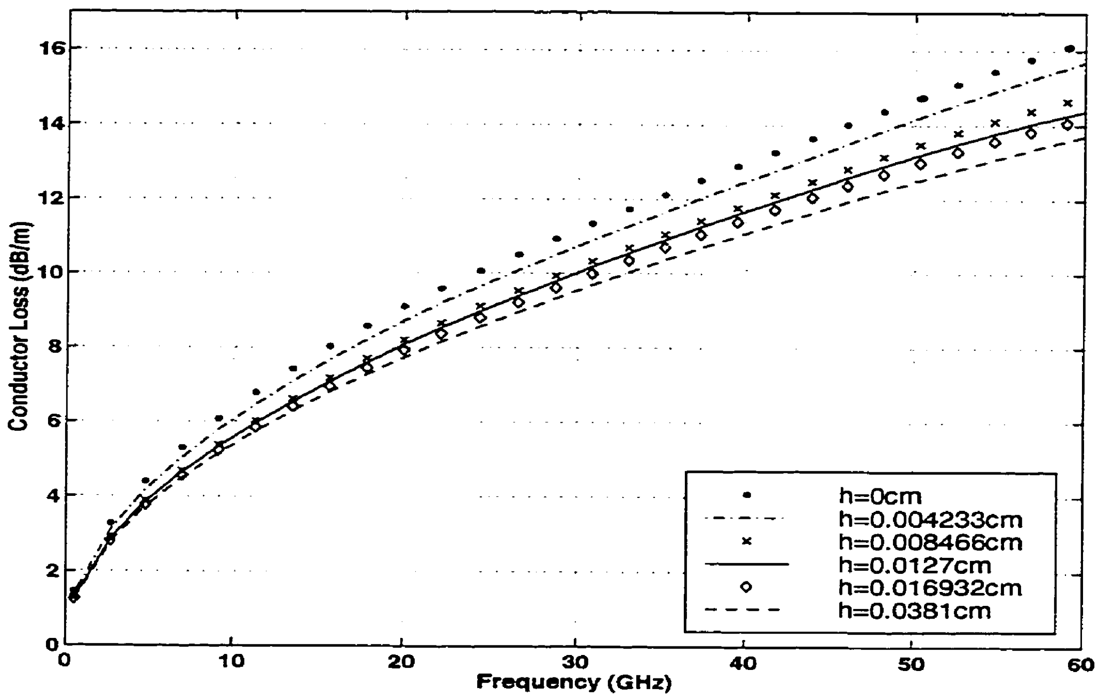

Fig. 4.1.11 Conductor Loss for Fig. 4.1.8 between Y = 130 dy & 150 dy

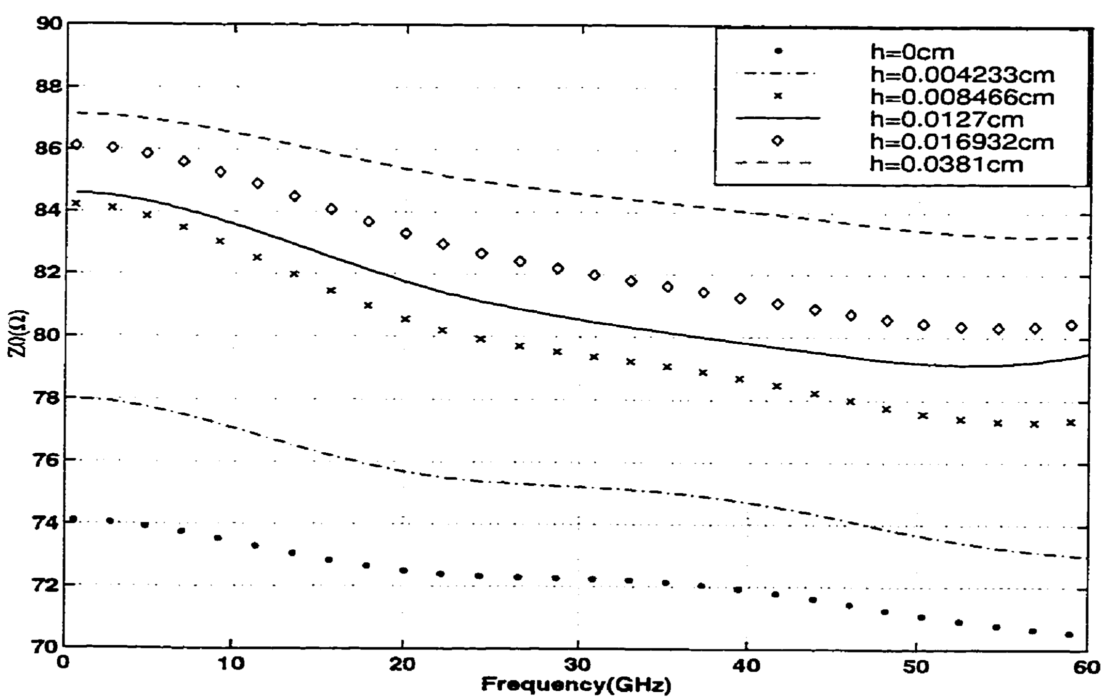

Fig.4.1.12 Characteristic Impedance for Fig. 4.1.8 at Y = 150 dy

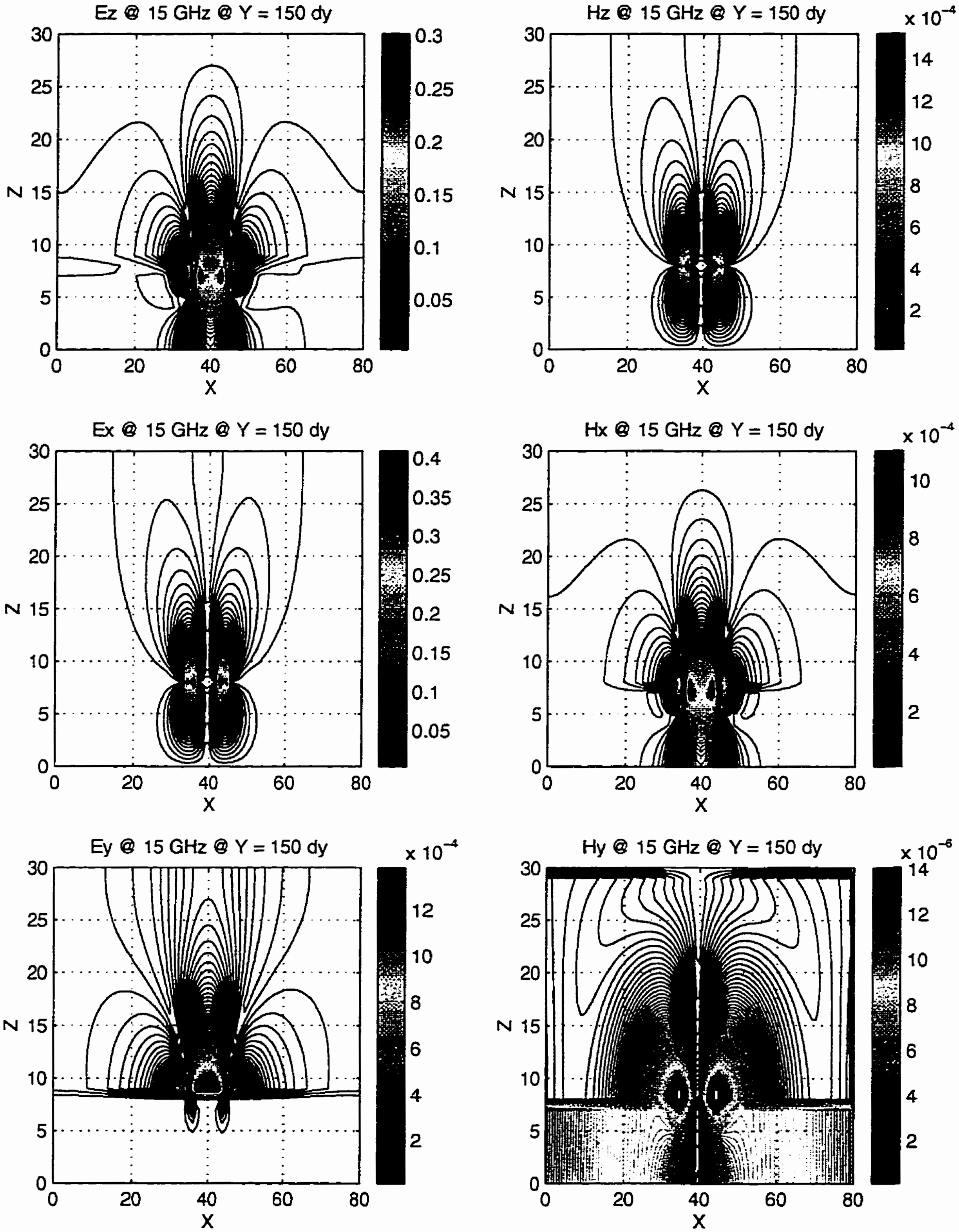

Fig. 4.1.13 Electric & Magnetic Fields Distributions at 15 GHz at Y=150 dy in X-Z Plane for Fig. 4.1.8 with h = 0 cm, Units: E: V/m, H: A/m

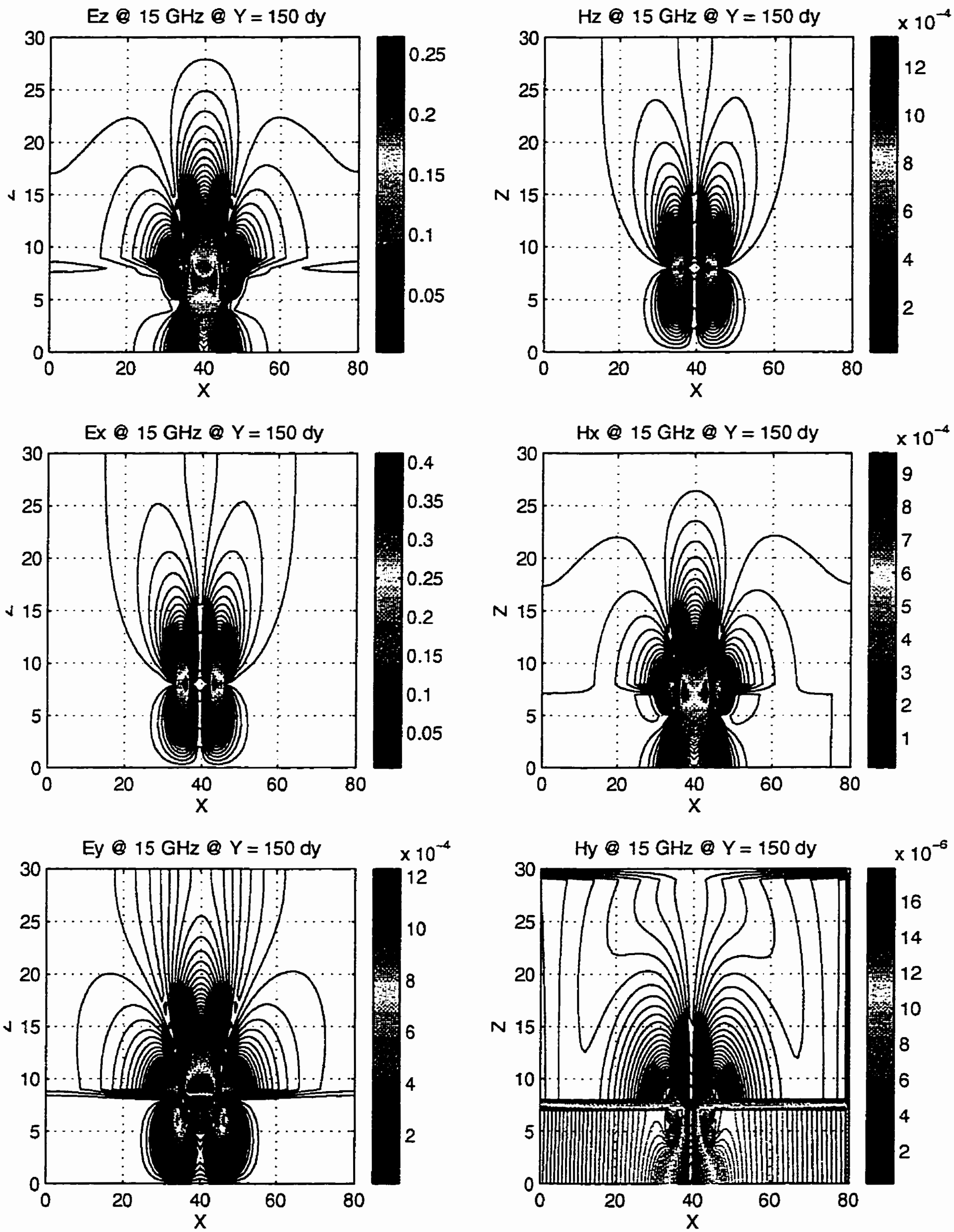

Fig. 4.1.14 Electric & Magnetic Fields Distributions at 15 GHz at Y=150 dy in X-Z Plane for Fig. 4.1.8 with h = 0.016932 cm, Units: E: V/m, H: A/m

4.2 Analysis of Micromachined Coplanar Waveguide Transmission Lines

In this section, dielectric loss, conductor loss and other characteristics of micromachined coplanar waveguide transmission lines with grooves extending underneath the central transmission line and coplanar ground planes will be studied and compared to those of the trenched coplanar waveguide transmission lines and micromachined microstrip transmission lines analysed previously in this thesis.

4.2.1 Micromachined Coplanar Waveguide Transmission Lines with a Bottom Ground Plane

The geometry structure of micromachined coplanar waveguide transmission lines with a bottom ground plane is shown in Fig. 4.2.1. The top and bottom conductor ground planes and the metal central transmission line are assumed to be infinitely thin. Three Gaussian pulses are excited simultaneously between the central conductor transmission lines and 3 ground planes shown in Fig. 4.2.1. Two grooves are micromachined symmetrically underneath the upper conductor planes and the gaps. Their depths are the same as the thickness of the substrate. The substrate is micromachined gradually towards underneath the central transmission line and the coplanar conductor ground planes. The cross sections of all the cases studied in this subsection for micromachined coplanar waveguide transmission lines with a bottom ground plane are shown in Fig. 4.2.2. The effective relative permittivity, dielectric loss, conductor loss and characteristic impedance are shown in Fig. 4.2.3-6. Fig. 4.2.3 indicates that the effective relative permittivity decreases from 1.85 to 1 with the increase of groove width up to the suspended case, in which the substrate is replaced with the air completely. Consequently, the dielectric loss can reach as low as zero at the suspended case in Fig. 4.2.4, just as we expected. It is also noticed that for the case 1 in Fig. 4.2.2 with $W_1 = 0.016932$ cm, although the groove has a little extension into the substrate underneath the central transmission line, the dielectric loss has a great reduction from 6 dB/m to 2 dB/m at 60 GHz shown in Fig. 4.2.4. In the case 3 in Fig. 4.2.2 with $W_1 = 0.0254$ cm, when the substrate underneath both the central transmission line and the gaps are grooved entirely, the dielectric loss reaches as low as 0.3 dB/m at 60 GHz. In the case 4 in Fig. 4.2.2 with $W_1 = 0.033864$ cm, while the groove extends into the substrate underneath the coplanar ground planes, the dielectric loss in Fig. 4.2.4 is nearby 0 dB/m. The reason for this is that its behavior in this case is just like a TEM wave propagating within a metal rectangular waveguide with two slots at the top. In addition, the conductor loss decreases from 16.2 dB/m to 11.7 dB/m in Fig. 4.2.5. Fig. 4.2.6 illustrates that characteristic impedance decreases with the increase of frequency at a given groove width from 0 to 60 GHz. It increases with the increase of groove width at a given frequency point for all the frequencies of interest.

The six field component distributions for the case 2 and the case 4 at 15 GHz are shown in Fig. 4.2.7-8, respectively. They indicate that most of E_y focuses at the vertical interface between the groove and the substrate. Except for the part of E_y just above the central conductor transmission line and on the fringes of the coplanar ground planes, almost half of the other E_y energy concentrates inside the groove and another half exists inside the substrate. Most energy of E_x and E_z concentrates on the fringes of the conductor planes which are singularities.

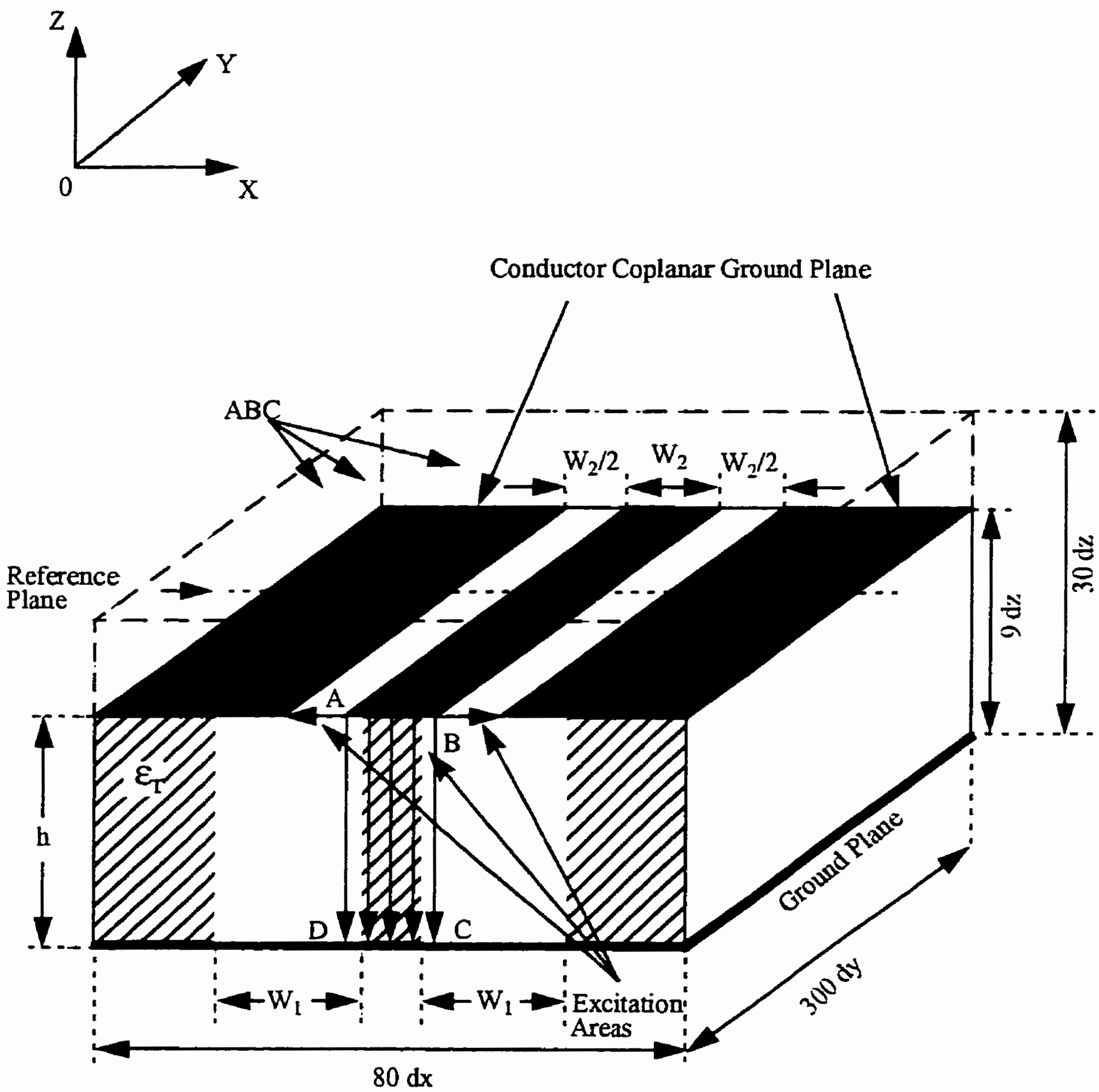

$h = 0.0381$ cm $W_2 = 0.0254$ cm $\varepsilon_r = 2.2$ $dx = dy = dz = 0.004233$ cm

Fig. 4.2.1 Geometry Structure of Micromachined Coplanar Waveguide Transmission Line with a Bottom Ground Plane

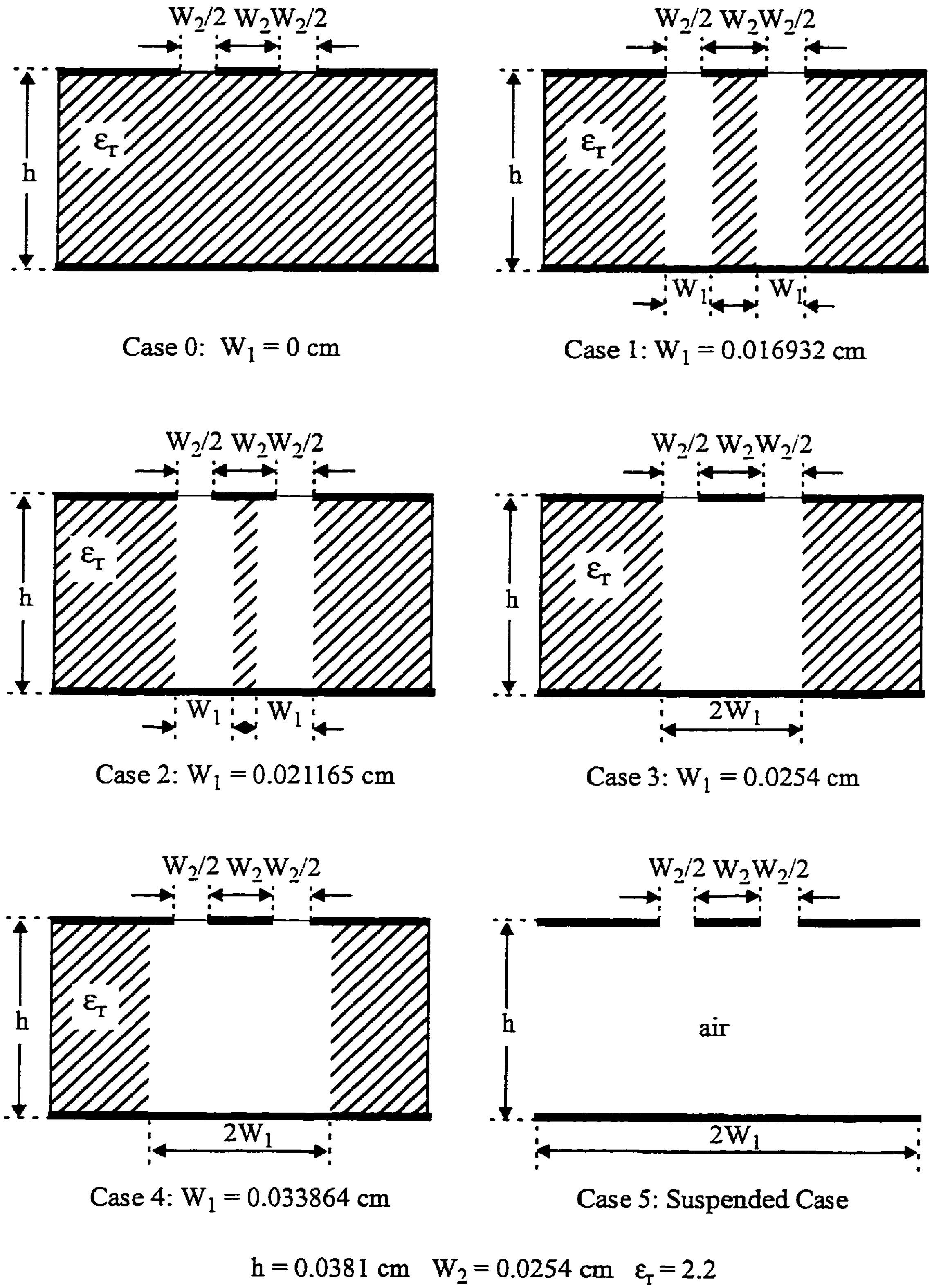

Fig. 4.2.2 Cross Sections for Fig. 4.2.1 for Calculations

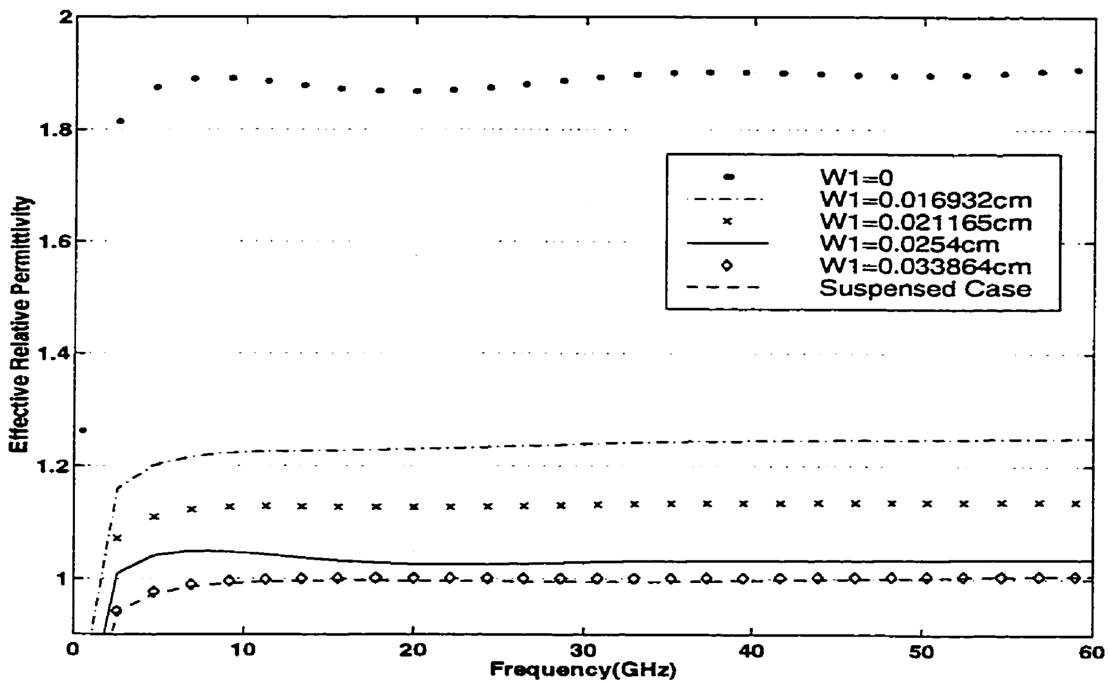

Fig.4.2.3 Effective Relative Permittivity for Fig. 4.2.1 between Y = 130 dy & 150 dy

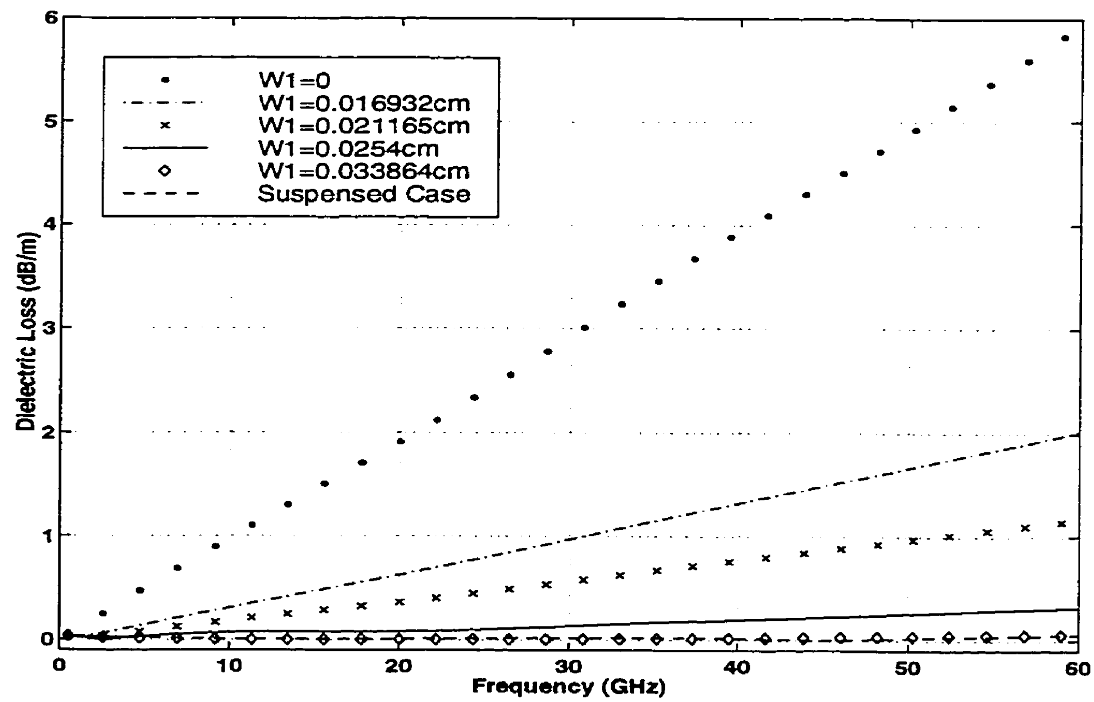

Fig. 4.2.4 Dielectric Loss for Fig. 4.2.1 between Y = 130 dy & 150 dy

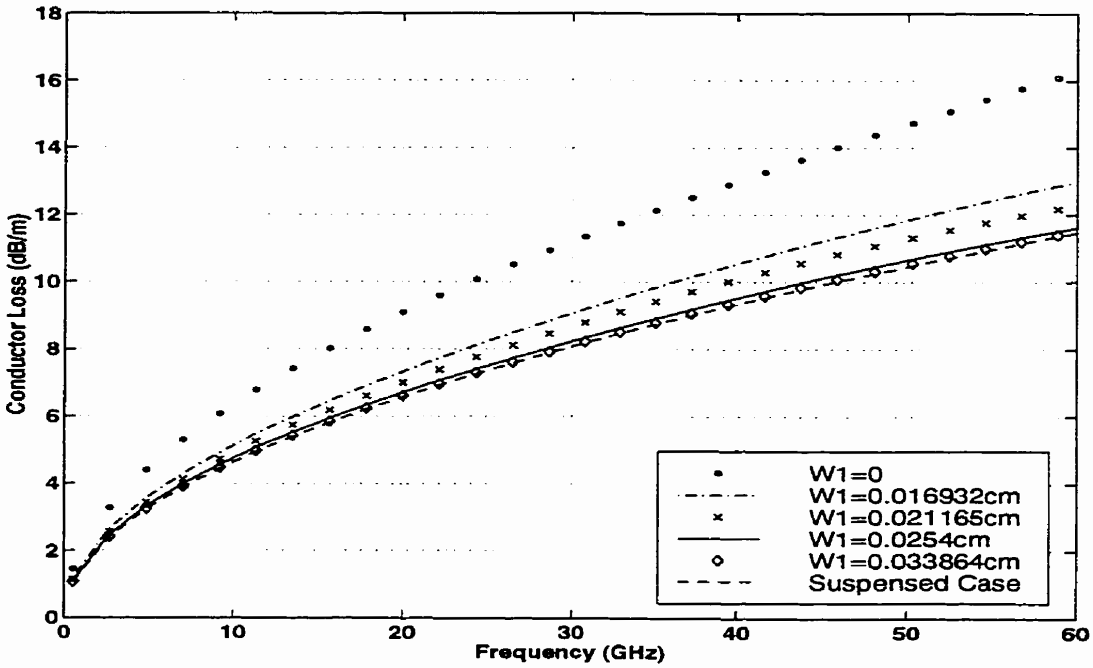

Fig. 4.2.5 Conductor Loss for Fig. 4.2.1 between Y = 130 dy & 150 dy

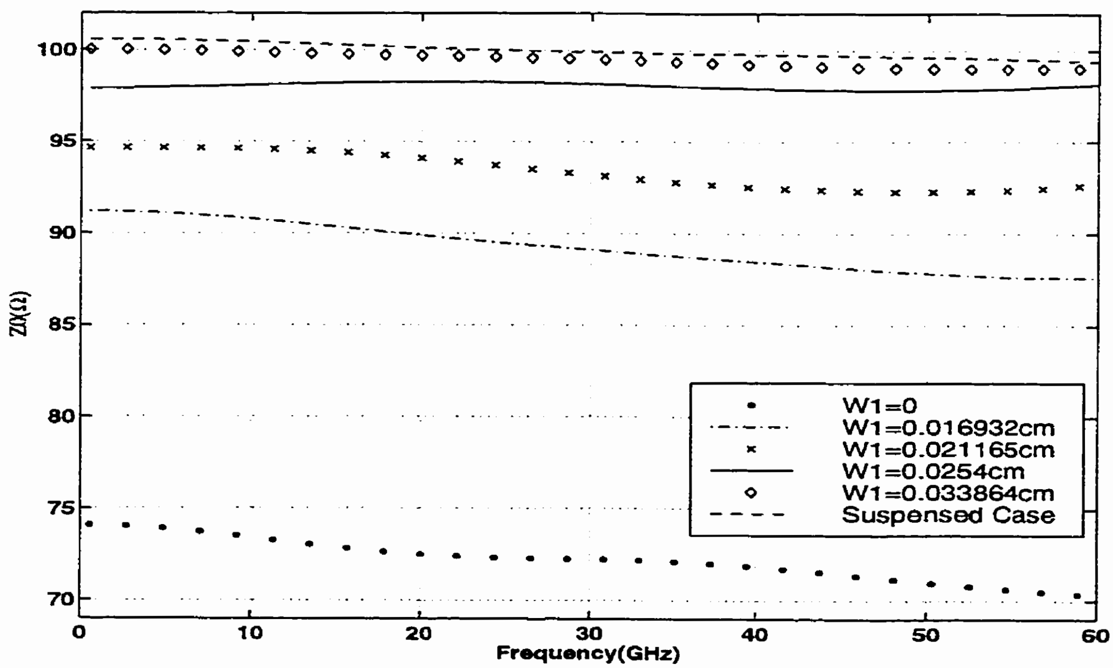

Fig. 4.2.6 Characteristic Impedance for Fig. 4.2.1 at Y = 150 dy

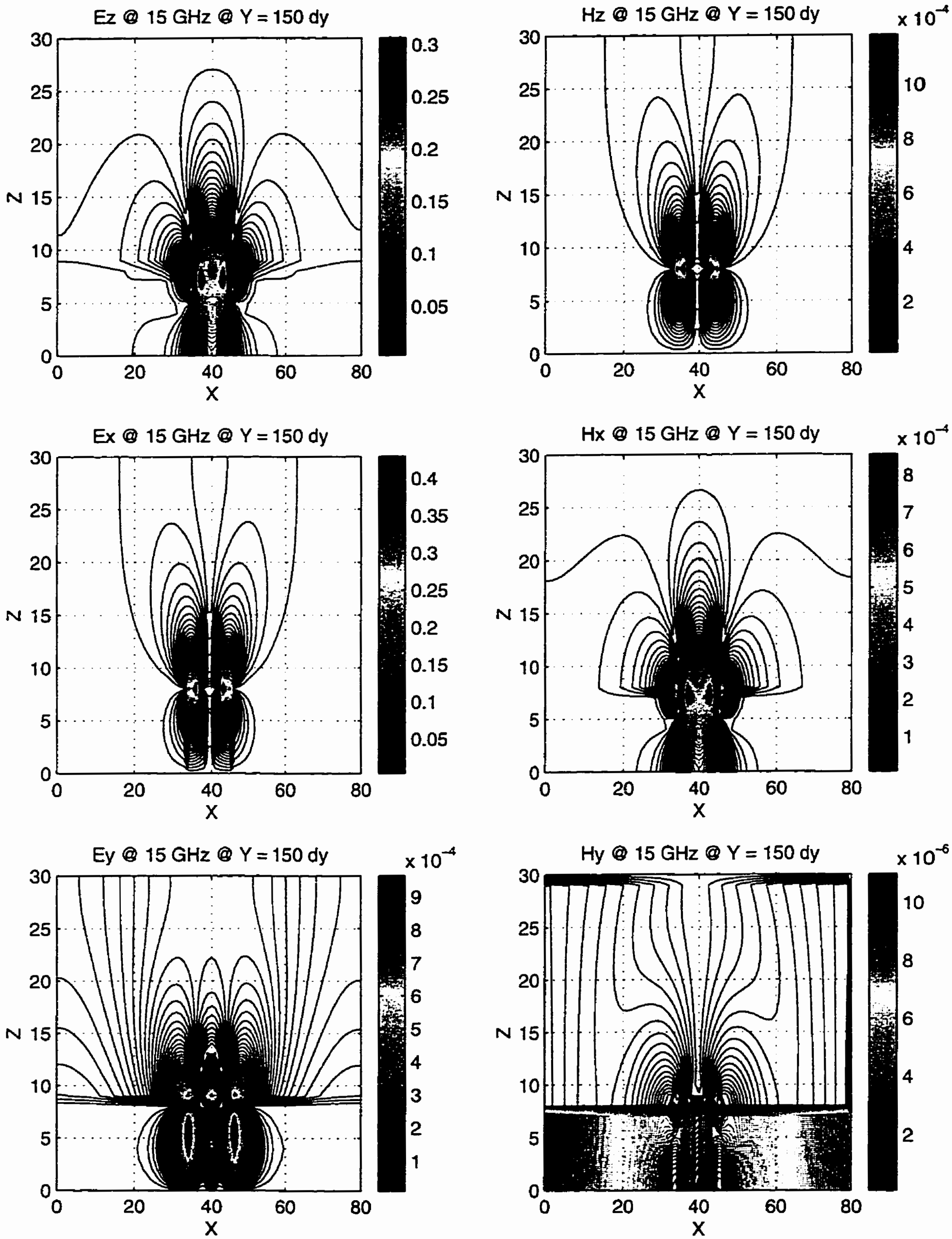

Fig. 4.2.7 Electric & Magnetic Fields Distributions at 15 GHz at Y=150 dy in X-Z Plane for Case 2 in Fig. 4.2.2, Units: E: V/m, H: A/m

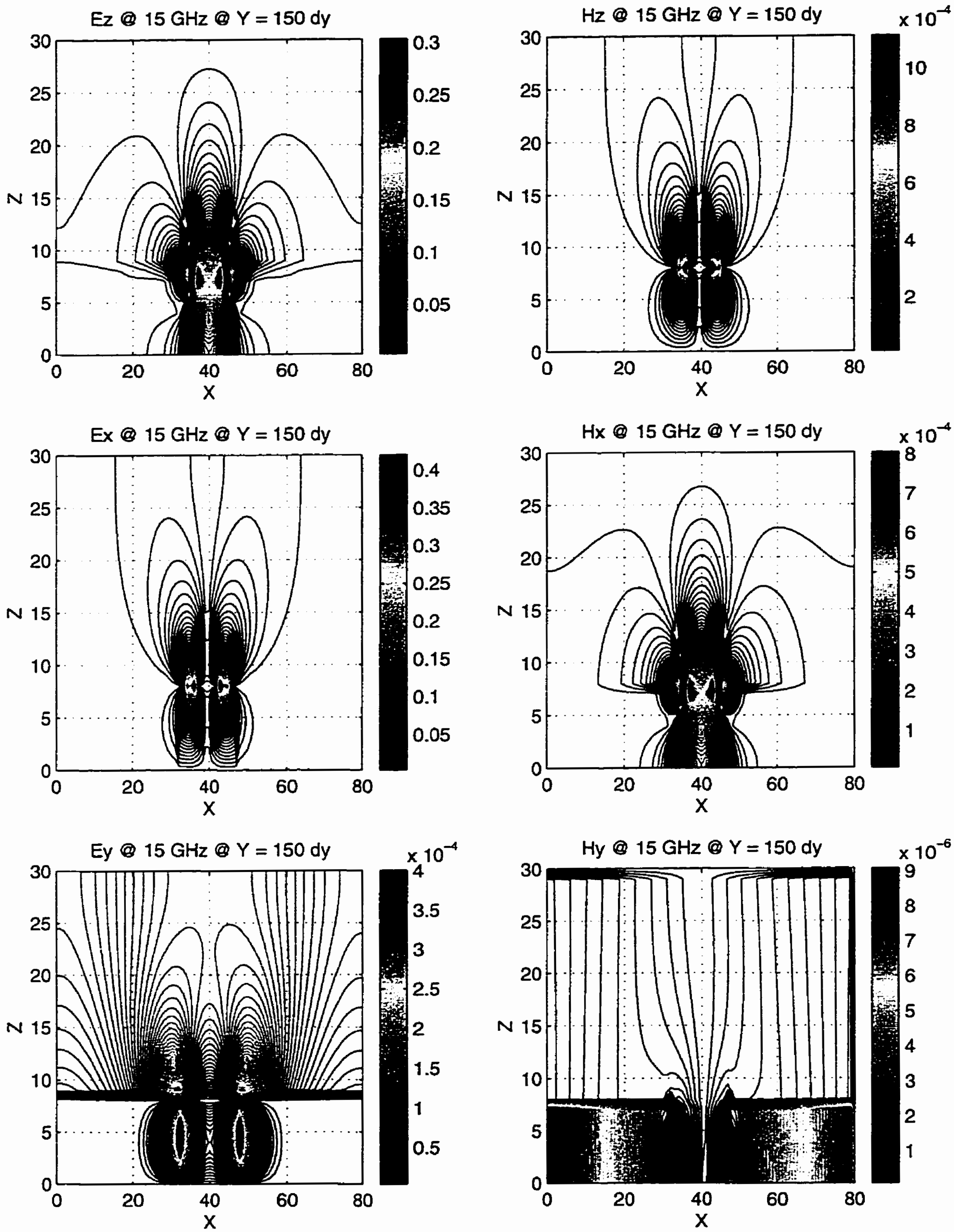

Fig. 4.2.8 Electric & Magnetic Fields Distributions at 15 GHz at Y=150 dy in X-Z Plane for Case 4 in Fig. 4.2.2, Units: E: V/m, H: A/m

4.2.2 Micromachined Coplanar Waveguide Transmission Lines without a Bottom Ground Plane

Micromachined coplanar waveguide transmission lines without a bottom ground plane in Fig. 4.2.9 are studied in this subsection. The geometry parameters are the same as those in the previous subsection 4.2.1 except without a bottom ground plane. Only two Gaussian pulses are excited in the front cross section plane at the top surface of the substrate between the central transmission line and two coplanar ground planes shown in Fig. 4.2.9. Six first order Mur ABCs are used to absorb propagation waves in six directions.

Six cases will be studied in this subsection. The cross sections of the geometry structures under the consideration are the same as those in Fig. 4.2.2 except without a bottom ground plane. The groove width is the variable. The case 1 with $W_1 = 0.016932$ cm in Fig. 4.2.10 has lower effective relative permittivity, $\varepsilon_{reff} = 1.18$ than that of the case with h = 0.0381 cm in Fig. 4.1.2, $\varepsilon_{reff} = 1.28$. It is reasonable because the former one has a wider groove width than the latter and consequently the former one has a lower effective permittivity. As a result, the dielectric loss in the case 1 with $W_1 = 0.016932$ cm in Fig. 4.2.11 is lower than that of the case h = 0.0381 cm in Fig. 4.1.3.

The conductor loss in Fig. 4.2.12 drops from 14 dB/m to 10.5 dB/m at 60 GHz from the conventional case $W_1 = 0$ to the suspended case respectively. It is also noticed that when the groove width equals to $2W_1 = 2 * 0.033864$ cm = 0.067728 cm, the conductor loss is as low as that of the suspended case in the Fig. 4.2.12. In Fig. 4.2.11, the dielectric loss of the case $W_1 = 0.033864$ cm approaches zero which is the result of the suspended case. Namely, the performance of the suspended case can be achieved by the non-suspended case which can be fabricated much easier than the suspended one.

Field components distributions are shown in Fig. 4.2.13-14 for the cases W_1 = 0.021165 cm and W_1 = 0.033864 cm respectively. Fig. 4.2.13 indicates that most of the propagation energy E_y concentrates at the vertical interface between the groove and the substrate along the z direction and radiates into the free space from the substrate through the horizontal interface between the bottom substrate surface and the air. When the substrate underneath the central transmission line isn't grooved completely with W_1 = 0.021165 cm shown in Fig. 4.2.2, some E_y radiates on the top side of the central transmission line as well as on the edges between the coplanar ground planes and gaps shown in Fig. 4.2.13. When the substrate underneath the central transmission line is grooved completely, there isn't any radiation just above the metal central transmission line illustrated in Fig. 4.2.14. Other field components in Fig. 4.2.13-14 concentrate mainly around the fringes of the conductors.

Furthermore, the results obtained from the micromachined coplanar waveguide transmission lines with and without a bottom ground plane are compared. First of all, the comparison between Fig. 4.2.3-4 and Fig. 4.2.10-11 indicates that when $W_1 < 0.021165$ cm, the latter has lower effective permittivity and dielectric loss than the former from 0 to 60 GHz. Moreover, the conductor loss of the former in Fig. 4.2.5 is higher than that of the latter in Fig. 4.2.12 from 0 to 60 GHz. When $W_1 => 0.021165$ cm, the latter has higher effective permittivity and dielectric loss than the former one at all the frequencies of interest. However, the reason needs to be investigated further.

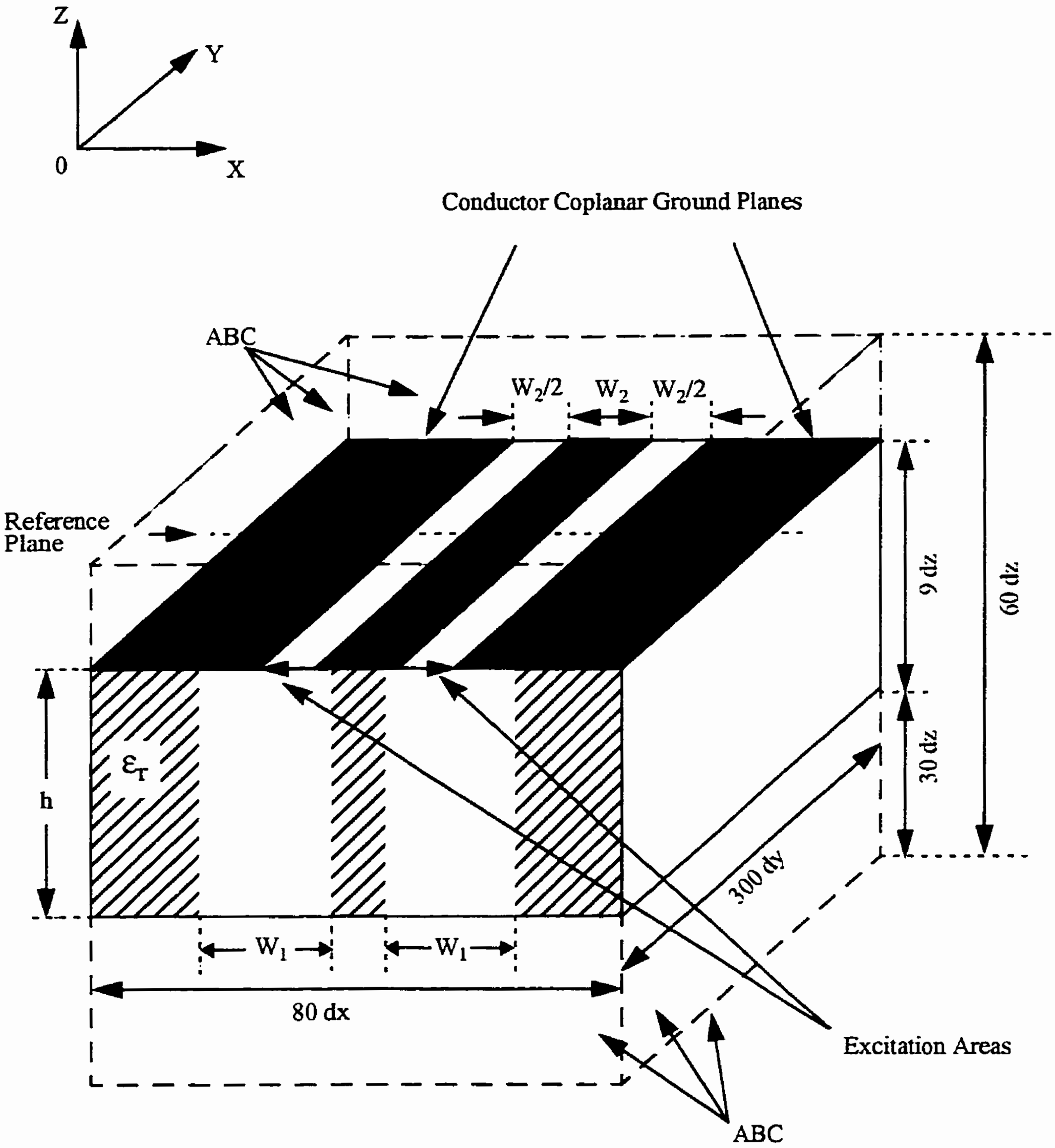

h = 0.0381 cm W_2 = 0.0254 cm ε_r = 2.2

Fig. 4.2.9 Geometry Structure of Micromachined Coplanar Waveguide Transmission Line without a Bottom Ground Plane

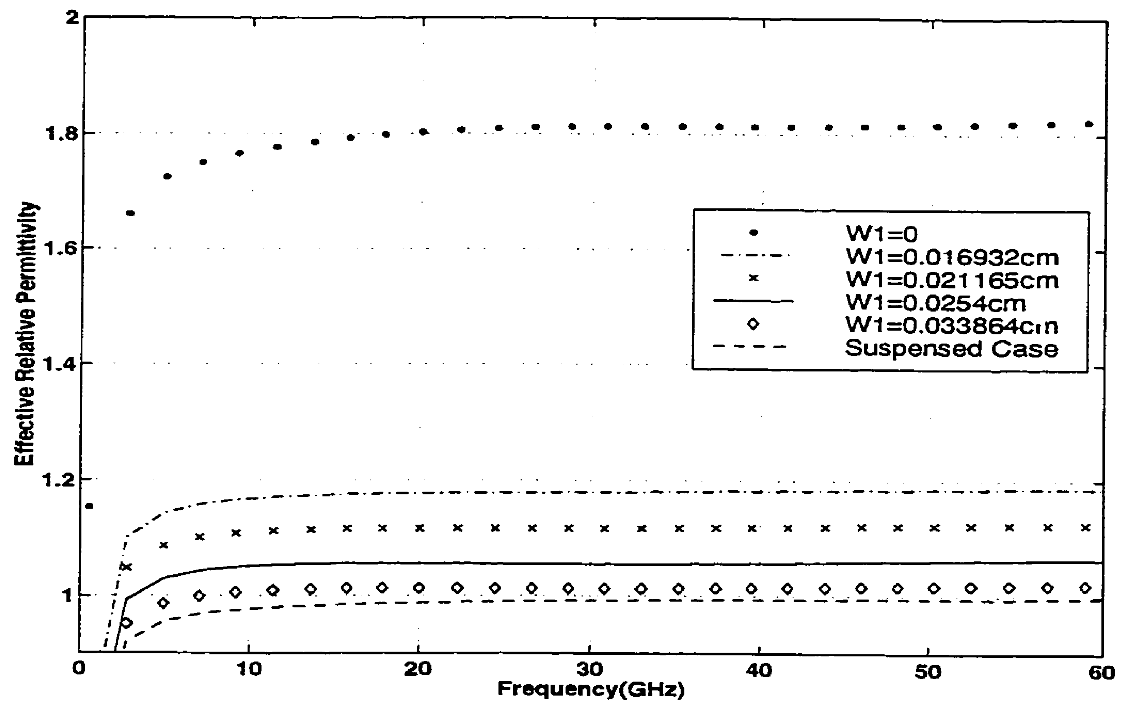

Fig. 4.2.10 Effective Relative Permittivity for Fig. 4.2.9 between Y = 130 dy & 150 dy

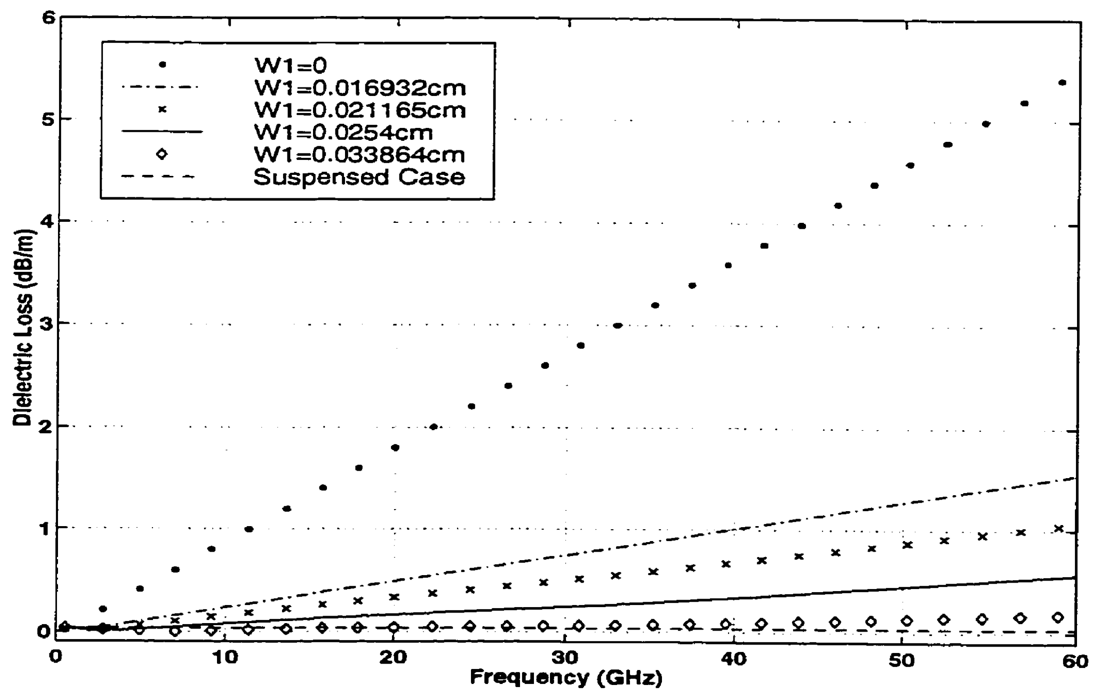

Fig. 4.2.11 Dielectric Loss for Fig. 4.2.9 between Y = 130 dy & 150 dy

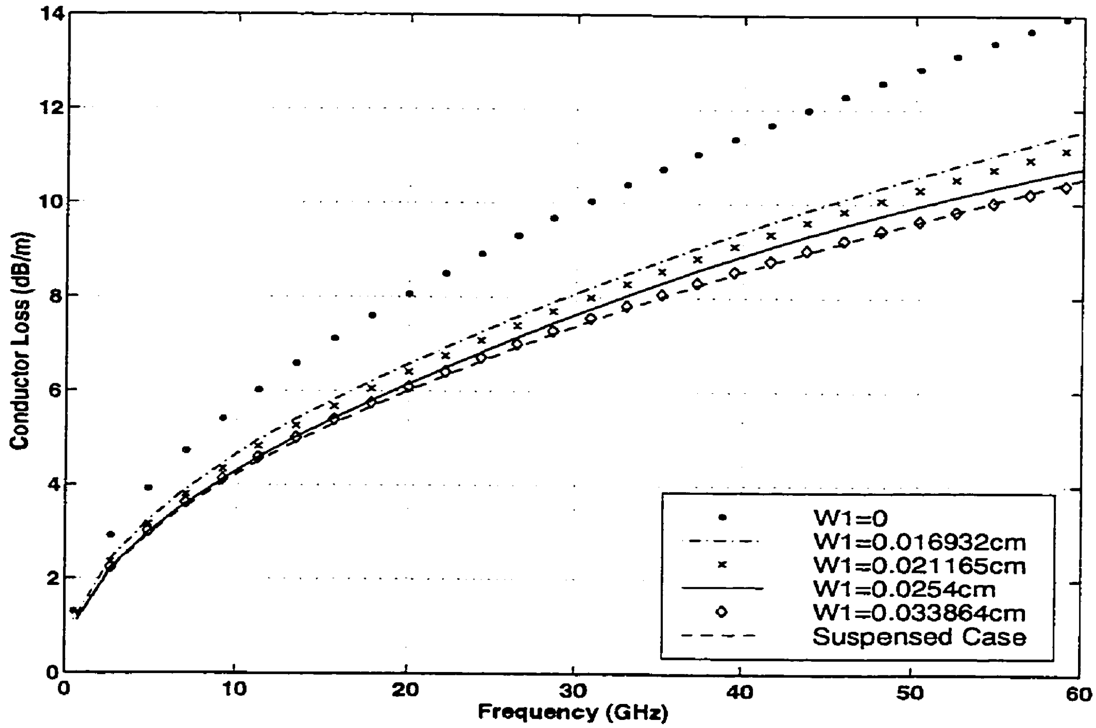

Fig. 4.2.12 Conductor Loss for Fig. 4.2.9 between Y = 130 dy & 150 dy

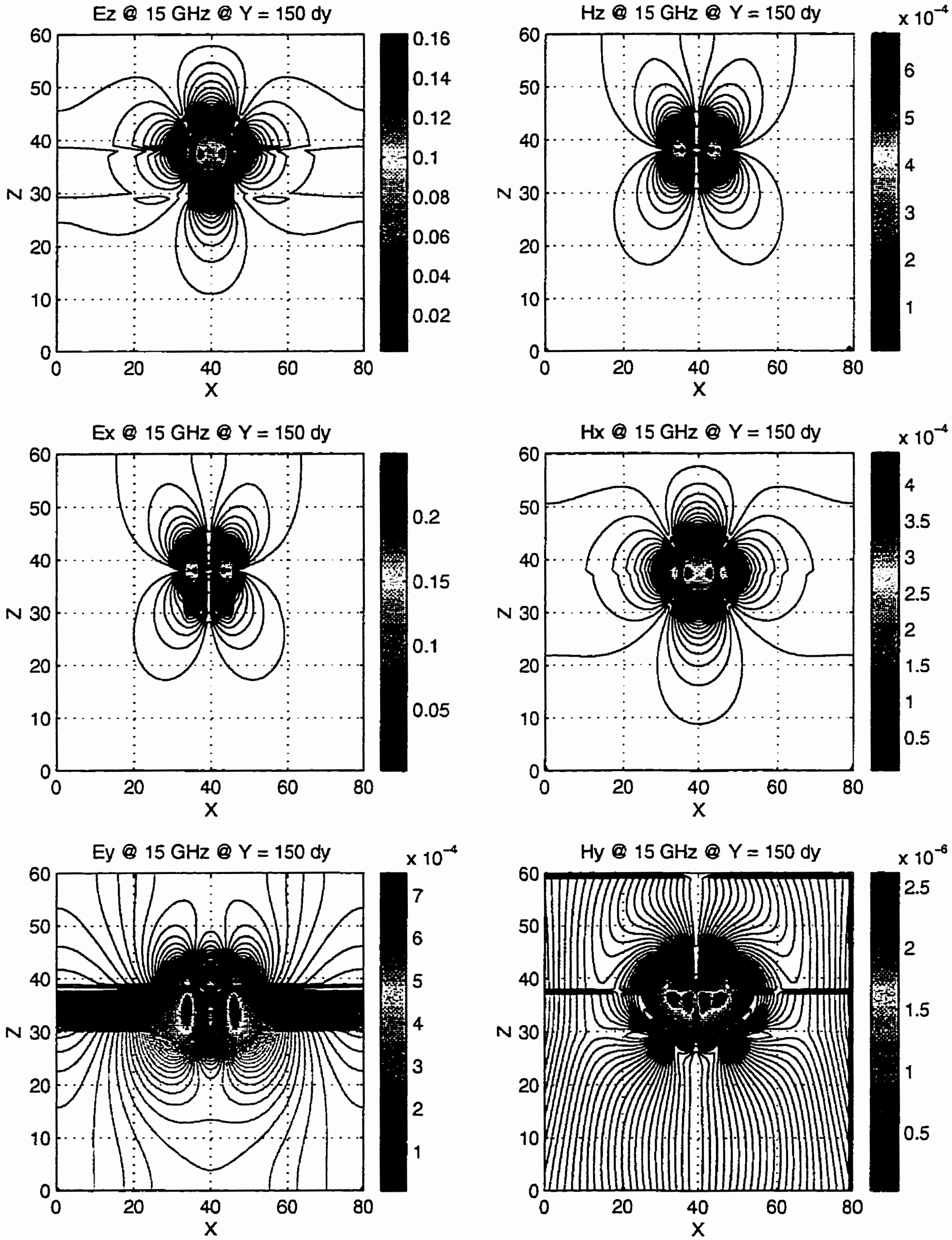

Fig.4.2.13 Electric & Magnetic Fields Distributions at 15 GHz at Y=150 dy in X-Z Plane in Fig. 4.2.9 with W_1 = 0.021165 cm, Units: E: V/m, H: A/m

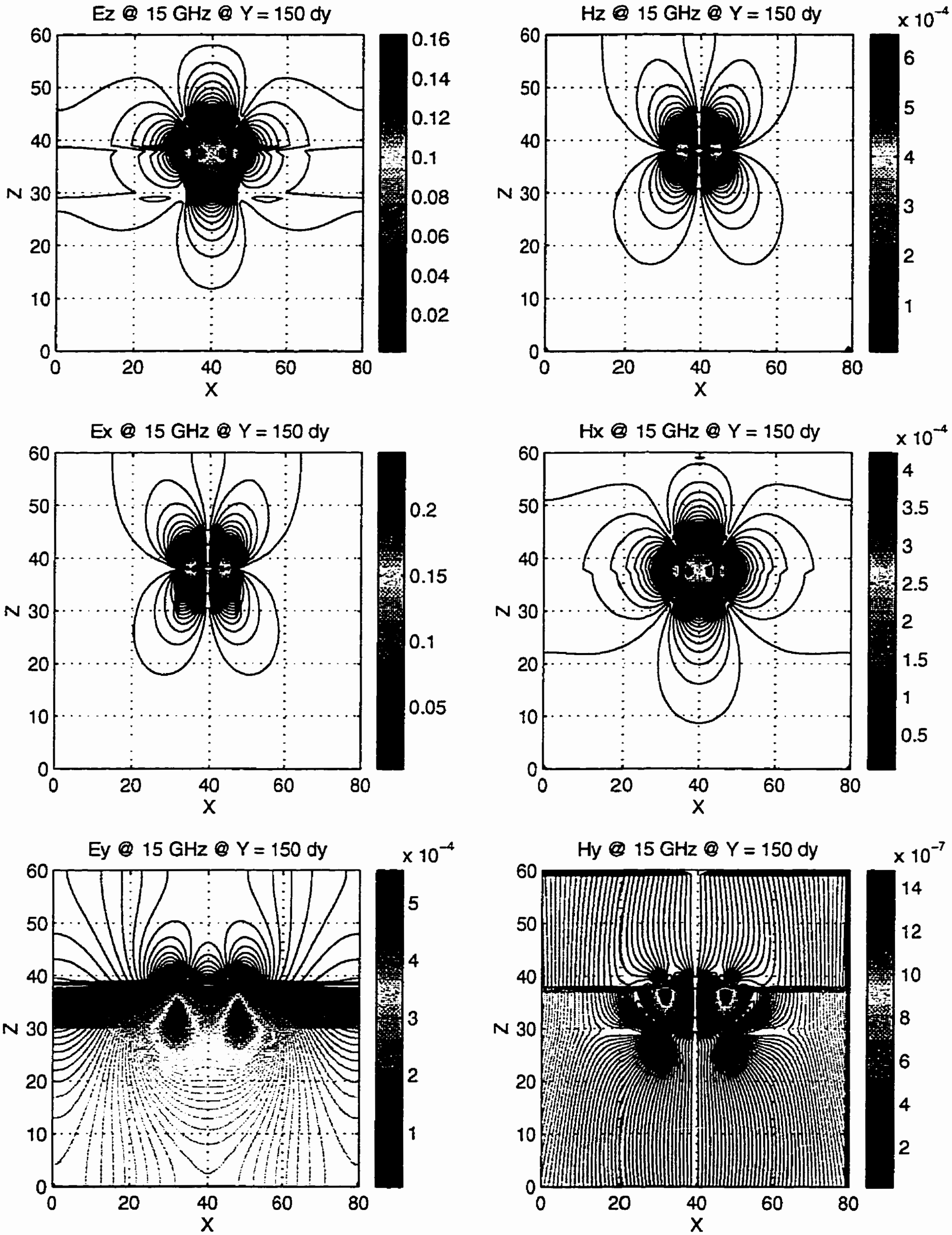

Fig. 4.2.14 Electric & Magnetic Fields Distributions at 15 GHz at Y=150 dy in X-Z Plane in Fig. 4.2.9 with W_1 = 0.033864 cm, Units: E: V/m H: A/m

CHAPTER 5

Conclusions and Future Work

This thesis is devoted to the analysis of low loss microwave & millimeter-wave planar transmission lines. The study in this thesis shows that micromachined & inverted micromachined microstrip transmission lines, trenched & micromachined CPW transmission lines have performance superior to their corresponding conventional counterparts. The significant contribution of this thesis is that, for the first time, it analyses microwave & millimeter-wave low loss planar transmission lines comprehensively, and provides the systematic analysis, on the basis of which the future experiment can be done more efficiently.

Finite-Difference Time-Domain (FDTD) method is used in this thesis because it is an efficient and relatively new method in electromagnetics compared to other conventional methods. It can get calculation result over a wide frequency range of interest at one calculation cycle. Another important advantage of FDTD over other methods is its geometrical and material generalities so that it can be used to analyse the isotropic inhomogeneous structures very well.

As the first case, FDTD was used to solve the conventional substrate microstrip patch antenna fed by non-symmetrical microstrip line. The calculated S_{11} and field distributions agree well with the published and measured results.

Then in the second case: micromachined microstrip transmission lines were analysed by FDTD. They include three types: the micromachined microstrip transmission lines with thick upper substrate, with very thin upper substrate (membrane) and inverted micromachined microstrip transmission lines. By the use of perturbation theory, the effective relative permittivity, dielectric loss, conductor loss and characteristic impedance are obtained. The results for the conventional substrates agree well with those from commercial antenna simulation software. It is found that although an inverted microstrip transmission line with conventional substrate (groove width $W_1 = 0$) has higher dielectric loss than a corresponding conventional microstrip transmission line ($W_1 = 0$), the inverted micromachined microstrip transmission lines (groove width $W_1 \neq 0$) have lower dielectric loss than those of the corresponding micromachined microstrip transmission lines (groove width $W_1 \neq 0$). However, the conductor loss of the inverted micromachined microstrip lines are generally 2 dB higher than that of the micromachined counterparts from 0 to 60 GHz. It is also discovered that the thickness of the upper substrate has a great influence on the dielectric loss of micromachined microstrip transmission lines. The thinner upper substrate it has, the less dielectric loss it will have, although the conductor loss does not change too much. Furthermore, a conclusion can be obtained that with the increase of the groove volume underneath the central transmission line, the dielectric loss decreases greatly while the conductor loss changes little. However, the conductor loss is higher than the dielectric loss at all frequencies. Thus, the conductor loss is the main source of resistive loss in this kind of structures. In addition, the spatial electric and magnetic fields distributions in frequency domain were obtained from time domain via FFT. It is found that the propagation wave energy is concentrated within the groove filled with the air and thus the dielectric loss of the whole structure under consideration is reduced. The study also shows that micromachined microstrip transmission lines can provide the most compact geometry and can be integrated with EM-coupled slots and simple fabrication.

The third type, trenched and micromachined coplanar waveguide transmission lines were studied extensively using FDTD for the first time. The trenched or micromachined coplanar waveguide transmission lines with various geometrical parameters were investigated with or without a bottom ground plane. The effective relative permittivity, dielectric loss, conductor loss, characteristic impedance and spatial field components distributions in frequency domain were obtained and shown. It was found that grooves underneath the central transmission line and gaps can reduce the dielectric loss greatly. With the increase of groove volume, the effective relative permittivity and the dielectric loss will decrease further. However, the conductor loss changes little. If the groove volume increases to reach some value, the dielectric loss approaches to zero and the conductor loss will be as low as that of the suspended case. This provides the opportunity for microwave engineers to design low loss planar transmission lines, or planar microwave components and circuits at very high frequency which can get loss as low as the ideal suspended case. The field component distributions show that in the trenched and micromachined cases, the most propagation energy concentrates at the vertical interface between the substrate and the groove filled with the air. As a result, there is lower dielectric loss in the whole structure and less radiation into the air outside of the whole structure under the consideration. Other field components focus mainly around the edges of the conductor planes. It shows that micromachined or trenched coplanar waveguide transmission lines can provide better field confinement and performance than the conventional counterparts.

Furthermore, this work is the first step to study theoretically low loss microwave & millimeter-wave planar transmission lines using FDTD. FDTD in lossy media [45] will be used as the next step. And the effect of ABC to the results need to be studied. Or, a more efficient ABC, such as Perfect Matched Layer (PML) [20] will be used. Other future work might include the fabrication and measurement of the low loss microwave or millimeter-wave planar transmission lines or circuits.

APPENDIX A

Interface Condition Between Two Dielectric Material

Suppose there is an interface plane lying in the y-z plane between two different layers with relative permittivities ε_1 and ε_2 respectively. To calculate the E_y and E_z on the interface, we start from one of the Maxwell's equations:

$$\frac{\partial E_y}{\partial t} = \frac{1}{\varepsilon_i}\left(\frac{\partial H_x}{\partial z} - \frac{\partial H_z}{\partial x} - \sigma_i E_y\right) \tag{A.1}$$

where i = 1, 2 denote the different permittivities and conductivity. Rewrite (A.1) as:

$$\frac{\partial E_y}{\partial t} = \frac{1}{\varepsilon_1}\left(\frac{\partial H_x}{\partial z} - \left.\frac{\partial H_z}{\partial x}\right|_1 - \sigma_1 E_y\right) \tag{A.2}$$

$$\frac{\partial E_y}{\partial t} = \frac{1}{\varepsilon_2}\left(\frac{\partial H_x}{\partial z} - \left.\frac{\partial H_z}{\partial x}\right|_2 - \sigma_2 E_y\right) \tag{A.3}$$

Since E_y, H_x and $\partial H_x / \partial z$ are continuous across the interface, it is obvious that $\partial H_z / \partial x$ is discontinuous across the interface; hence, by subtracting (A.3) from (A.2), we get:

$$\left(\frac{\sigma_2}{\varepsilon_2}-\frac{\sigma_1}{\varepsilon_1}\right)E_y = \left(\frac{1}{\varepsilon_2}-\frac{1}{\varepsilon_1}\right)\frac{\partial H_x}{\partial z} - \frac{1}{\varepsilon_2}\frac{\partial H_z}{\partial x}\bigg|_2 + \frac{1}{\varepsilon_1}\frac{\partial H_z}{\partial x}\bigg|_1 \tag{A.4}$$

Approximate $\partial H_z / \partial x\,|_1$ and $\partial H_z / \partial x\,|_2$ by:

$$\frac{\partial H_z}{\partial x}\bigg|_1 = \frac{H_z(m) - H_z(m-0.5)}{(\Delta x)/2} \tag{A.5}$$

$$\frac{\partial H_z}{\partial x}\bigg|_2 = \frac{H_z(m+0.5) - H_z(m)}{(\Delta x)/2} \tag{A.6}$$

where m is assumed to be the position of the interface, and m+0.5 and m-0.5 denote the position of a half step above and below the interfaces respectively in the x direction.

Substituting (A.5) and (A.6) into (A.4), we have:

$$H_z(m) = \frac{\varepsilon_1}{\varepsilon_1+\varepsilon_2}H_z(m+0.5) + \frac{\varepsilon_2}{\varepsilon_1+\varepsilon_2}H_z(m-0.5)$$

$$+\frac{\Delta x}{2}\frac{\varepsilon_2-\varepsilon_1}{\varepsilon_1+\varepsilon_2}\frac{\partial H_x}{\partial z} - \frac{\varepsilon_2\sigma_1-\varepsilon_1\sigma_2}{\varepsilon_1+\varepsilon_2}E_y \tag{A.7}$$

Substituting (A. 7) back into (A.5) and (A.6), then substituting the resulting expressions in (A.2) and (A.3) and adding them together, it is finally obtained:

$$\frac{\sigma_1+\sigma_2}{2}E_y + \frac{\varepsilon_1+\varepsilon_2}{2}\frac{\partial E_y}{\partial t} = \frac{\partial H_x}{\partial z} - \frac{\Delta H_z}{\Delta x} \tag{A.8}$$

Following the similar procedure, it can also be shown that:

$$\frac{\sigma_1 + \sigma_2}{2} E_z + \frac{\varepsilon_1 + \varepsilon_2}{2} \frac{\partial E_z}{\partial t} = \frac{\Delta H_y}{\Delta x} - \frac{\partial H_x}{\partial y} \tag{A.9}$$

Equations (A.8) and (A.9) can be interpreted physically as using the average of the parameters of the two different dielectric layers in the standard FDTD algorithm.

Appendix B

Computational Domain Effect on the Results

This appendix studies the effect of two different computational parameters on the results, the computational domain size and separation distance L in the equation (3.2.1) in Section 3.2.

Firstly, the computational domain is enlarged by putting the top ABC further away from the micromachined planar microstrip transmission lines and moving the two-side ABCs further towards the outside. So the grids of computational domain are: 160 dx * 300 dy * 60 dz which is 4 times as large as the corresponding amount of the grids in Section 3.2. As a result, the computer memory and computing time is 4 times of those needed in Section 3.2. Other parameters are the same as those in Fig. 3.2.1. The results of effective relative permittivity, dielectric loss, conductor loss and characteristic impedance are shown in Fig. B.1-6.

After comparing the Fig. 3.2.2-7 and Fig. B.1-6, it is found the calculation results of the characteristic impedance using large computational domain is better than those using small computational domain. However, the effective relative permittivity, dielectric loss and conductor loss have little improvement. These results also show that the distance of reference plane from the ABC walls and the middle point of transmission line can effect results. Therefore the reference plane should be selected to be far away from the ABC walls and the middle point of the transmission line. Although this appendix is from the

Section 3.2, this method can be applied to the other sections of this thesis .

To examine the effect of L in the results, L is changed in equation (3.2.1) is changed from 20 dy to 10 dy and 40 dy, respectively, while keeping all other parameters unchanged. The corresponding effective relative permittivities are plotted in the Fig. B.7 and Fig. B.8 respectively. They are the same as those in Fig. 3.2.2. It indicates that L has no influence on the result.

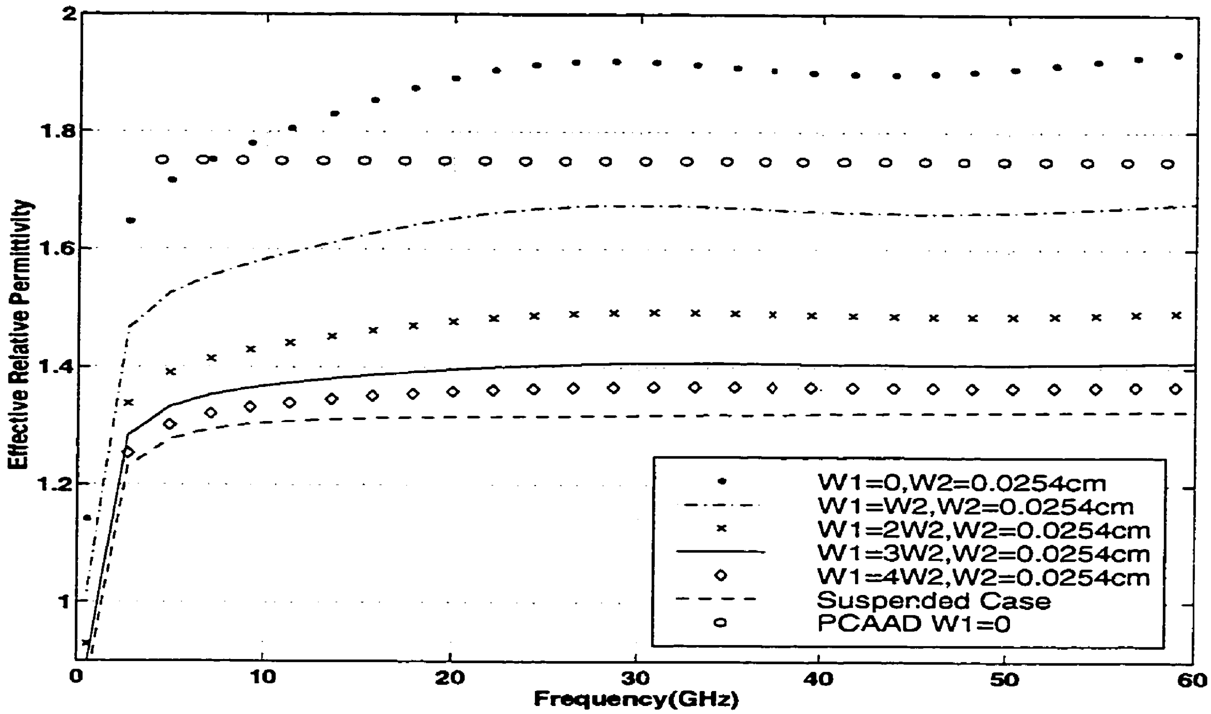

Fig. B.1 Effective Relative Permittivity for Fig. 3.2.1 between Y = 130 & 150 dy with grids 160 dx * 300 dy * 60 dz

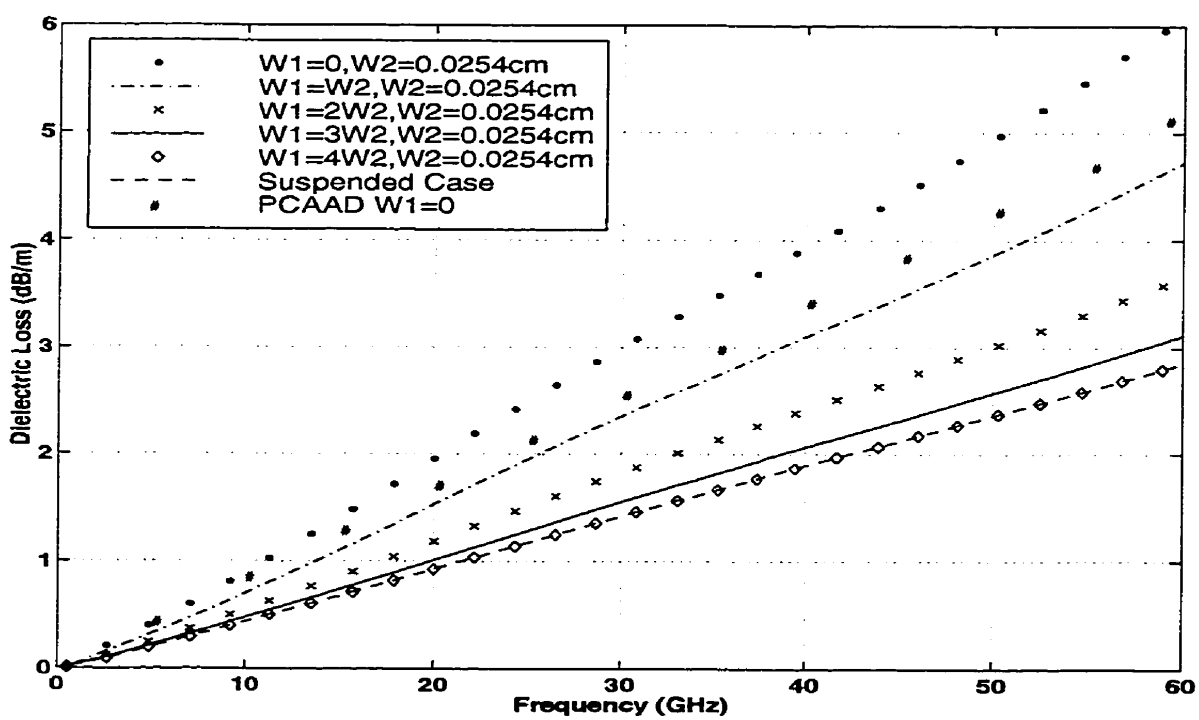

Fig. B. 2 Dielectric Loss for Fig. 3.2.1 between Y = 130 & 150 dy with grids 160 dx * 300 dy * 60 dz

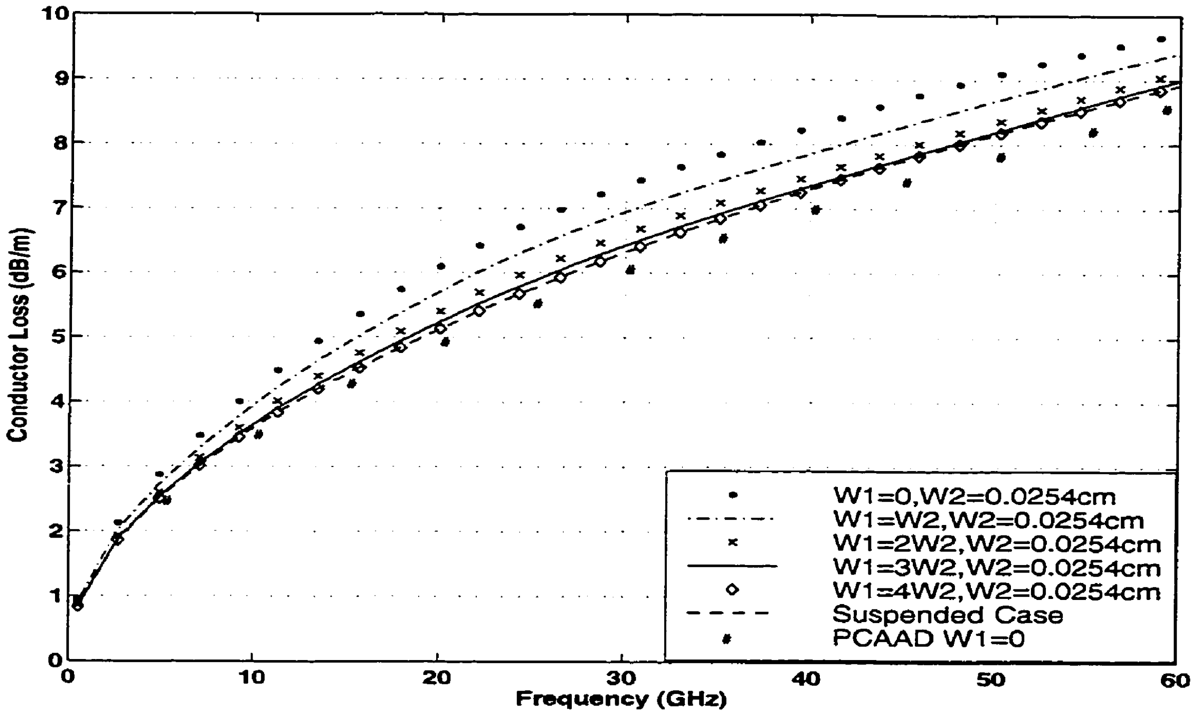

Fig. B. 3 Conductor Loss for Fig. 3.2.1 between Y = 130 & 150 dy with grids 160 dx * 300 dy * 60 dz

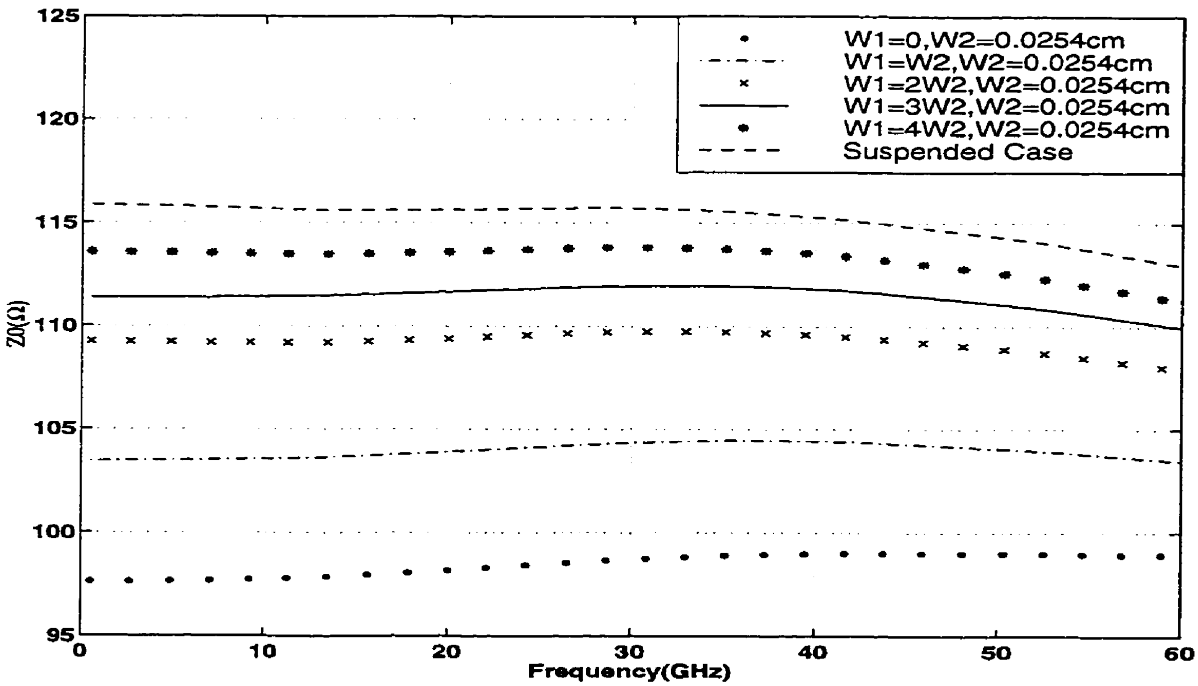

Fig. B. 4 Characteristic Impedance for Fig. 3.2.1 at Y = 30 dy grids 160 dx * 300 dy * 60 dz

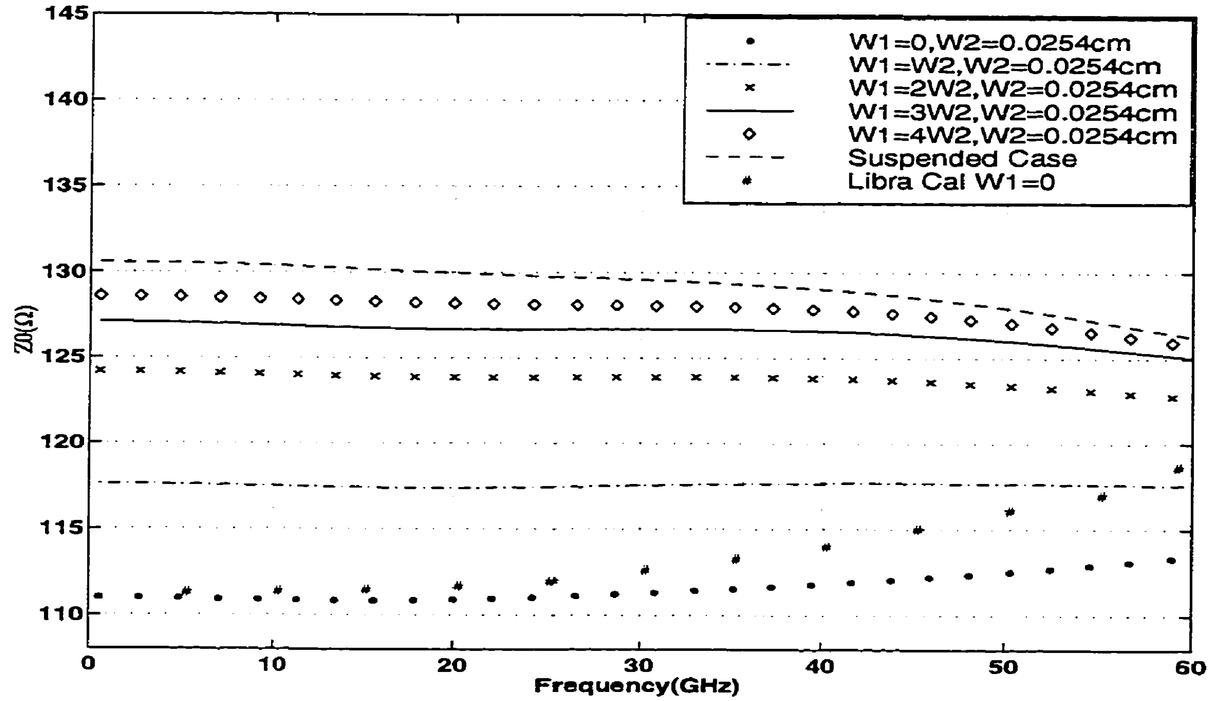

Fig. B. 5 Characteristic Impedance for Fig. 3.2.1 at Y = 50 dy
grids 160 dx * 300 dy * 60 dz

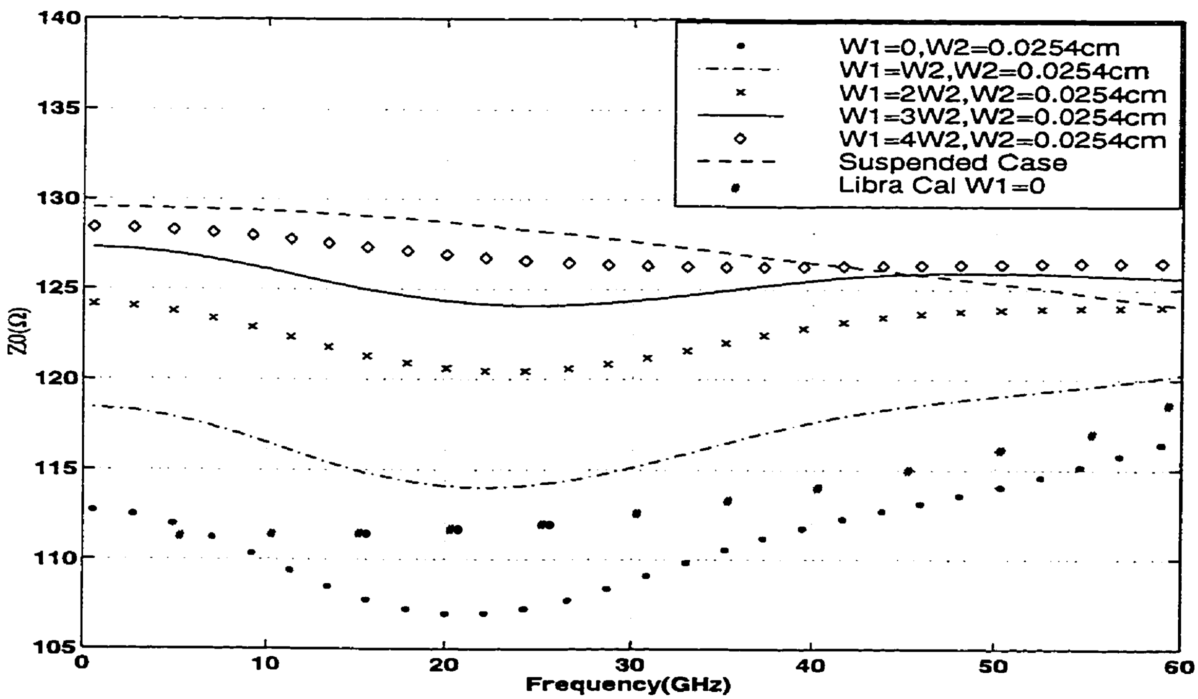

Fig. B. 6 Characteristic Impedance for Fig. 3.2.1 at Y = 150 dy
grids 160 dx * 300 dy * 60 dz

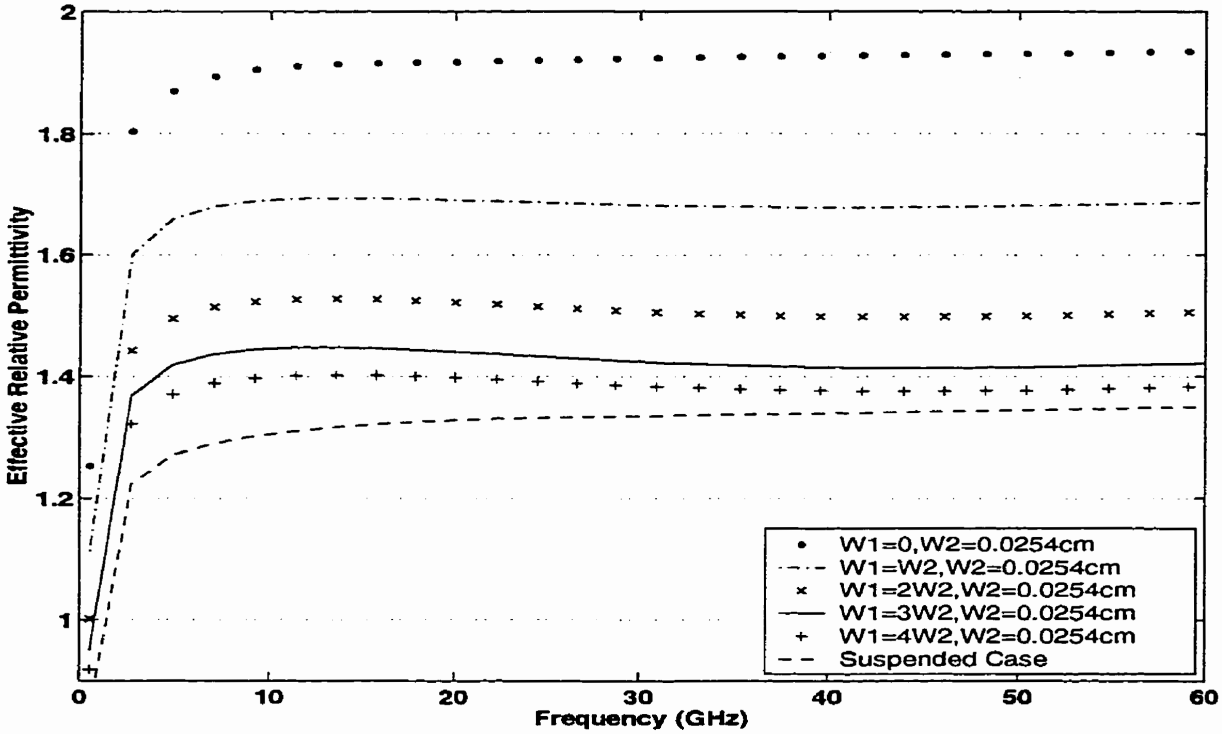

Fig. B.7 Effective Relative Permittivity for Fig. 3.2.1 for L = 10 dy

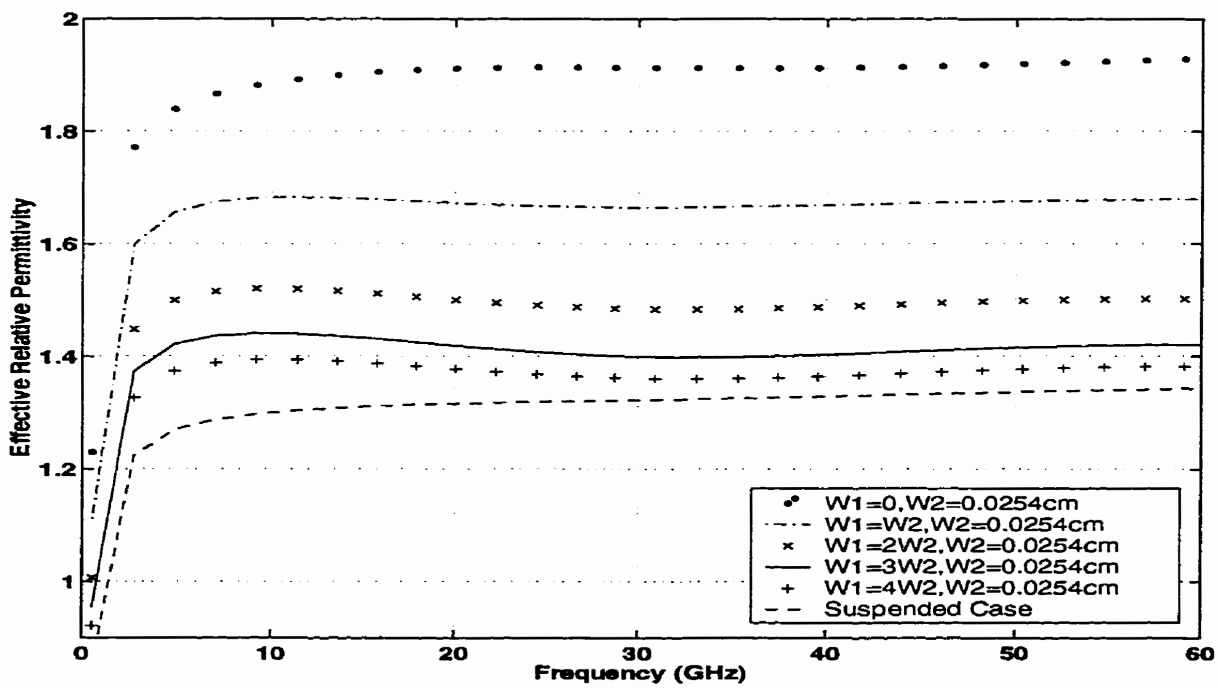

Fig. B.8 Effective Relative Permittivity for Fig. 3.2.1 for L = 40 dy

Appendix C

Effect of Time Steps on the Results

This appendix provides the study of effect of time steps on the effective relative permittivity, especially at low frequency end. Time steps 8000 and 20000 are used for the calculation for the case in Fig. 3.2.1. The corresponding effective relative permittivities at low frequency end are enlarged and plotted in Fig. C.1 and Fig. C. 2. They show that with larger time steps the accuracy of effective relative permittivity at low frequency end improves.

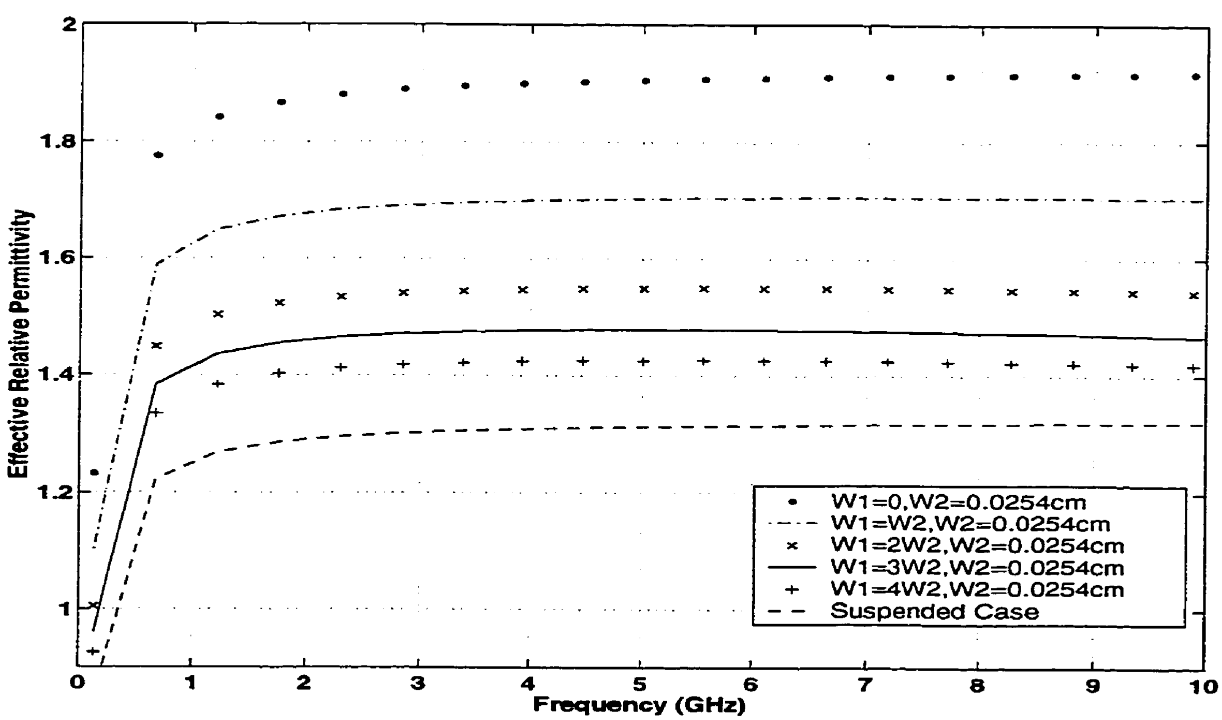

Fig. C.1 Effective Relative Permittivity for Fig. 3.2.1 between Y = 130 dy & 150 dy with Time Steps 8000

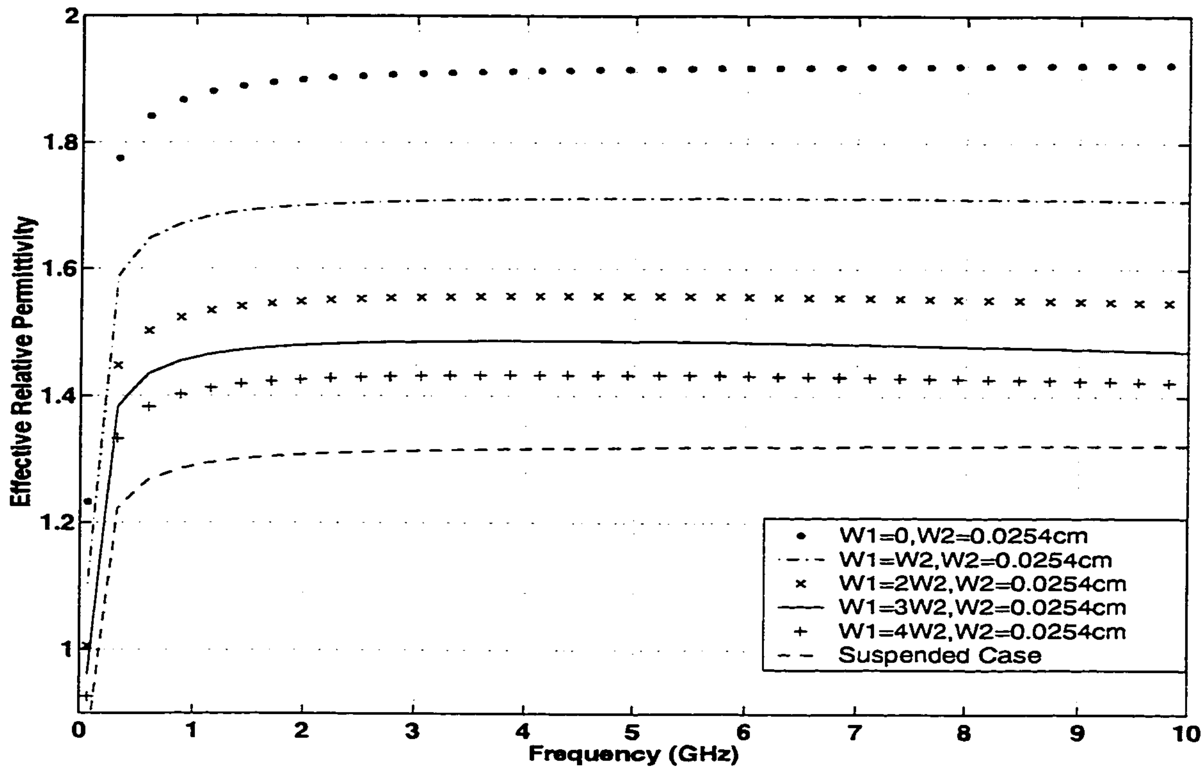

Fig. C.2 Effective Relative Permittivity for Fig. 3.2.1 between Y = 130 dy & 150 dy with Time Steps 20000

Appendix D

Discrete Fourier Transform

The Discrete Fourier Transform (DFT) used in this thesis is:[51]

$$X(k) = \frac{1}{N}\sum_{n=0}^{N-1} x[n]\, e^{-jk\left(\frac{2\pi}{N}\right)n} \qquad k = 0, 1, 2, \ldots\ldots N-1 \qquad \text{(D.1)}$$

where N is the total number of discrete time-domain points, x[n] is the values in time domain and X(k) is the values in frequency domain.

In this thesis the Fast Fourier Transfrom (FFT), which is a fast DFT, is used from Matlab. The frequency resolution in FFT is df = 1/(N*dt), where dt is the time step increment in FDTD.

REFERENCES

[1] N. I. Dib, W. P. Harokopus, L. P. B. Katehi, C. C. Ling, and G. M. Rebeiz, "Study of a Novel Planar Transmission Line", *1991 IEEE MTT-S International Microwave Symposium Digest*, Boston, MA, pp. 623-626, June 1991

[2] T. M. Weller, G. M. Rebeiz and L. P. B. Katehi, "Experimental Results on Microshield Transmission Line Circuits", *1993 IEEE MTT-S International Microwave Symposium Digest*, pp. 827-830, 1993

[3] L. P. B. Katehi, G. M. Rebeiz, T. M. Weller, R. F. Drayton, H. Cheng and J. F. Whitaker, "Micromachined Circuits for Millimeter- and Submillimeter-Wave Applications", *IEEE Antenna and Propagation Magazine*, vol. 35, No. 5, pp. 9-17, Oct. 1993

[4] T. M. Weller, L. P. B. Katehi and G. M. Rebeiz, "High Performance Microshield Line Components", *IEEE Transactions on Microwave Theory & Techniques*, vol. 43, No. 3, pp. 534-543, Mar. 1995

[5] S. V. Robertson, L. P. B. Katehi and G. M. Rebeiz, "Micromachined W-Band Filters", *IEEE Transactions on Microwave Theory & Techniques*, vol. 44, No. 4, pp. 598-606, April, 1996

[6] V. Milanovic, M. Gaitan, E. D. Bowen, M. E. Zaghloul, "Micromachined Microwave Transmission Lines in CMOS Technology", *IEEE Transactions on Microwave Theory & Techniques*, vol. 45, No. 5, pp. 630-635, May 1997

[7] K. J. Herrick, J. G. Yook, L. P. B. Katehi, "Microtechnology in the Development of Three-Dimensional Circuits", *IEEE Transactions on Microwave Theory & Tech-*

niques, vol. 46, No. 11, pp. 1832-1844, Nov. 1998

[8] S. V. Robertson, A. R. Brown, L. P. B. Katehi, G. M. Rebeiz, "A 10-60-GHz Micromachined Directional Coupler", *IEEE Transactions on Microwave Theory & Techniques*, vol. 46, No. 11, pp. 1845-1849, Nov. 1998

[9] K. S. Yee, "Numerical solution of Initial Boundary Value Problems Involving Maxwell's Equations in Isotropic Media", *IEEE Transactions on Antennas & Propagation*, vol. AP-14, No. 3, May, 1966

[10] X. Zhang, J. Fang, K. K. Mei and Y. Liu, "Calculation of the Dispersive Characteristics of Microstrips by the Time-Domain Finite-Difference Method", *IEEE Transactions on Microwave Theory & Techniques*, vol. 36, No. 2, pp. 263-267, Feb. 1988

[11] X. Zhang and K. K. Mei, "Time-Domain Finite Difference Approach to the Calculation of the Frequency-Dependent Characteristics of Microstrip Discontinuities", *IEEE Transactions on Microwave Theory & Techniques*, vol. 36, No. 12, pp. 1775-1787, Dec. 1988

[12] A. Reineix and B. Jecko, "Analysis of Microstrip Patch Antennas Using Finite Difference Time Domain Method", *IEEE Transactions on Antennas & Propagation*, vol. 37, No. 11, pp. 1361-1369, Nov. 1989

[13] D. M. Sheen, S. M. Ali, M. D. Abouzahra and J. A. Kong, "Application of the Three-Dimensional Finite-Difference Time-Domain Method to the Analysis of Planar Microstrip Circuits", *IEEE Transactions on Microwave Theory & Techniques*, vol. 38, No. 7, pp. 849-857, July 1990

[14] A. Taflove, *"Advances in Computational Electrodynamics: the Finite-Difference Time-Domain Method"*, Artech House, 1998

[15] W. A. Chamma, "Study on the Application of the Finite Difference-Time Domain Method for Solution of Electromagnetic Problems", Ph. D. Thesis, Dept. of Electrical & Computer Engineering, University of Manitoba, Winnipeg, Manitoba, Canada, Jan. 1993

[16] A. Taflove and M. E. Brodwin, "Numerical Solution of Steady-State Electromagnetic Scattering Problems Using the Time-Dependent Maxwell's Equations", *IEEE Transactions on Microwave Theory & Techniques*, vol. 23, pp. 623-630, 1975

[17] A. Taflove and K. Umashankar, "Review of FDTD Numerical Modelling of Electromagnetic Wave Scattering and Radar Cross-Section", *Proc. IEEE,* vol. 77, pp. 682-699, May 1989

[18] A. Taflove, *"Computational Electrodynamics-the Finite-Difference Time-Domain Method"*, Artech House, 1995

[19] G. Mur, "Absorbing Boundary Conditions for the Finite-Difference Approximation of the Time-Domain Electromagnetic-field Equations", *IEEE Transactions on Electromagnetic Compatibility,* vol. EMC-23, No. 4, pp. 377-382, 1981

[20] J. P. Berenger, "A Perfectly Matched Layer for the Absorption of Electromagnetics Waves", *Journal of Computational Physics*, vol. 114, No. 1, pp. 185-200, 1994

[21] K. K. Mei and J. Fang, "Superabsorption- A Method to Improve Absorbing Boundary Conditions", *IEEE Transactions on Antennas & Propagation,* vol. AP-40, No. 2, pp. 1001-1010, 1992

[22] B. Engquist and A. Majda, "Absorbing Boundary Conditions for the Numerical Simulation of Waves", *Math. of Computation,* vol. 31, pp. 629-651, July 1977

[23] J. G. Blaschak & G. Kriegsmann, "A Comparative Study of Absorbing Boundary

Conditions", *Journal of Computational Physics,* vol. 77, pp. 109-139, 1988

[24] W. Chamma, N. Gupta, L. Shafai, "Dispersion Characteristics of Suspended Microstrip Line on Segmented Dielectric Substrate", Symposium on Antenna Technology and Applied Electromagnetics, *ANTEM'98*, pp. 159-162, Aug. 1998

[25] N. Gupta, N. Jacob, W. Chamma, L. Shafai, S. Raut, A. Asi, "Simulation & Experimental Evaluation o the Low Loss Grooved Line", Symposium on Antenna Technology and Applied Electromagnetics, *ANTEM'98*, pp. 451-454, Aug. 1998

[26] A. Taflove, "Review of the Formulation and Application of the Finite-Difference Time-Domain Method for Numerical Modeling of Electromagnetic Wave Interaction with Arbitrary Structures", *Wave motion*, Vol. 10, pp. 547-582, 1988

[27] N. Dib, Linda P. B. Katehi, "Impedance Calculation for the Microshield Line", *IEEE Microwave and Guided Wave Letters*, vol. 2, No. 10, pp. 406-408, Oct. 1992

[28] M. Vaughan, K. Hur, R. Compton, "Improvement of Microstrip Patch Antenna Radiation Patterns", *IEEE Transactions on Antennas & Propagation*, Vol. 42, No. 6, pp. 882- 885, June 1994

[29] Chen-Yu Chi, G. M. Rebeiz, "Planar Microwave and Millimeter-Wave Lumped Elements and Coupled-Line Filters Using Micro-Machining Techniques", *IEEE Transactions on Microwave Theory & Techniques*, vol. 43, No. 4, pp. 730-739, April 1995

[30] R. F. Drayton, L. P. B. Katehi, "Development of Self-Packaged High Frequency Circuits Using Micromachining Techniques", *IEEE Transactions on Microwave Theory & Techniques*, vol. 43, No. 9, pp. 2073-2080, Sep. 1995

[31] M. Stotz, G. Gottwald, H. Haspeklo and J. Wenger, "Planar Millimeter-Wave Anten-

nas using $SinN_x$ -Membranes on GaAs", *IEEE Transactions on Microwave Theory & Techniques*, vol. 44, No. 9, pp. 1593-1595, Sept. 1996

[32] Chen-Yu Chi, G. M. Rebeiz, "Conductor-Loss Limited Stripline Resonator and Filters", *IEEE Transactions on Microwave Theory & Techniques*, vol. 44, No. 4, pp. 626-630, April 1996

[33] G. P. Gauthier, N. Dib, Linda P. Katehi, G. M. Rebeiz, "77 GHz Dual-Polarized Microstrip Antennas on Thin Dielectric Membrane", *IIEEE Antennas and Propagations International Symposium Digest,* pp. 1874-1877, 1997

[34] J. B. Muldavin, T. J. Ellis and G. M. Rebeiz, "Tapered Slot Antennas on the Thick Dielectric Substrates Using Micromachining Techniques", *IEEE Antennas and Propagations International Symposium Digest,* pp. 1110-1113, 1997

[35] G. P. Gauthier, A. Courtay and G. M. Rebeiz, "Microstrip Antennas on Synthesized Low Dielectric Constant Substrates", *IEEE Transactions on Antennas and Propagations,* vol. 45, No. 8, pp. 1310-1314, Aug. 1997

[36] I. Papapolymerou, R. F. Drayton, Linda, P. B. Katehi, "Micromachined Patch Antennas", *IEEE Transactions on Antennas and Propagations*, vol. 46, No. 2, pp. 275-283, Feb. 1998

[37] V. M. Lubecke, K. Mizuno and G. M. Rebeiz, "Micromachining for Terahertz Applications", *IEEE Transactions on Microwave Theory & Techniques*, vol. 46, No. 11, pp. 1821-1831, Nov. 1998

[38] K. Herrick, T. Schwarz and L. P. B. Katehi, "Si-Micromachined Coplanar Waveguides for Use in High-Frequency Circuits", *IEEE Transactions on Microwave Theory & Techniques*, vol. 46, No. 6, pp. 762-768, June 1998

[39] T. L. Willke, S. Gearhart, "LIGA Micromachined Planar Transmission Lines and Filters", *IEEE Transactions on Microwave Theory & Techniques*, vol. 45, No. 10, pp. 1681-1688, Oct. 1997

[40] S. Yang, Z. Hu, N. Buchanan, V. Fusco, J. Stewart, Y. We, B. Armstrong, G. Armstrong, H. Gamble, "Characteristics of Trenched Coplanar Waveguide for High-Resistivity Si MMIC Applications", *IEEE Transactions on Microwave Theory & Techniques*, vol. 46, No. 5, pp. 623-631, May 1998

[41] P. Salzenstein, O. Dupuis, M. Helal, E. Lheurette, O. Vanbesien, P. Mounaix and D. Lippens, "Coplanar Waveguides on Dielectric Membrane Micromachined on a GaAs Substrate", *Electronics Letters*, Vol. 32, No. 9, pp. 821-822, 25th April 1996

[42] E. Lan, S. M. El-Ghazaly, V. Nair, K. Eisenbeiser, B. Ooms, "Wide Band CAD Model for Coplanar Waveguide using FDTD Technique", *IEEE MTT-S International Microwave Symposium Digest*, pp. 1583-1586, June 1997

[43] David M. Pozar, Microwave Engineering, Addison-Wesley Inc., 1993

[44] Y. Lu and L. Shafai, "Analysis on Novel Low Loss Planar Transmission Lines", Dept. of ECE, University of Manitoba, Winnipeg, Manitoba, Canada, 1999

[45] R. Luebbers, "Lossy Dielectric in FDTD", *IEEE Transactions on Antennas & Propagation*, vol. 41, No. 11, pp. 1586-1588, Nov. 1993

[46] Y. Lu and L. Shafai, "Study of Micromachined Microstrip Lines using FDTD", *IEEE AP-S Antennas & Propagations Society International Symposium*, Orlando, FL, USA, July 1999

[47] Y. Lu & L. Shafai, "Full Wave Analysis of Low Loss Planar Transmission Lines", *XXVIth General Assembly of the International Union of Radio Science (URSI),*

Toronto, Canada, Aug. 1999

[48] Y. Lu and L. Shafai, "Characteristics of Inhomogeneous Multilayer Microstrip Transmission Lines", *Progress in Electromagnetics Research Symposium (PIERS) 1999*, Taiwan, China, Mar. 1999

[49] D. Mirshekar-Syahkal, J. B. Davies, "Accurate Solution of Microstrip & Coplanar Structures for Dispersion and for Dielectric and Conductor loss", *IEEE Transactions on Microwave Theory & Techniques*, Vol. MTT-27, No. 7, pp. 695-699, July 1979

[50] N. Gupta, L. Shafai, "Low Loss Microstrip Lines", Dept. of ECE, University of Manitoba, Winnipeg, Manitoba, Canada, 1997

[51] A. V. Oppenheim, Signals and Systems, Prentice-Hall, pp. 320-321, 1983